ELECTRONIC, MAGNETIC AND OPTICAL PROPERTIES OF DISORDERED GRAPHENE QUANTUM DOTS

A Thesis Submitted to
the Graduate School of Engineering and Sciences of
İzmir Institute of Technology
in Partial Fulfillment of the Requirements for the Degree of

DOCTOR OF PHILOSOPHY

in Physics

by
Abdulmenaf ALTINTAŞ

July 2018
İZMİR

We approve the thesis of **Abdulmenaf ALTINTAŞ**

Examining Committee Members:

_____
Assoc. Prof. Dr. Alev Devrim GÜÇLÜ
Department of Physics, İzmir Institute of Technology

_____
Assoc. Prof. Dr. Cem ÇELEBİ
Department of Physics, İzmir Institute of Technology

_____
Assoc. Prof. Dr. Hâldun SEVİNÇLİ
Department of Materials Science and Engineering, İzmir Institute of Technology

_____
Prof. Dr. Bekir Sıtkı KANDEMİR
Department of Physics, Ankara University

_____
Assoc. Prof. Dr. Engin DURGUN
National Nanotechnology Research Center , İhsan Doğramacı Bilkent University

2 July 2018

_____
Assoc. Prof. Dr. Alev Devrim GÜÇLÜ
Supervisor, Department of Physics
İzmir Institute of Technology

_____
Prof. Dr. R. Tuğrul SENGER
Head of the Department of
Physics

_____
Prof. Dr. Aysun SOFUOĞLU
Dean of the Graduate School of
Engineering and Sciences

ACKNOWLEDGMENTS

ABSTRACT

ELECTRONIC, MAGNETIC AND OPTICAL PROPERTIES OF DISORDERED GRAPHENE QUANTUM DOTS

In this thesis, we theoretically investigate electronic, magnetic and optical properties of disordered graphene quantum dots. The numerical calculations are performed using a combination of tight-binding, mean-field Hubbard and configuration interaction methods. We focus on the effects of long-range disorder and electron-electron interactions on the optical properties and the effects of atomic defect related short-range disorders and electron-electron interactions on Anderson type localization and the magnetic properties of hexagonal armchair graphene quantum dots. For the case of long-range disorder, we show that, when the electron-hole puddles are present, tight-binding method gives a poor description of the low-energy absorption spectra compared to meanfield and configuration interaction calculation results. As the size of the graphene quantum dot is increased, the universal optical conductivity limit can be observed in the absorption spectrum. When disorder is present, calculated absorption spectrum approaches the experimental results for isolated monolayer of graphene sheet. On the other hand, for the case of short-range related disorder, we observe that randomly distributed defects with concentrations between 1-5% of the total number of atoms leads to electronic localization alongside magnetic puddle-like structures. We show that localization length is not affected by magnetization if there is an even distribution of defects between the two sublattices of the honeycomb lattice. However, for an uneven distributions, localization is found to be significantly enhanced.

ÖZET

DÜZENSİZ GRAFEN KUANTUM NOKTALARININ ELEKTRONİK, MANYETİK VE OPTİK ÖZELLİKLERİ

Bu tezde, düzensiz grafen kuantum noktalarının elektronik, manyetik ve optik özelliklerini inceliyoruz. Nümerik hesaplar tight-binding, mean-field Hubbard ve konfigürasyon etkileşimi metodlarını kullanarak yapılmıştır. Grafen kuantum noktaları için, uzun-mesafe etkili düzensizliklerin ve elektron-elektron etkileşimlerinin optik özellikleri üzerindeki etkisi ve atomik-boyutlu kısa mesafe etkili düzensizliklerin ve elektron-elektron etkileşimlerinin Anderson tipi lokalizasyon ve manyetik özellikler üzerindeki etkisine odaklanıyoruz. Uzun-mesafe etkili düzensizlikler durumu için, elektron-hole puddlelları olduğu zaman tight-binding metodu, düşük enerjili emilim spektrumu için, mean-field Hubbard ve konfigürasyon etkileşimi metodları ile kıyaslandığında yeterli bir açıklama veremediğini gösteriyoruz. Grafen kuantum noktasının büyüklüğü arttıkça, emilim spektrumunda evrensel optik iletim limiti gözlemlenebiliyor. Düzensizlikler olduğu zaman, izole grafen tabakası için hesaplanan emilim spektrumu deneysel sonuçlarla uyumlu hale geliyor. Diğer taraftan, kısa mesafe etkili düzensizlik durumları için, toplam atom sayısının %1-5 oranı kadar olarak rasgele dağıtılan düzensizlik yoğunluğunun, elektronik lokalizasyonun oluşması yanında manyetik puddle benzeri yapıların oluşmasına neden oluyor. Eğer düzensizlikler alt örgüler arasında eşit bir şekilde dağıtılırsa lokalizasyon uzunluğunun manyetikleşmeden etkilenmediğini gösteriyoruz. Tam tersine, eğer düzensizlikler alt örgüler arasında eşit olmayan bir şekilde dağıtılırsa, lokalizasyonun daha fazla olduğu gözlemleniyor.

... to my wife Elena

and

Family ...

TABLE OF CONTENTS

LIST OF FIGURES

LIST OF TABLES

CHAPTER 1

INTRODUCTION

Throughout the history of humankind, search for functional materials have always been hot topic and will likely continue to be in the future. Although the roles of functional materials have been changing from stone age to smart materials age, the demands for those materials have always been high due to needs of time eras as shown in Figure 1.1 (Gandhi and Thompson, 1992).
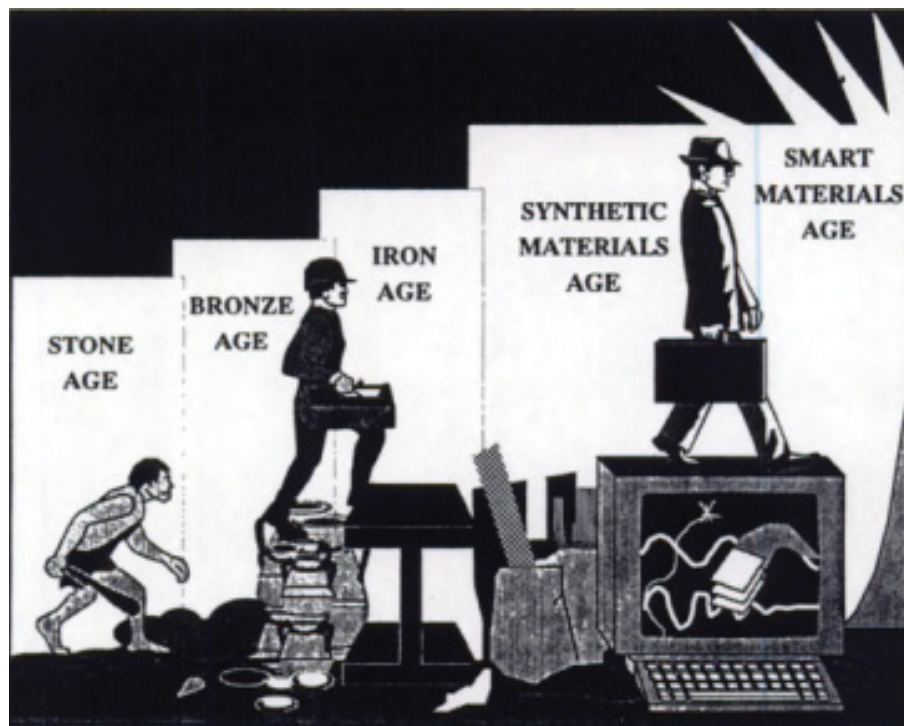
Figure 1.1. Representative cartoon of evolution of human demands for functional materials in different time eras. (Source: Gandhi and Thompson, 1992).

After being studied theoretically by Wallace in 1947 and produced with mechanical exfoliation by Novoselov *et al.* in 2004 , graphene was identified as a multi-functional material due to its promising electrical conductivity, structural strength, thermal conductivity and striking optical characteristics (Wallace, 1947; Novoselov *et al.*, 2004, 2005;

Zhang *et al.*, 2005; Rycerz *et al.*, 2007; Lee *et al.*, 2008; Dikin *et al.*, 2007; Xin *et al.*, 2015; Mak *et al.*, 2008; Zhang *et al.*, 2009). Graphene, two dimensional hexagonal array of carbon atoms (see upper left of Figure 1.2) offers variety of applications in electronics, optics, medicine, construction, transportation etc. (Novoselov *et al.*, 2012; Geim and Novoselov, 2007; Zurutuza and Marinelli, 2014).
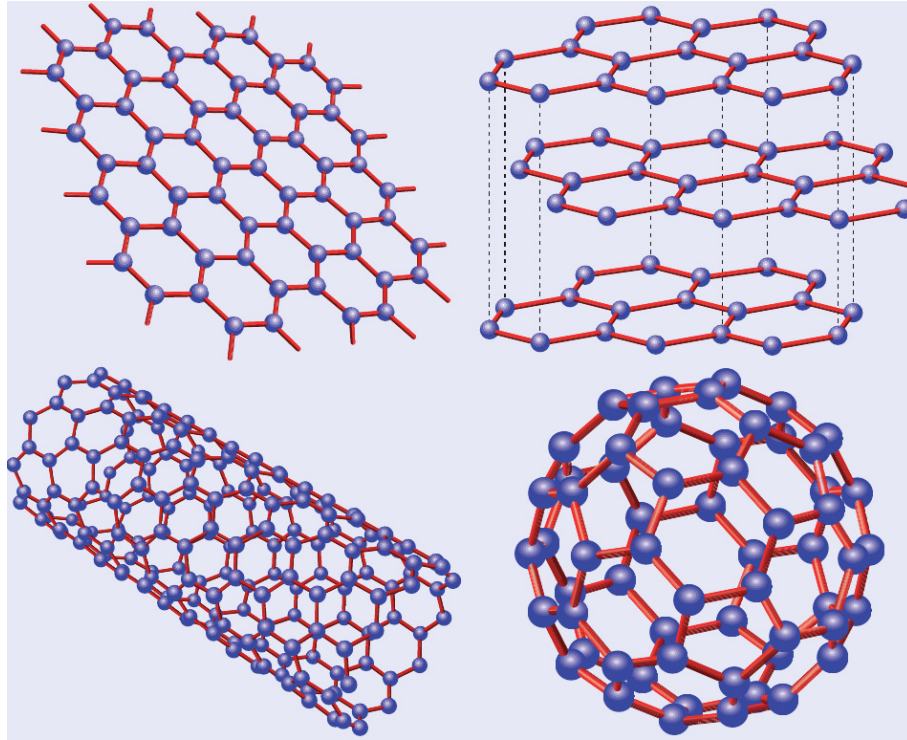
Figure 1.2. Graphene (upper left), stack of graphene layers (graphite, upper right), rolled-up cylinder of graphene (carbon nano-tube, lower left) and rolled-up ball of graphene (buckminsterfullerene, lower right). Corresponding carbon atoms and bonds are represented by blue balls and red sticks, respectively. (Source: Neto *et al.*, 2006).

Graphene sheet can be shaped to have desired structure for a specific purpose as can be seen in Figure 1.2 (Neto *et al.*, 2006). On the other hand, electronic, magnetic and optical properties of graphene can be manipulated at the nanoscale in the desired way by controlling lateral size, shape, type of edge, doping level and the number of layers in graphene nanostructures (Li *et al.*, 2008; Cai *et al.*, 2010; Treier *et al.*, 2011; Mueller *et al.*, 2010; Morita *et al.*, 2011; Wassmann *et al.*, 2008).

Among those various graphene nanostructures, graphene quantum dots (GQDs)
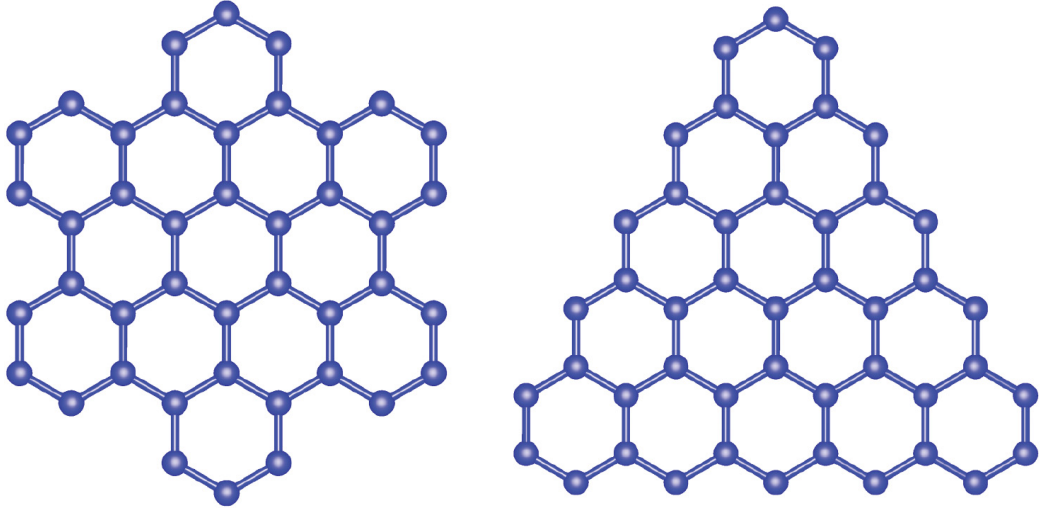
Figure 1.3. Graphene quantum dots. Carbon atoms and bonds are represented by blue balls and sticks, respectively. Hexagonal armchair edged GQD (left) and triangular zigzag edged GQD (right).

(see Figure 1.3) offer a possibility to simultaneously control the electronic, magnetic and optical functionalities in a single material and are classified according to their edge character since the edges play an important role in determining physical properties of GQDs. (Altıntaş *et al.*, 2017; Güçlü *et al.*, 2011; Voznyy *et al.*, 2011; Güçlü *et al.*, 2016; Shen *et al.*, 2012; Ritter and Lyding, 2009; Peng *et al.*, 2012; Trauzettel *et al.*, 2007; Gerardot *et al.*, 2008; Zarenia *et al.*, 2011; Potasz *et al.*, 2012; Güçlü *et al.*, 2009, 2010; Basak *et al.*, 2015; Sun *et al.*, 2015; Li *et al.*, 2015; Ozfidan *et al.*, 2016). In particular, GQDs with zigzag edges (see right part of Figure 1.3) are found to exhibit unusual magnetic and optical properties due to the presence of a degenerate band of states at the Fermi level. On the contrary, armchair edges (see left part of Figure 1.3) do not lead to degenerate band of states at the Fermi level, hence, can be used as small model of bulk graphene which does not have edge states (Altıntaş *et al.*, 2017; Güçlü *et al.*, 2011; Voznyy *et al.*, 2011; Güçlü *et al.*, 2016).

A detailed theoretical investigation of combined effects of long-range disorder and electron-electron interactions on the optical properties of graphene quantum dots is still lacking. Hence, we investigate theoretically electronic and optical properties of medium and large sized hexagonal armchair GQDs to understand the role of long-ranged disorder on the optical properties. Our main contribution involves inclusion of

electron-electron interactions within meanfield and many-body configuration interaction approaches. We show that the electron-electron interactions play a significant role in redistributing electron-hole puddles, thus strongly affecting the optical properties. We also investigate the large size limit of the GQDs as compared to optical properties of bulk graphene Mak *et al.* (2011); Lee *et al.* (2011); Yuan *et al.* (2011) and show that UOC can be observed in GQDs with a diameter of 18 nm.

In order to find out the role of atomic defects in both the localization of electronic states and the magnetic behavior at the nanoscale, we perform meanfield Hubbard (MFH) calculations for medium sized graphene quantum dots (GQD). More specifically, we focus on hexagonal shaped GQDs with armchair edges which are, unlike zigzag edges, free of magnetized edge effects. We show that localization of electronic states can occur due to randomly created atomic defects, together with formation of magnetic puddles.
The text of this thesis is organized as follows:

Chapter 2 briefly describes and lists methods that are used conventionally to fabricate graphene nanostructures.

Chapter 3 provides with theoretical background of models that are carried out to understand physical properties of GQDs. Band structure of bulk graphene is constructed and second quantization method and derivation of models such as tight binding, meanfield Hubbard and configuration interaction are discussed.

Chapter 4 gives detailed analysis about understanding absorption properties of GQDs by using tight-binding, mean-field Hubbard and configuration methods. We describe absorption properties of graphene nanostructures and effects of charge impurities and electron-electron interaction on the optical properties of GQDs.

Chapter 5 analyses magnetic properties of GQDs which has short-range disorders such as hydrogenation or vacancies. We explain magnetization caused by defects and try to understand antiferromagnetic and ferromagnetic behavior of GQDs.

Chapter 6 focuses on the effects of randomly created disorders on the localization of electronic waves. We show that randomly created short-range disorders leads to Anderson-type localization of electronic waves in GQDs.

Finally, Chapter 7 provides with a brief conclusion.

CHAPTER 2

GRAPHENE NANOSTRUCTURES

In this chapter, we briefly describe and list methods including mechanical exfoliation, chemical vapor deposition (CVD), epitaxial graphene formation on SiC and bottom-up fabrication that are used conventionally to fabricate graphene nanostructures.

2.1. Graphene Nanostructures Fabrication Methods

Graphene fabrication attempts dates back to almost 60 years ago when Boehm *et al.* produced graphite thin film (Boehm *et al.*, 1962).
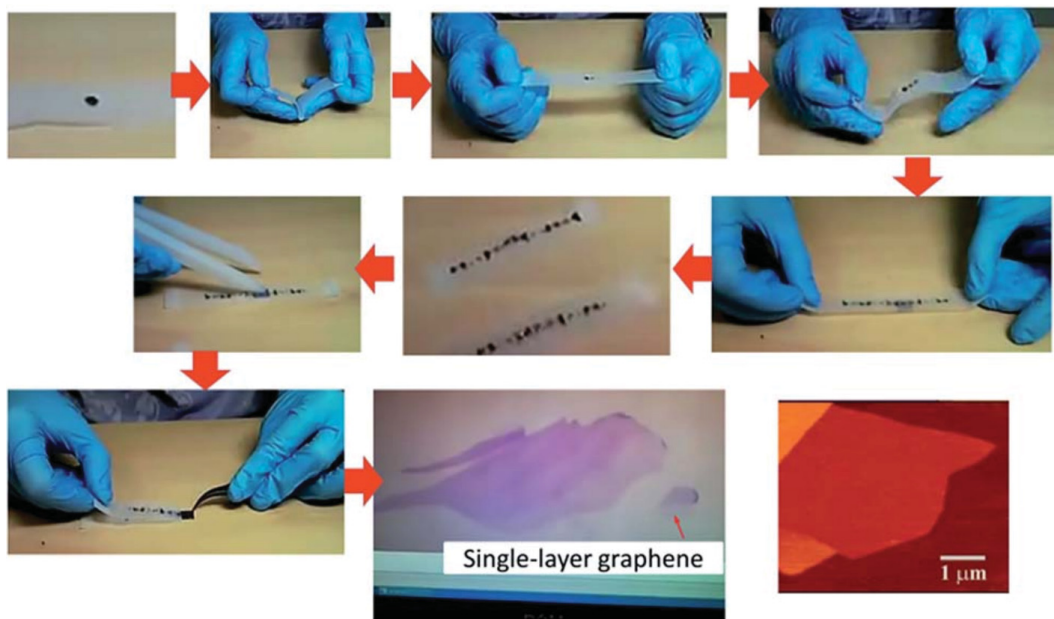
Figure 2.1. Fabrication of graphene by using mechanical exfoliation method. A graphite piece is sticked to a scotch tape and layers of graphite are isolated by repeatedly sticking the tape to the graphite to brake the van der Waals bond between layers. (Source: Yi and Shen, 2015).

One layer of graphite has been produced since then (Van Bommel *et al.*, 1975;

Boehm *et al.*, 1986; Lu *et al.*, 1999) and was first isolated with method of mechanical exfoliation by scientists in 2004 (Novoselov *et al.*, 2004).

2.1.1. Mechanical Exfoliation

Exfoliation of graphene mechanically is low cost and relatively easy method to obtain several layers or single layer of graphene (Dresselhaus and Dresselhaus, 2002; Shenderova *et al.*, 2002; Novoselov *et al.*, 2004). A graphite piece is sticked to a scotch tape and layers of graphite are isolated by repeatedly sticking the tape to the graphite to brake the van der Waals bond between layers, hence, one can obtain single layer of graphite (graphene) as shown in Figure 2.1 (Yi and Shen, 2015).

2.1.2. Chemical Vapor Deposition

Chemical vapor deposition has also been a common method to produce single or several layers of graphene (Johansson *et al.*, 1994; Reina *et al.*, 2008; Wei *et al.*, 2009; Li *et al.*, 2011).
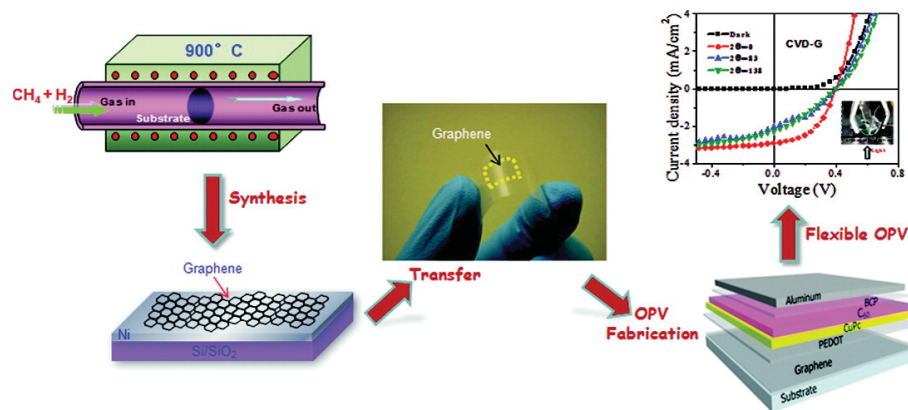
Figure 2.2. Graphene fabrication by using CVD. Carbon atoms are precipitated on Ni to produce desired layer of graphene. (Source: Gomez De Arco *et al.*, 2010).

Firstly, a transition metal such as Ni is evaporated on SiO_2/Si substrate area which is patterned by electron beam lithography (Reina *et al.*, 2008). After annealing of Ni,
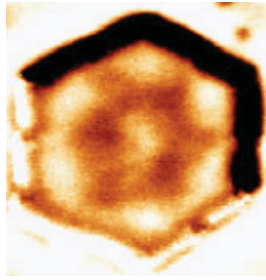
Figure 2.3. It is possible to fabricate graphene quantum dots having width size 8 nm fabricated by using CVD. (Source: Subramaniam *et al.*, 2012).

hydrocarbons are introduced in ultra high vacuum (UHV) ambient and carbon atoms are precipitated on Ni to produce desired layer of graphene. Then, graphene is transferred from substrate with the help of poly(methyl methacrylate) (PMMA) to a targeted substrate in order to be used in a specific manner(Gomez De Arco *et al.*, 2010) as shown in Figure 2.2.
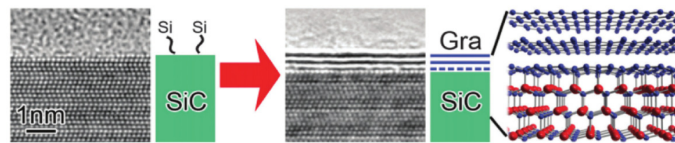
Figure 2.4. Graphene fabrication on SiC. One can produce single layer of graphene and then apply epitaxial methods to fabricate desired device to be characterized. (Source: Zaretski and Lipomi, 2015).

By using CVD, it is also possible to fabricate graphene quantum dots having width size $\leqslant$ 10 nm as shown in Figure 2.3 (Gomez De Arco *et al.*, 2010; Subramaniam *et al.*, 2012).

2.1.3. Graphene Formation on SiC

Graphene formation on SiC is a commonly applied technique to produce single layer of graphene (Kusdemir *et al.*, 2015; Zaretski and Lipomi, 2015; Hass *et al.*, 2008;

Wu *et al.*, 2009; Emtsev *et al.*, 2009; Berger *et al.*, 2004, 2006). SiC substrate is heated to a temperature which brakes bonding of Si and C atoms and leads to desorption of Si atoms from the surface by leaving surface for C atoms to rebond on surface as shown in Figure 2.4 (Zaretski and Lipomi, 2015). By using this method, one can produce single layer of graphene and then apply epitaxial methods to fabricate desired device to be characterized (Kusdemir *et al.*, 2015).

2.1.4. Bottom-up Fabrication Method of Graphene Quantum Dots

Apart from top-down fabrication, graphene nano-structures can be produced by so called bottom-up method (Liu *et al.*, 2011; Dong *et al.*, 2012; Cai *et al.*, 2010; Talirz *et al.*, 2013; Cai *et al.*, 2014).
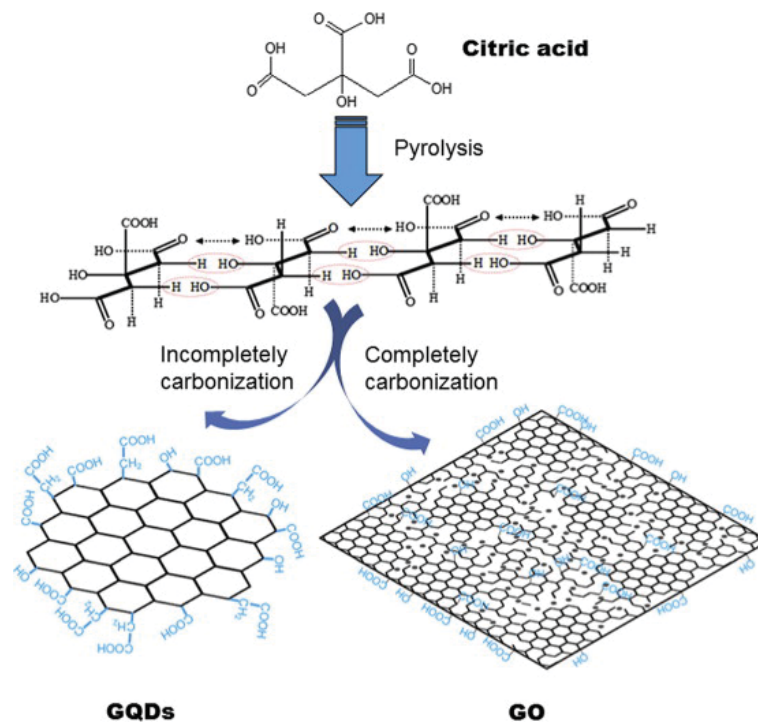
Figure 2.5. Bottom-up fabrication procedure of graphene quantum dots. Process relies on chemically directed reactions with the help of precursors and atomically precious structures can be built. (Source: Dong *et al.*, 2012).

This fabrication process relies on chemically directed reactions with the help of precursors and atomically precious structures can be built as shown in Figure 2.5 (Dong

et al., 2012). In this procedure, citric acid gets decomposed through being heated to a high temperature of 200 °C with introduction of carboxylic acid (COOH) which leads to formation of GQDs and graphene oxides (GO) when exposed to incomplete and complete carbonizations, respectively (Dong *et al.*, 2012).

CHAPTER 3

THEORETICAL MODELS

In this chapter, we start with obtaining band structure of bulk graphene by using p_z orbitals residing on honeycomb lattice structure. In order to get familiarized with notation used in theoretical models for GQDs, we briefly describe second quantization method and show derivation of models such as tight binding, mean-field Hubbard and configuration interaction.

3.1. Graphene's Electronic Band Structure

A carbon atom has 6 electrons and electronic configuration of ground state energy level as $1s^2 2s^2 2p^2$, hence, it is expected to have one type of bonding due to its electronic configuration.
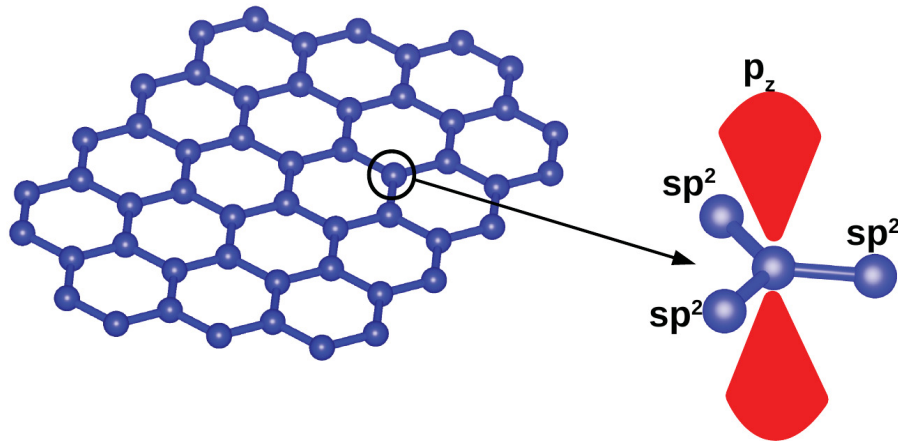
Figure 3.1. Schematic of sp^2 bonding of Carbon atoms. A small portion of graphene bulk structure (left side of figure) and corresponding sp^2 bonding (right side of figure). p_z orbitals pictured by red cones.

However, carbon atoms form different type bondings due to hybrid orbitals such as sp, sp^2 and sp^3 when they are brought together under certain conditions (Pauling, 1941;
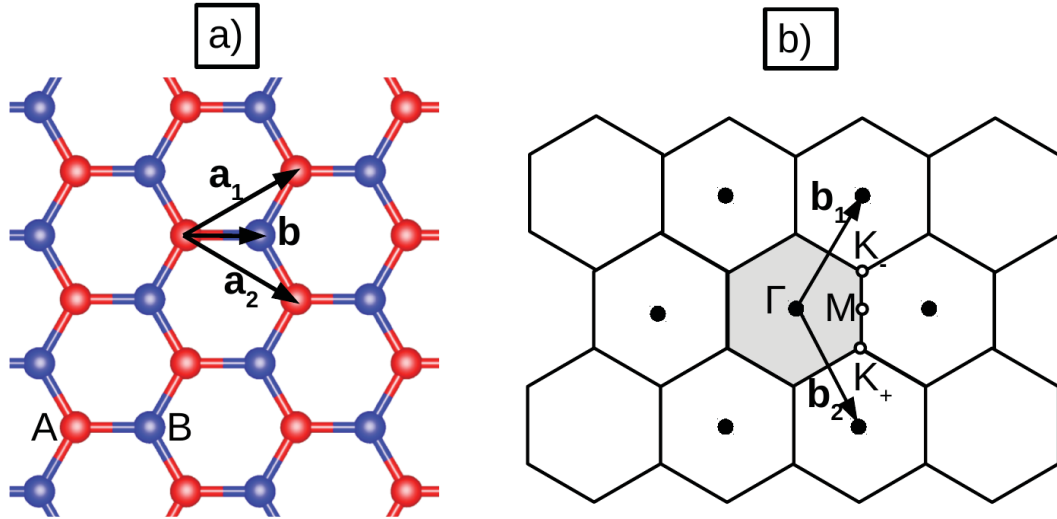
Figure 3.2. a) Real and b) reciprocal lattice space structure of graphene. a) Carbon atoms belonging to two different sublattices labeled by letter A (red ball) and B (blue ball). $\mathbf{a_1}$ and $\mathbf{a_2}$ represent unit cell vectors and $\mathbf{b}$ represents distance vector between two Carbon atoms. b) $\mathbf{b_1}$ and $\mathbf{b_2}$ represent reciprocal lattice vectors and corresponding symmetry points in Brillouin zone (shaded area) are labeled by Γ, K and M.

McFeely *et al.*, 1974; Muller *et al.*, 1993; Gilkes *et al.*, 1997, 2000; Jin *et al.*, 2009). One electron can be promoted from $2s^2$ to $2p$ orbital and leads to electronic configuration of $1s^2 2s^1 2p_x^1 2p_y^1 2p_z^1$. Graphene obtains its honey-comb crystal structure (see Figure 3.1) and mechanical stability when Carbon atoms bond in hybrid sp^2 orbital configuration which is an admixture of $2s$, $2p_x$ and $2p_y$ orbitals. On the other hand, $2p_z$ orbitals, which are perpendicular to graphene sheet, are mainly responsible for electronic, optic and magnetic properties of graphene (Wallace, 1947; Novoselov *et al.*, 2004, 2005; Zhang *et al.*, 2005; Rycerz *et al.*, 2007; Lee *et al.*, 2008; Dikin *et al.*, 2007; Xin *et al.*, 2015; Mak *et al.*, 2008; Zhang *et al.*, 2009) as can be seen in Figure 3.1.

Graphene honeycomb crystal structure can be build up by triangular Bravais lattice consists of two basis atoms labeled A and B as shown in Figure 3.2. Primitive unit cell can be constructed by vectors $\mathbf{a_1}$ and $\mathbf{a_2}$. One can form all graphene lattice points by taking integer multiple of unit vectors with basis atoms located at $(0, 0)$ and $(0, b)$ where b=1.42 Å is the distance between two carbon atoms.

We define primitive vectors for real space lattice as:

$$\mathbf{a_1} = a \left(\frac{\sqrt{3}}{2}, \frac{1}{2} \right) \tag{3.1}$$

$$\mathbf{a_2} = a \left(\frac{-\sqrt{3}}{2}, \frac{1}{2} \right) \tag{3.2}$$

where $a = \sqrt{3}b$ is the real space lattice constant and corresponding reciprocal space lattice vectors are:

$$\mathbf{b_1} = a_r \left(\frac{1}{2}, \frac{\sqrt{3}}{2} \right) \tag{3.3}$$

$$\mathbf{b_2} = a_r \left(\frac{1}{2}, \frac{-\sqrt{3}}{2} \right) \tag{3.4}$$

where reciprocal space lattice constant $a_r = 4\pi/a\sqrt{3}$ and relation between two spaces is $\mathbf{a_i} \cdot \mathbf{b_j} = 2\pi \delta_{ij}$.

Position vectors for A-type and B-type atoms are defined as:

$$\mathbf{R_A} = l\mathbf{a_1} + m\mathbf{a_2} + \mathbf{b} \tag{3.5}$$

$$\mathbf{R_B} = l\mathbf{a_1} + m\mathbf{a_2} \tag{3.6}$$

where l and m are integers.

The state of an electron $\Psi^{A,B}(\mathbf{k}, \mathbf{r})$ on sublattice A,B can be written as a linear combination of p_z orbital wave function's $\psi_z(\mathbf{r} - \mathbf{R_{A,B}})$ which are localized on the related sublattice site as:

$$\Psi^A(\mathbf{k}, \mathbf{r}) = \frac{1}{\sqrt{N_{cell}}} \sum_{R_A} \psi_z(\mathbf{r} - \mathbf{R_A}) e^{i\mathbf{k} \cdot \mathbf{R_A}} \tag{3.7}$$

$$\Psi^B(\mathbf{k}, \mathbf{r}) = \frac{1}{\sqrt{N_{cell}}} \sum_{R_B} \psi_z(\mathbf{r} - \mathbf{R_B}) e^{i\mathbf{k} \cdot \mathbf{R_B}} \tag{3.8}$$

where N_{cell} represents the number of unit cell in the structure.

Total state function of electron can be written as a linear combination of state in sublattice A and B:

$$\Psi(\mathbf{k}, \mathbf{r}) = c_{\mathbf{k}}^A \Psi^A(\mathbf{k}, \mathbf{r}) + c_{\mathbf{k}}^B \Psi^B(\mathbf{k}, \mathbf{r}) \tag{3.9}$$

and Hamiltonian of this state function:

$$H = \frac{p^2}{2m} + \sum_{R_A} U(\mathbf{r} - \mathbf{R_A}) + \sum_{R_B} U(\mathbf{r} - \mathbf{R_B}) \qquad (3.10)$$

where $U(\mathbf{r} - \mathbf{R_{A,B}})$ are atomic potentials centered at $\mathbf{R_{A,B}}$. Then, Hamiltonian $H(\mathbf{k})$ matrix in the basis of $\Psi^{A,B}(\mathbf{k}, \mathbf{r})$ can be expressed as:

$$H(\mathbf{k}) = \begin{bmatrix} <\Psi^A(\mathbf{k}, \mathbf{r}) \mid H \mid \Psi^A(\mathbf{k}, \mathbf{r})> & <\Psi^A(\mathbf{k}, \mathbf{r}) \mid H \mid \Psi^B(\mathbf{k}, \mathbf{r})> \\ <\Psi^B(\mathbf{k}, \mathbf{r}) \mid H \mid \Psi^A(\mathbf{k}, \mathbf{r})> & <\Psi^B(\mathbf{k}, \mathbf{r}) \mid H \mid \Psi^B(\mathbf{k}, \mathbf{r})> \end{bmatrix} \qquad (3.11)$$

and we assume that $\Psi^A(\mathbf{k}, \mathbf{r})$ and $\Psi^B(\mathbf{k}, \mathbf{r})$ are orthogonal. As a next step, we need to diagonalize $2x2$ Hamiltonian matrix and find eigenvalue and eigenvectors. We will make nearest neighbor approximation, hence, neglect next neighbor and further neighbor atomic orbital interactions.

We write first matrix element as:

$$<\Psi^A(\mathbf{k}, \mathbf{r}) \mid H \mid \Psi^A(\mathbf{k}, \mathbf{r})> =$$

$$\frac{1}{\sqrt{N_{cell}}} \sum_{R_A, R_{A'}, R_B} <\psi_z(\mathbf{r} - \mathbf{R_{A'}}) \mid H(\mathbf{k}) \mid \psi_z(\mathbf{r} - \mathbf{R_A})> e^{i\mathbf{k} \cdot (\mathbf{R_A} - \mathbf{R_{A'}})}$$

$$= \frac{1}{\sqrt{N_{cell}}} \sum_{R_A, R_{A'}} \{ <\psi_z(\mathbf{r} - \mathbf{R_{A'}}) \mid \frac{p^2}{2m} + U(\mathbf{r} - \mathbf{R_A}) \mid \psi_z(\mathbf{r} - \mathbf{R_A})>$$

$$+ <\psi_z(\mathbf{r} - \mathbf{R_{A'}}) \mid \frac{p^2}{2m} + \sum_{R_B} U(\mathbf{r} - \mathbf{R_B}) \mid \psi_z(\mathbf{r} - \mathbf{R_A})> \} e^{i\mathbf{k} \cdot (\mathbf{R_A} - \mathbf{R_{A'}})} \quad (3.12)$$

and additionally, equation for sub lattice A as:

$$\left(\frac{p^2}{2m} + \sum_{R_A} U(\mathbf{r} - \mathbf{R_A}) \right) \mid \psi_z(\mathbf{r} - \mathbf{R_A})> = \epsilon_A \mid \psi_z(\mathbf{r} - \mathbf{R_A})> . \qquad (3.13)$$

We take $\epsilon_A = 0$ and $<\psi_z(\mathbf{r} - \mathbf{R_{A'}}) \mid \psi_z(\mathbf{r} - \mathbf{R_A})> = 0$.
Then, we obtain $<\Psi^A(\mathbf{k}, \mathbf{r}) \mid H \mid \Psi^A(\mathbf{k}, \mathbf{r})> = 0$. Similarly, other matrix element $<\Psi^B(\mathbf{k}, \mathbf{r}) \mid H \mid \Psi^B(\mathbf{k}, \mathbf{r})> = 0$. We write off-diagonal matrix element as:

$$<\Psi^B(\mathbf{k}, \mathbf{r}) \mid H \mid \Psi^A(\mathbf{k}, \mathbf{r})> =$$

$$\frac{1}{\sqrt{N_{cell}}} \sum_{R_A, R_{B'}, R_B} <\psi_z(\mathbf{r} - \mathbf{R_B}) \mid U(\mathbf{r} - \mathbf{R_{B'}}) \mid \psi_z(\mathbf{r} - \mathbf{R_A})> e^{i\mathbf{k} \cdot (\mathbf{R_A} - \mathbf{R_B})} \quad (3.14)$$

by neglecting $R_A = R_B$ and taking $R_B = R_{B'}$, we get:

$$<\Psi^B(\mathbf{k}, \mathbf{r}) \mid H \mid \Psi^A(\mathbf{k}, \mathbf{r})> =$$

$$\frac{1}{\sqrt{N_{cell}}} \sum_{<R_A, R_B>} <\psi_z(\mathbf{r} - \mathbf{R_B}) \mid U(\mathbf{r} - \mathbf{R_{B'}}) \mid \psi_z(\mathbf{r} - \mathbf{R_A})> e^{i\mathbf{k} \cdot (\mathbf{R_A} - \mathbf{R_B})}. \quad (3.15)$$
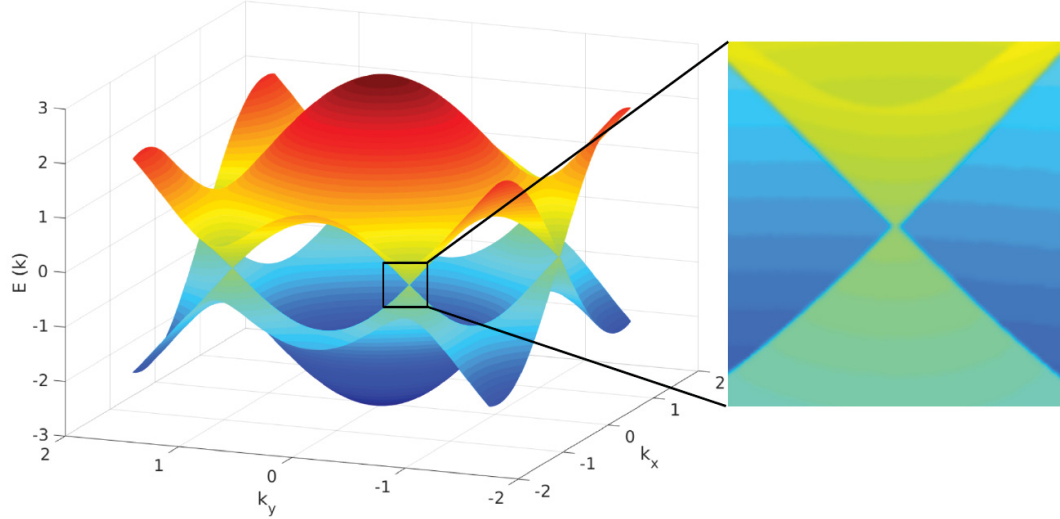
Figure 3.3. Band structure of graphene. Zoomed zero energy level shows that graphene is a gap-less semi metal.

We define nearest neighbor hopping parameter t as:

$$t = < \psi_z(\mathbf{r} - \mathbf{R_B}) \mid U(\mathbf{r} - \mathbf{R_{B'}}) \mid \psi_z(\mathbf{r} - \mathbf{R_A}) > . \tag{3.16}$$

Then, we obtain

$$< \Psi^B(\mathbf{k}, \mathbf{r}) \mid H \mid \Psi^A(\mathbf{k}, \mathbf{r}) >= t \left(e^{i\mathbf{k}\cdot\mathbf{b}} + e^{i\mathbf{k}\cdot(\mathbf{b}-\mathbf{a_1})} + e^{i\mathbf{k}\cdot(\mathbf{b}-\mathbf{a_2})} \right) \tag{3.17}$$

and

$$< \Psi^A(\mathbf{k}, \mathbf{r}) \mid H \mid \Psi^B(\mathbf{k}, \mathbf{r}) >= t \left(e^{-i\mathbf{k}\cdot\mathbf{b}} + e^{-i\mathbf{k}\cdot(\mathbf{b}-\mathbf{a_1})} + e^{-i\mathbf{k}\cdot(\mathbf{b}-\mathbf{a_2})} \right) . \tag{3.18}$$

By also defining:

$$f(\mathbf{k}) = e^{-i\mathbf{k}\cdot\mathbf{b}} + e^{-i\mathbf{k}\cdot(\mathbf{b}-\mathbf{a_1})} + e^{-i\mathbf{k}\cdot(\mathbf{b}-\mathbf{a_2})}, \tag{3.19}$$

we get eigenvalue and vector equation for $H(\mathbf{k})$ as:

$$\begin{bmatrix} 0 & tf(\mathbf{k}) \\ tf^*(\mathbf{k}) & 0 \end{bmatrix} \begin{bmatrix} c_{\mathbf{k}}^A \\ c_{\mathbf{k}}^B \end{bmatrix} = E(\mathbf{k}) \begin{bmatrix} c_{\mathbf{k}}^A \\ c_{\mathbf{k}}^B \end{bmatrix} . \tag{3.20}$$

By solving this matrix equation, we get energy eigenvalues as:

$$E_\pm(\mathbf{k}) = \mp t |f(\mathbf{k})|. \tag{3.21}$$

We can write energy values explicitly as:

$$E_{\pm}(k_x, k_y) = \mp\sqrt{1 + 4cos^2(k_ya/2) + 4cos(\sqrt{3}k_xa/2)cos(k_ya/2)}. \qquad (3.22)$$

and obtain electronic band of graphene as shown in the Figure 3.3. Band structure of graphene shows us that graphene is a gap-less semi metal at the Dirac points (zero energy level) which are located at symmetric K points (see Figure 3.2b).

3.2. Second Quantization

By using second quantization formalism, one only works with algebraic manipulation of quantum mechanical operators instead of working with complicated properties of determinants made up of orbitals (Doi, 1976; Runge *et al.*, 1991; Berazin, 2012; Szabo and Ostlund, 2012). We start with generic orbitals associated with annihilation a and creation $a^\dagger$ operators. We define a slater determinant acted upon by $a_l^\dagger$ as:

$$a_l^\dagger \mid \phi_m, \cdots, \phi_z > = \mid \phi_l\phi_m, \cdots, \phi_z > . \qquad (3.23)$$

where $a_l^\dagger$ creates an electron in the orbital ϕ_l. Order of acting of creation operators are important. For example, we can write:

$$a_k^\dagger a_l^\dagger \mid \phi_m, \cdots, \phi_z > = a_k^\dagger \mid \phi_l\phi_m, \cdots, \phi_z >$$
$$= \mid \phi_k\phi_l\phi_m, \cdots, \phi_z > \qquad (3.24)$$

and by changing the order we obtain:

$$a_l^\dagger a_k^\dagger \mid \phi_m, \cdots, \phi_z > = a_l^\dagger \mid \phi_k\phi_m, \cdots, \phi_z >$$
$$= \mid \phi_l\phi_k\phi_m, \cdots, \phi_z >$$
$$= - \mid \phi_k\phi_l\phi_m, \cdots, \phi_z > \qquad (3.25)$$

where Slater determinant alters the sign when order of its components changes. By adding equations (3.24) and (3.25), we get:

$$(a_k^\dagger a_l^\dagger + a_l^\dagger a_k^\dagger) \mid \phi_m, \cdots, \phi_z > = 0. \qquad (3.26)$$

Since we have used an arbitrary determinant $\mid \phi_m, \cdots, \phi_z >$, we have verified creation operator relations as:

$$a_k^\dagger a_l^\dagger + a_l^\dagger a_k^\dagger = \{a_k^\dagger, a_l^\dagger\} = 0 \qquad (3.27)$$

15

We can take $k = l$ and get :

$$a_l^\dagger a_l^\dagger = -a_l^\dagger a_l^\dagger$$
$$= 0 \qquad (3.28)$$

which means that two electrons can not occupy the same orbital. Hence, when we choose two electrons to occupy two arbitrary orbitals ϕ_m and ϕ_n and try to create two electrons occupying ϕ_l orbital, we obtain null state as:

$$a_l^\dagger a_l^\dagger \mid \phi_m \phi_n > = a_l^\dagger \mid \phi_l \phi_m \phi_n >$$
$$= \mid \phi_l \phi_l \phi_m \phi_n >$$
$$= 0 \qquad (3.29)$$

In general terms,

$$a_l^\dagger \mid \phi_l, \cdots, \phi_z >= 0 \qquad (3.30)$$

if $l \in \{l, \cdots, z\}$ which claims that no more than one electron can be created in the same orbital. It is a manifestation of Pauli exclusion principle in second quantized form.

On the other hand, annihilation operator a_l which is defined as adjoint of the creation operator $a_l^\dagger$ acts on state vector or Slater determinant (Slater, 1929) as:

$$a_l \mid \phi_l \phi_m, \cdots, \phi_z >= \mid \phi_m, \cdots, \phi_z > . \qquad (3.31)$$

and annihilate an electron in orbital ϕ_l. By following similar procedure of creation operator and taking adjoint of equation (3.27), we obtain anti-commutation relation for annihilation operators as:

$$a_k a_l + a_l a_k = \{a_k, a_l\}$$
$$= 0. \qquad (3.32)$$

We also define a condition such that an electron can not be removed from orbital in which it is not available, that is,

$$a_l \mid \phi_m, \cdots, \phi_z >= 0. \qquad (3.33)$$

if $l \notin \{m, \cdots, z\}$. In order to obtain anti-commutation relation of creation and annihilation operator, we write:

$$(a_l a_l^\dagger + a_l^\dagger a_l) \mid \phi_m, \cdots, \phi_z > = a_l a_l^\dagger \mid \phi_m, \cdots, \phi_z >$$
$$= a_l \mid \phi_l \phi_m, \cdots, \phi_z >$$
$$= \mid \phi_m, \cdots, \phi_z > . \qquad (3.34)$$

16

where we have assumed that determinant $\mid \phi_m, \cdots, \phi_z >$ did not include an electron in orbital ϕ_l.

On the contrary, we can define Slater determinant which includes an electron in orbital ϕ_l and write equation as:

$$
\begin{aligned}
(a_l a_l^\dagger + a_l^\dagger a_l) \mid \phi_l \phi_m, \cdots, \phi_z > &= a_l^\dagger a_l \mid \phi_m, \cdots, \phi_z > \\
&= a_l \mid \phi_l \phi_m, \cdots, \phi_z > \\
&= \mid \phi_m, \cdots, \phi_z > .
\end{aligned}
\tag{3.35}
$$

and we obtain anti-commutation relation relation of creation and annihilation operator for both case as:

$$
\begin{aligned}
a_l a_l^\dagger + a_l^\dagger a_l &= \{a_l, a_l^\dagger\} \\
&= 1.
\end{aligned}
\tag{3.36}
$$

To generalize anti-commutation relation, we write condition when $k \in \{k, m, \cdots, z\}$ and $l \notin \{k, m, \cdots, z\}$ as:

$$
\begin{aligned}
(a_k a_l^\dagger + a_l^\dagger a_k) \mid \phi_k \phi_m, \cdots, \phi_z > &= -(a_k a_l^\dagger + a_l^\dagger a_k) \mid \phi_m \phi_k, \cdots, \phi_z > \\
&= -a_k \mid \phi_l \phi_k \phi_m, \cdots, \phi_z > - a_l^\dagger \mid \phi_m, \cdots, \phi_z > \\
&= a_k \mid \phi_k \phi_l \phi_m, \cdots, \phi_z > - \mid \phi_l \phi_m, \cdots, \phi_z > \\
&= \mid \phi_l \phi_m, \cdots, \phi_z > - \mid \phi_l \phi_m, \cdots, \phi_z > \\
&= 0
\end{aligned}
\tag{3.37}
$$

where we have used $\mid \phi_k \phi_l \phi_m, \cdots, \phi_z > = - \mid \phi_l \phi_k \phi_m, \cdots, \phi_z >$ property. Hence, we obtain:

$$
\begin{aligned}
(a_k a_l^\dagger + a_l^\dagger a_k) &= \{a_k, a_l^\dagger\} \\
&= 0
\end{aligned}
\tag{3.38}
$$

when $k \neq l$. Finally, we can generalize anti-commutation relation by combining equations (3.36) and (3.38) as:

$$
\{a_k, a_l^\dagger\} = \delta_{kl}
\tag{3.39}
$$

After defining creation $a^\dagger$ and annihilation a operators with corresponding anti-commutation relations, we are ready to create generic operators such as one electron O_{p1} and coulomb repulsion operator O_{p2} with corresponding matrix elements as:

$$
O_{p1} = \sum_{k,l} < k \mid t \mid l > a_k^\dagger a_l
\tag{3.40}
$$

$$O_{p2} = \frac{1}{2} \sum_{k,l,m,n} < kl \mid V \mid mn > a_k^\dagger a_l^\dagger a_m a_n \tag{3.41}$$

where $< k \mid t \mid l >$ and $< kl \mid V \mid mn >$ are matrix elements.

To see the effect of generic operators on an arbitrary wave function and express simplicity of second quantization method, we use Hartree-Fock ground state wave function $\mid \Psi_{GS} >$ (Hartree, 1928; Fock, 1930) as:

$$< \Psi_{GS} \mid O_{p1} \mid \Psi_{GS} >= \sum_{k,l} < k \mid t \mid l >< \Psi_{GS} \mid a_k^\dagger a_l \mid \Psi_{GS} > \tag{3.42}$$

and by using anti-commutation relation, we can write:

$$< \Psi_{GS} \mid a_k^\dagger a_l \mid \Psi_{GS} >= \delta_{kl} < \Psi_{GS} \mid \Psi_{GS} > - < \Psi_{GS} \mid a_l a_k^\dagger \mid \Psi_{GS} > \tag{3.43}$$

second term is zero since an electron can not be created twice in the same orbital and we are left with only first term which is equal to δ_{kl}. We can write final expression as:

$$< \Psi_{GS} \mid O_{p1} \mid \Psi_{GS} > = \sum_{k,l} < k \mid t \mid l > \delta_{kl}$$
$$= \sum_{k} < k \mid t \mid k > . \tag{3.44}$$

For the case of two electron operator, we can proceed as:

$$< \Psi_{GS} \mid O_{p2} \mid \Psi_{GS} >= \frac{1}{2} \sum_{k,l,m,n} < kl \mid V \mid mn >< \Psi_{GS} \mid a_k^\dagger a_l^\dagger a_m a_n \mid \Psi_{GS} > \tag{3.45}$$

and using anti-commutation relation and changing the order of creation and annihilation operators, we obtain:

$$< \Psi_{GS} \mid a_k^\dagger a_l^\dagger a_m a_n \mid \Psi_{GS} >=$$
$$\delta_{ln} < \Psi_{GS} \mid a_k^\dagger a_m^\dagger \mid \Psi_{GS} > - < \Psi_{GS} \mid a_k^\dagger a_n a_l^\dagger a_m \mid \Psi_{GS} >$$
$$= \delta_{ln}\delta_{km} < \Psi_{GS} \mid \Psi_{GS} > -\delta_{ln} < \Psi_{GS} \mid a_m a_k^\dagger \mid \Psi_{GS} >$$
$$- \delta_{lm} < \Psi_{GS} \mid a_k^\dagger a_n \mid \Psi_{GS} > + < \Psi_{GS} \mid a_k^\dagger a_n a_m a_l^\dagger \mid \Psi_{GS} >= \delta_{ln}\delta_{km} - \delta_{lm}\delta_{kn}$$
$$\tag{3.46}$$

and we get:

$$< \Psi_{GS} \mid O_{p2} \mid \Psi_{GS} >= \frac{1}{2} \sum_{k,l} [< kl \mid V \mid kl > - < kl \mid V \mid lk >] \tag{3.47}$$

3.3. Mean-Field Hubbard Model

Armed with second quantization technique, we can proceed to construct mean-field Hubbard model. We will start with general many-body Hamiltonian which includes one and two electron operator as:

$$H = \sum_{pq} <p \mid t \mid q> a_p^\dagger a_q + \frac{1}{2} \sum_{pqrs} <pq \mid V \mid rs> a_p^\dagger a_q^\dagger a_r a_s. \qquad (3.48)$$

By using general Hamiltonian above, we can write new Hamiltonian in order to show spin degrees explicitly. We will change indices as $p = (k\sigma_1)$, $q = (l\sigma_2)$, $r = (m\sigma_3)$ and $s = (n\sigma_4)$ where σ_i's indicate spin degrees. Then, we can rewrite matrix elements as:

$$\begin{aligned}
t_{pq} &= <p \mid t \mid q> \\
&= <k\sigma_1 \mid t \mid l\sigma_2> \\
&= <k \mid t \mid l><\sigma_1 \mid \sigma_2> \quad \text{here, } t \text{ is assumed to be spin-free} \\
&= <k \mid t \mid l> \delta_{\sigma_1 \sigma_2} \\
&= <k \mid t \mid l> = t_{kl} \qquad (3.49)
\end{aligned}$$

and

$$\begin{aligned}
<pq \mid V \mid rs> &= <k\sigma_1 l\sigma_2 \mid V \mid m\sigma_3 n\sigma_4> \\
&= <kl \mid V \mid mn><\sigma_1 \mid \sigma_4><\sigma_2 \mid \sigma_3> \quad \text{here, } V \text{ is spin-free} \\
&= <kl \mid V \mid mn> \delta_{\sigma_1 \sigma_4} \delta_{\sigma_2 \sigma_3} \\
&= <kl \mid V \mid mn>. \qquad (3.50)
\end{aligned}$$

Finally, our general Hamiltonian which is including spin explicitly can be written as:

$$H = \sum_{kl\sigma} t_{kl} a_{k\sigma}^\dagger a_{l\sigma} + \frac{1}{2} \sum_{klmn,\sigma\sigma'} <kl \mid V \mid mn> a_{k\sigma}^\dagger a_{l\sigma'}^\dagger a_{m\sigma'} a_{n\sigma}. \qquad (3.51)$$

In order to continue our derivation to mean-field Hubbard, we will try to keep specific terms of 2 electron operator such as $<kk \mid V \mid kk> = U$ and $<lk \mid V \mid kl> = V_{kl}$ and neglect other terms. Hence, we write:

$$\frac{U}{2} \sum_{k,\sigma\sigma'} a_{k\sigma}^\dagger a_{k\sigma'}^\dagger a_{k\sigma'} a_{k\sigma} = \frac{1}{2} \sum_{k,\sigma\sigma'} <kk \mid V \mid kk> a_{k\sigma}^\dagger a_{k\sigma'}^\dagger a_{k\sigma'} a_{k\sigma} \qquad (3.52)$$

and then, by using anti-commutation relations and defining number operator $n_{k\sigma} = a_{k\sigma}^\dagger a_{k\sigma}$,

we can rearrange the terms in eqn. (3.52) as:

$$\frac{U}{2} \sum_{k,\sigma\sigma'} [a_{k\sigma}^\dagger a_{k\sigma'}^\dagger a_{k\sigma'} a_{k\sigma}] = \frac{U}{2} \sum_{k,\sigma\sigma'} [a_{k\sigma}^\dagger a_{k\sigma'}^\dagger (-a_{k\sigma} a_{k\sigma'})]$$

$$= \frac{U}{2} \sum_{k,\sigma\sigma'} [-a_{k\sigma}^\dagger (\delta_{\sigma\sigma'} - a_{k\sigma} a_{k\sigma'}^\dagger) a_{k\sigma'}]$$

$$= \frac{U}{2} \sum_{k,\sigma\sigma'} [-a_{k\sigma}^\dagger a_{k\sigma'} \delta_{\sigma\sigma'} + a_{k\sigma}^\dagger a_{k\sigma} a_{k\sigma'}^\dagger a_{k\sigma'}]$$

$$= \frac{U}{2} \sum_{k,\sigma\sigma'} [-a_{k\sigma}^\dagger a_{k\sigma} + a_{k\sigma}^\dagger a_{k\sigma} a_{k\sigma'}^\dagger a_{k\sigma'}]$$

$$= \frac{U}{2} \sum_{k,\sigma\sigma'} [a_{k\sigma}^\dagger a_{k\sigma} (-1 + a_{k\sigma'}^\dagger a_{k\sigma'})]$$

$$= \frac{U}{2} \sum_{k,\sigma'} [n_{k\uparrow}(n_{k\sigma'} - 1) + n_{k\downarrow}(n_{k\sigma'} - 1)]$$

$$= \frac{U}{2} \sum_{k} [n_{k\uparrow}(n_{k\uparrow} + n_{k\downarrow} - 1) + n_{k\downarrow}(n_{k\uparrow} + n_{k\downarrow} - 1)]$$

$$= \frac{U}{2} \sum_{k} [n_{k\uparrow}(n_{k\uparrow} - 1) + n_{k\downarrow}(n_{k\downarrow} - 1) + n_{k\uparrow}n_{k\downarrow} + n_{k\downarrow}n_{k\uparrow}]$$

$$= \frac{U}{2} \sum_{k,\sigma} n_{k\sigma} n_{k\bar\sigma} \text{ where } \bar\sigma \text{ refers to opposite spin} \qquad (3.53)$$

and $\frac{1}{2} \sum_{kl,\sigma\sigma'} < lk \mid V \mid kl > a_{k\sigma}^\dagger a_{l\sigma'}^\dagger a_{l\sigma'} a_{k\sigma}$ can be rearranged as:

$$\frac{1}{2} \sum_{kl,\sigma\sigma'} < lk \mid V \mid kl > a_{k\sigma}^\dagger a_{l\sigma'}^\dagger a_{l\sigma'} a_{k\sigma} = \frac{1}{2} \sum_{kl,\sigma\sigma'} V_{kl} a_{k\sigma}^\dagger a_{l\sigma'}^\dagger (-a_{k\sigma} a_{l\sigma'})$$

$$= \frac{1}{2} \sum_{kl,\sigma\sigma'} V_{kl} a_{k\sigma}^\dagger a_{k\sigma} a_{l\sigma'}^\dagger a_{l\sigma} = \frac{1}{2} \sum_{kl,\sigma\sigma'} V_{kl} n_{k\sigma} n_{l\sigma'}. \qquad (3.54)$$

and we rewrite eqn. (3.51) as:

$$H = \overbrace{\sum_{kl\sigma} t_{kl} a_{k\sigma}^\dagger a_{l\sigma} + \frac{U}{2} \sum_{k,\sigma} n_{k\sigma} n_{k\bar\sigma}}^{\text{Hubbard model}} + \underbrace{\frac{1}{2} \sum_{kl,\sigma\sigma'} V_{kl} n_{k\sigma} n_{l\sigma'}}_{\text{Extended Hubbard model}}. \qquad (3.55)$$

We can continue by using $n_{k\sigma} = n_{k\uparrow} + n_{k\downarrow}$ and $n_{k\uparrow}n_{k\downarrow} \mid \quad >= n_{k\downarrow}n_{k\uparrow} \mid \quad >$ as:

$$\frac{U}{2} \sum_{k,\sigma} n_{k\sigma} n_{k\bar\sigma} = \frac{U}{2} \sum_{k,\sigma} (n_{k\uparrow}n_{k\downarrow} + n_{k\downarrow}n_{k\uparrow})$$

$$= \frac{U}{2} \sum_{k} 2(n_{k\uparrow}n_{k\downarrow})$$

$$= U \sum_{k} n_{k\uparrow}n_{k\downarrow} \qquad (3.56)$$

and

$$\frac{1}{2}\sum_{kl,\sigma\sigma'}V_{kl}n_{k\sigma}n_{l\sigma'} = \frac{1}{2}\sum_{kl}V_{kl}[n_{k\uparrow}n_{l\uparrow} + n_{k\downarrow}n_{l\downarrow} + n_{k\uparrow}n_{l\downarrow} + n_{k\downarrow}n_{l\uparrow}]$$

$$= \frac{1}{2}\sum_{kl}V_{kl}[n_{k\uparrow}(n_{l\uparrow} + n_{k\downarrow}) + n_{k\downarrow}(n_{l\uparrow} + n_{k\downarrow})]$$

$$= \frac{1}{2}\sum_{kl}V_{kl}[(n_{k\uparrow} + n_{k\downarrow})(n_{l\uparrow} + n_{l\downarrow})]$$

$$= \frac{1}{2}\sum_{kl}V_{kl}n_k n_l \tag{3.57}$$

and we rewrite eqn. (3.55) as:

$$H = \sum_{kl\sigma}t_{kl}a_{k\sigma}^{\dagger}a_{l\sigma} + U\sum_{k}n_{k\uparrow}n_{k\downarrow} + \frac{1}{2}\sum_{\substack{kl\\k\neq l}}V_{kl}n_k n_l \tag{3.58}$$

Afterwards, we take $n_{k\uparrow} =< n_{k\uparrow} > +(n_{k\uparrow} - < n_{k\uparrow} >)$ and assume $\Delta n_{k\sigma} = (n_{k\sigma} - < n_{k\sigma} >)$ is negligibly small and rewrite each term of eqn. (3.58) as:

$$U\sum_{k}n_{k\uparrow}n_{k\downarrow} = U\sum_{k}(< n_{k\uparrow} > +\Delta n_{k\downarrow})(< n_{k\downarrow} > +\Delta n_{k\downarrow})$$

$$= U\sum_{k}[< n_{k\uparrow} >< n_{k\downarrow} >$$

$$+ < n_{k\uparrow} > \Delta n_{k\downarrow} + < n_{k\downarrow} > \Delta n_{k\uparrow} + \Delta n_{k\uparrow}\Delta n_{k\downarrow}]$$

$$= U\sum_{k}[< n_{k\uparrow} >< n_{k\downarrow} >$$

$$+ < n_{k\uparrow} > n_{k\downarrow} - < n_{k\uparrow} >< n_{k\downarrow} > + < n_{k\downarrow} > n_{k\uparrow} - < n_{k\uparrow} >< n_{k\downarrow} >]$$

$$= U\sum_{k}[< n_{k\uparrow} > n_{k\downarrow} + < n_{k\downarrow} > n_{k\uparrow} - < n_{k\uparrow} >< n_{k\downarrow} >] \tag{3.59}$$

and

$$\frac{1}{2}\sum_{\substack{kl\\k\neq l}}V_{kl}n_k n_l = \frac{1}{2}\sum_{\substack{kl\\k\neq l}}V_{kl}(< n_k > +\Delta n_k)(< n_l > +\Delta n_l)$$

$$= \frac{1}{2}\sum_{\substack{kl\\k\neq l}}V_{kl}[< n_k >< n_l > + < n_k > \Delta n_l + < n_l > \Delta n_k + \Delta n_k\Delta n_l]$$

$$= \frac{1}{2}\sum_{\substack{kl\\k\neq l}}V_{kl}[< n_k >< n_l > + < n_k > n_l - < n_k >< n_l > + < n_l > n_k$$

$$- < n_l >< n_k >]$$

$$= \frac{1}{2}\sum_{\substack{kl\\k\neq l}}V_{kl}[< n_k > n_l + < n_l > n_k - < n_k >< n_l >] \tag{3.60}$$

and we rewrite eqn. (3.58) as:

$$H = \sum_{kl\sigma} t_{kl} a_{k\sigma}^\dagger a_{l\sigma}$$
$$+ U \sum_k [< n_{k\uparrow} > n_{k\downarrow} + < n_{k\downarrow} > n_{k\uparrow} - < n_{k\uparrow} >< n_{k\downarrow} >]$$
$$+ \frac{1}{2} \sum_{\substack{kl \\ k \neq l}} V_{kl} [< n_k > n_l + < n_l > n_k - < n_k >< n_l >]. \qquad (3.61)$$

Before proceeding to mean-field Hamiltonian, we need to make some assumptions with charge and spin densities as $< n_k >= 1$ and $< n_{k\sigma} >= 1/2$, respectively. Hence, eqn. (3.61) can be rewritten with this assumptions as:

$$H_{MF}^b = \sum_{kl\sigma} t_{kl} a_{k\sigma}^\dagger a_{l\sigma} + U \sum_k [\frac{n_{k\downarrow}}{2} + \frac{n_{k\uparrow}}{2} - \frac{1}{4}] + \frac{1}{2} \sum_{\substack{kl \\ k \neq l}} V_{kl} [n_l + n_k - 1] \qquad (3.62)$$

and we write:

$$H = H + H_{MF}^b - H_{MF}^b$$
$$= \sum_{kl\sigma} t_{kl} a_{k\sigma}^\dagger a_{l\sigma} + U \sum_k [< n_{k\uparrow} > n_{k\downarrow} + < n_{k\downarrow} > n_{k\uparrow} - < n_{k\uparrow} >< n_{k\downarrow} >]$$
$$+ \frac{1}{2} \sum_{\substack{kl \\ k \neq l}} V_{kl} [< n_k > n_l + < n_l > n_k - < n_k >< n_l >]$$
$$+ \sum_{kl\sigma} t_{kl} a_{k\sigma}^\dagger a_{l\sigma} + U \sum_k [\frac{n_{k\downarrow}}{2} + \frac{n_{k\uparrow}}{2} - \frac{1}{4}] + \frac{1}{2} \sum_{\substack{kl \\ k \neq l}} V_{kl} [n_l + n_k - 1]$$
$$- \sum_{kl\sigma} t_{kl} a_{k\sigma}^\dagger a_{l\sigma} - U \sum_k [\frac{n_{k\downarrow}}{2} + \frac{n_{k\uparrow}}{2} - \frac{1}{4}] - \frac{1}{2} \sum_{\substack{kl \\ k \neq l}} V_{kl} [n_l + n_k - 1]. \qquad (3.63)$$

After rearranging eqn. (3.63), we get:

$$H = \sum_{kl\sigma} t_{kl}' a_{k\sigma}^\dagger a_{l\sigma} + U \sum_{k,\sigma} [(< n_{k\sigma} > - \frac{1}{2}) n_{k\bar\sigma}] + \sum_{\substack{kl,\sigma \\ k \neq l}} V_{kl} [(< n_k > - 1) n_{l\sigma}] + K$$

$$(3.64)$$

where $t' = \sum_{kl\sigma} t_{kl} a_{k\sigma}^\dagger a_{l\sigma} + U \sum_k [\frac{n_{k\downarrow}}{2} + \frac{n_{k\uparrow}}{2}] + \frac{1}{2} \sum_{\substack{kl \\ k \neq l}} V_{kl} [n_l + n_k]$ and $K = -U \sum_k [< n_{k\uparrow} >< n_{k\downarrow} >] - \frac{1}{2} \sum_{\substack{kl \\ k \neq l}} V_{kl} [< n_l >< n_k >]$. From now on we will rewrite t' as t which is a conventional notation for hopping parameter in the literature and we will neglect constant term K which has no effect on Hamiltonian. Hence, we can write our mean-field Hubbard Hamiltonian as:

$$H_{MF} = \sum_{kl\sigma} t_{kl} a_{k\sigma}^\dagger a_{l\sigma} + U \sum_{k,\sigma} [(< n_{k\sigma} > - \frac{1}{2}) n_{k\bar\sigma}] + \sum_{\substack{kl,\sigma \\ k \neq l}} V_{kl} [(< n_k > - 1) n_{l\sigma}]. \quad (3.65)$$

H_{MF} is a single-body Hamiltonian which is computationally much more easy to deal with compared to many-body Hamiltonian in eqn. (3.48).

3.4. Configuration Interaction Method

The many-body Hamiltonian written in eqn. (3.48) can not be solved for more than several particles and orbitals due to computational limits. Hence, we have made mean-field approximation to convert eqn. (3.48) into computable structure. By doing mean-field approximation, however, one ignores exchange-correlation effects of particles. We use many-body configuration interaction method in order to include all interaction of different configurations (see Figure 3.4) while studying optical transitions. We start with defining Hamiltonian which includes several parts as :

$$H_{MB} = H_0 - H_{MF}^{HF} + H_{int} \tag{3.66}$$

where H_0 is Hartree-Fock (HF) self energy, H_{MF}^{HF} is HF mean-field interaction and H_{int} represents full interaction. HF self energy Hamiltonian is defined as:

$$H_0 = \sum_{p\sigma} \epsilon_p a_{p\sigma}^\dagger a_{p\sigma} + \sum_{p'\sigma} \epsilon_{p'} a_{p'\sigma}^\dagger a_{p'\sigma} \tag{3.67}$$

and HF mean-field interaction Hamiltonian as:

$$H_{MF}^{HF} = \sum_{\substack{pqs \\ \sigma\sigma'}} \{< pq \mid V \mid qs > -\delta_{\sigma\sigma'} < pq \mid V \mid sq >\} a_{p\sigma}^\dagger a_{s\sigma}$$

$$+ \sum_{\substack{p'qs' \\ \sigma\sigma'}} \{< p'q \mid V \mid qs' > -\delta_{\sigma\sigma'} < p'q \mid V \mid s'q >\} a_{p'\sigma}^\dagger a_{s'\sigma} \tag{3.68}$$

and full interaction Hamiltonian as:

$$H_{int} = \frac{1}{2} \sum_{\substack{pqrs \\ \sigma\sigma'}} < pq \mid V \mid rs > a_{p\sigma}^\dagger a_{q\sigma'}^\dagger a_{r\sigma'} a_{s\sigma}$$

$$+ \frac{1}{2} \sum_{\substack{p'q'r's' \\ \sigma\sigma'}} < p'q' \mid V \mid r's' > a_{p'\sigma}^\dagger a_{q'\sigma'}^\dagger a_{r'\sigma'} a_{s'\sigma}$$

$$+ \sum_{\substack{pq'r's \\ \sigma\sigma'}} \{< pq' \mid V \mid r's > -\delta_{\sigma\sigma'} < pq' \mid V \mid sr' >\} a_{p\sigma}^\dagger a_{q'\sigma'}^\dagger a_{r'\sigma'} a_{s\sigma} \tag{3.69}$$

where $p - p'$ interaction have been neglected due to the gap between valance and conduction band. Additionally, one can rewrite eqn. (3.66) as:

$$H_{MB} = H_0 + H_{ee} + H_{hh} + H_{eh} \tag{3.70}$$

where H_{ee}, H_{hh} and H_{eh} are electron-electron, hole-hole and electron-hole interaction terms, respectively. Hence, H_{ee}, H_{hh} and H_{eh} are defined as:

$$H_{ee} = \frac{1}{2} \sum_{\substack{p'q'r's' \\ \sigma\sigma'}} <p'q' \mid V \mid r's'> a^\dagger_{p'\sigma} a^\dagger_{q'\sigma'} a_{r'\sigma'} a_{s'\sigma}, \tag{3.71}$$

$$H_{hh} = \frac{1}{2} \sum_{\substack{pqrs \\ \sigma\sigma'}} <pq \mid V \mid rs> a^\dagger_{p\sigma} a^\dagger_{q\sigma'} a_{r\sigma'} a_{s\sigma}$$
$$- \sum_{\substack{pqs \\ \sigma\sigma'}} \{<pq \mid V \mid qs> -\delta_{\sigma\sigma'} <pq \mid V \mid sq>\} a^\dagger_{p\sigma} a_{s\sigma} \tag{3.72}$$

and

$$H_{eh} = \sum_{\substack{pq'r's \\ \sigma\sigma'}} \{<pq' \mid V \mid r's> -\delta_{\sigma\sigma'} <pq' \mid V \mid sr'>\} a^\dagger_{p\sigma} a^\dagger_{q'\sigma'} a_{r'\sigma'} a_{s\sigma}$$
$$- \sum_{\substack{p'qs' \\ \sigma\sigma'}} \{<p'q \mid V \mid qs'> -\delta_{\sigma\sigma'} <p'q \mid V \mid s'q>\} a^\dagger_{p'\sigma} a_{s'\sigma}. \tag{3.73}$$

By using anti-commutation relations, one can rewrite eqn. (3.72) as:

$$H_{hh} = \frac{1}{2} \sum_{\substack{pqrs \\ \sigma\sigma'}} <pq \mid V \mid rs> a^\dagger_{p\sigma} (\delta_{qr} - a_{r\sigma'} a^\dagger_{q\sigma'}) a_{s\sigma}$$
$$- \sum_{\substack{pqs \\ \sigma\sigma'}} \{<pq \mid V \mid qs> -\delta_{\sigma\sigma'} <pq \mid V \mid sq>\} a^\dagger_{p\sigma} a_{s\sigma}$$
$$= \frac{1}{2} \sum_{\substack{pqs \\ \sigma\sigma'}} <pq \mid V \mid qs> a^\dagger_{p\sigma} a_{s\sigma}$$
$$- \frac{1}{2} \sum_{\substack{pqrs \\ \sigma\sigma'}} <pq \mid V \mid rs> (\delta_{pr}\delta_{\sigma\sigma'} - a_{r\sigma'} a^\dagger_{p\sigma})(\delta_{qs}\delta_{\sigma\sigma'} - a_{s\sigma} a^\dagger_{q\sigma'})$$
$$- \sum_{\substack{pqs \\ \sigma\sigma'}} \{<pq \mid V \mid qs> -\delta_{\sigma\sigma'} <pq \mid V \mid sq>\} a^\dagger_{p\sigma} a_{s\sigma}$$
$$= \frac{1}{2} \sum_{\substack{pqs \\ \sigma\sigma'}} \{<pq \mid V \mid qs> -\delta_{\sigma\sigma'} <pq \mid V \mid sq>\} a^\dagger_{p\sigma} a_{s\sigma} + constants$$
$$- \frac{1}{2} \sum_{\substack{pqrs \\ \sigma\sigma'}} <pq \mid V \mid rs> a_{r\sigma'} a^\dagger_{p\sigma} a_{s\sigma} a^\dagger_{q\sigma'} + \frac{1}{2} \sum_{\substack{pqrs \\ \sigma\sigma'}} <pq \mid V \mid rq> a_{r\sigma'} a^\dagger_{p\sigma} \delta_{\sigma\sigma'}$$
$$- \sum_{\substack{pqs \\ \sigma\sigma'}} \{<pq \mid V \mid qs> -\delta_{\sigma\sigma'} <pq \mid V \mid sq>\} a^\dagger_{p\sigma} a_{s\sigma} \tag{3.74}$$

and ignoring the constant term, we get:

$$H_{hh} = \frac{1}{2} \sum_{\substack{pqrs \\ \sigma\sigma'}} <pq \mid V \mid rs> a_{r\sigma'} a_{s\sigma} a^\dagger_{p\sigma} a^\dagger_{q\sigma'}. \tag{3.75}$$

24

If we reorganize indicies and using hole representation $h_{p\bar{\sigma}} = a_{p\sigma}^\dagger$, the eqn. (3.75) becomes:

$$H_{hh} = \frac{1}{2} \sum_{\substack{pqrs \\ \sigma\sigma'}} <pq \mid V \mid rs> h_{r\sigma'}^\dagger h_{s\sigma}^\dagger h_{p\sigma} h_{q\sigma'}. \tag{3.76}$$

On the other hand, electron-hole interaction Hamiltonian can be rewritten as:
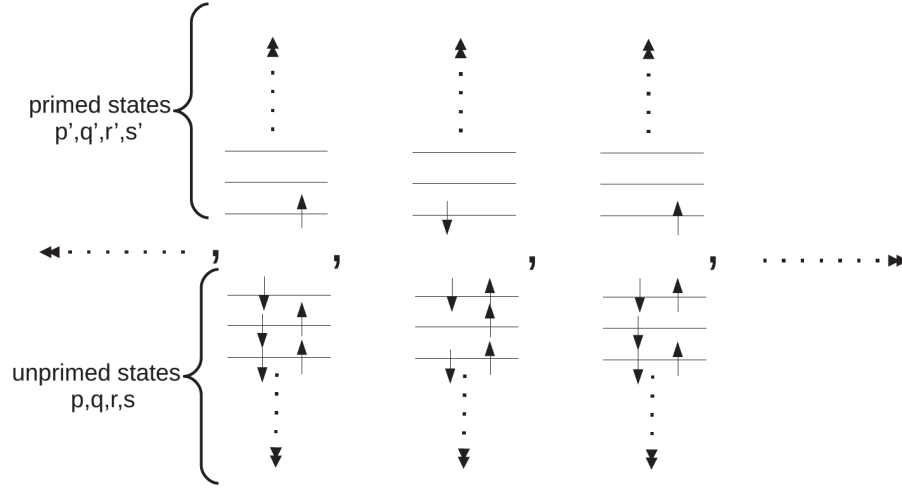
Figure 3.4. Cartoon of different configurations of excitation of particles to various molecular orbital levels. Primed states corresponds to conduction states and unprimed states corresponds to valance states.

$$
\begin{aligned}
H_{eh} &= \sum_{\substack{pq'r's \\ \sigma\sigma'}} \{< pq' \mid V \mid r's > -\delta_{\sigma\sigma'} < pq' \mid V \mid sr' >\} a_{p\sigma}^\dagger a_{q'\sigma'}^\dagger a_{r'\sigma'} a_{s\sigma} \\
&\quad - \sum_{\substack{p'qs' \\ \sigma\sigma'}} \{< p'q \mid V \mid qs' > -\delta_{\sigma\sigma'} < p'q \mid V \mid s'q >\} a_{p'\sigma}^\dagger a_{s'\sigma} \\
&= \sum_{\substack{p'qs' \\ \sigma\sigma'}} \{< p'q \mid V \mid qs' > -\delta_{\sigma\sigma'} < p'q \mid V \mid s'q >\} a_{p'\sigma}^\dagger a_{s'\sigma} \\
&\quad - \sum_{\substack{pq'r's \\ \sigma\sigma'}} \{< pq' \mid V \mid r's > -\delta_{\sigma\sigma'} < pq' \mid V \mid sr' >\} a_{q'\sigma'}^\dagger a_{s\sigma'} a_{p\sigma'}^\dagger a_{r'\sigma} \\
&\quad - \sum_{\substack{p'qs' \\ \sigma\sigma'}} \{< p'q \mid V \mid qs' > -\delta_{\sigma\sigma'} < p'q \mid V \mid s'q >\} a_{p'\sigma}^\dagger a_{s'\sigma} \tag{3.77}
\end{aligned}
$$

and switching to hole representation as:

$$H_{eh} = - \sum_{\substack{p'qrs' \\ \sigma\sigma'}} \{< rp' \mid V \mid s'q > -\delta_{\sigma\sigma'} < rp' \mid V \mid qs' >\} a^\dagger_{p'\sigma} h^\dagger_{q\bar{\sigma}'} h_{r\bar{\sigma}'} a_{s'\sigma} \quad (3.78)$$

and reorganizing all terms, one get final electron-hole interaction Hamiltonian as:

$$H_{eh} = - \sum_{\substack{p'qrs' \\ \sigma\sigma'}} \{< rp' \mid V \mid s'q > -(1 - \delta_{\sigma\sigma'}) < rp' \mid V \mid qs' >\} a^\dagger_{p'\sigma} h^\dagger_{q\sigma'} h_{r\sigma'} a_{s'\sigma}$$

$$+ \sum_{\substack{p',q,r,s' \\ \sigma,\bar{\sigma}}} < rp' \mid V \mid qs' > a^\dagger_{p'\bar{\sigma}} h^\dagger_{q\sigma} h_{r\bar{\sigma}} a_{s'\sigma}. \quad (3.79)$$

Lastly, eqn. (3.66) can be rewritten as:

$$H_{MB} = \sum_{p\sigma} \epsilon_p + \sum_{p'\sigma} \epsilon_{p'} a^\dagger_{p'\sigma} a_{p'\sigma} - \sum_{p\sigma} \epsilon_p h^\dagger_{p\sigma} h_{p\sigma}$$

$$+ \frac{1}{2} \sum_{\substack{p'q'r's' \\ \sigma\sigma'}} < p'q' \mid V \mid r's' > a^\dagger_{p'\sigma} a^\dagger_{q'\sigma'} a_{r'\sigma'} a_{s'\sigma}$$

$$+ \frac{1}{2} \sum_{\substack{pqrs \\ \sigma\sigma'}} < pq \mid V \mid rs > h^\dagger_{r\sigma'} h^\dagger_{s\sigma} h_{p\sigma} h_{q\sigma'}$$

$$- \sum_{\substack{p'qrs' \\ \sigma\sigma'}} \{< rp' \mid V \mid s'q > -(1 - \delta_{\sigma\sigma'}) < rp' \mid V \mid qs' >\} a^\dagger_{p'\sigma} h^\dagger_{q\sigma'} h_{r\sigma'} a_{s'\sigma}$$

$$+ \sum_{\substack{p',q,r,s' \\ \sigma,\bar{\sigma}}} < rp' \mid V \mid qs' > a^\dagger_{p'\bar{\sigma}} h^\dagger_{q\sigma} h_{r\bar{\sigma}} a_{s'\sigma}. \quad (3.80)$$

where first term is vacuum energy, second and third terms are electron and hole self energies, fourth and fifth terms are electron-electron and hole-hole interaction terms, respectively, and sixth and seventh terms are electron-hole interaction terms.

After defining each component of MFH and CI Hamiltonian, one can continue to calculate corresponding matrix elements of one particle or two particle operators. As an example, we show matrix element calculation for the sixth term of CI Hamiltonian which has components as:

$$\sum_{\substack{p'qrs' \\ \sigma\sigma'}} \{< rp' \mid V \mid s'q > -(1 - \delta_{\sigma\sigma'}) < rp' \mid V \mid qs' >\} a^\dagger_{p'\sigma} h^\dagger_{q\sigma'} h_{r\sigma'} a_{s'\sigma}. \quad (3.81)$$

We define two particle state $\mid \mu'_\sigma \nu_\sigma >$ where μ'_σ and ν_σ represents spin orbitals of electron and hole, respectively. Then, corresponding matrix elements of eqn. (3.81) can

$<kl\mid V\mid mn>$	E (eV)
$<11\mid V\mid 11>$	16.522
$<12\mid V\mid 21>$	8.640
$<13\mid V\mid 31>$	5.333
$<11\mid V\mid 12>$	3.157
$<12\mid V\mid 31>$	1.735
$<12\mid V\mid 12>$	0.873
$<11\mid V\mid 22>$	0.873
$<22\mid V\mid 13>$	0.606

Table 3.1. Calculated matrix elements between electrons which resides on the corresponding lattice sites in graphene. Indicated numbers 1,2 and 3 refers to electrons on-sites, first nearest-neighbours and second nearest-neighbours, respectively.

be obtained as:

$$\sum_{\substack{p'qrs' \\ \sigma\sigma'}} \{...\} < \alpha_{\sigma_1}\beta'_{\sigma_2} \mid a^{\dagger}_{p'\sigma}h^{\dagger}_{q\sigma'}h_{r\sigma'}a_{s'\sigma} \mid \mu'_{\sigma_3}\nu_{\sigma_4} >$$

$$= \sum_{\substack{p'qrs' \\ \sigma\sigma'}} \{...\} < \alpha_{\sigma_1}\beta'_{\sigma_2} \mid a^{\dagger}_{p'\sigma}h^{\dagger}_{q\sigma'}h_{r\sigma'} \mid \mu'_{\sigma_3}\nu_{\sigma_4} > \delta_{s'\mu'}\delta_{\sigma\sigma_3}$$

$$= \sum_{\substack{p'qrs' \\ \sigma\sigma'}} \{...\} < \alpha_{\sigma_1}\beta'_{\sigma_2} \mid a^{\dagger}_{p'\sigma}h^{\dagger}_{q\sigma'} \mid 0 > \delta_{r\nu}\delta_{\sigma'\sigma_4}\delta_{s'\mu'}\delta_{\sigma\sigma_3}$$

$$= \sum_{\substack{p'qrs' \\ \sigma\sigma'}} \{...\} < \alpha_{\sigma_1}\beta'_{\sigma_2} \mid a^{\dagger}_{p'\sigma} \mid q_{\sigma'} > \delta_{r\nu}\delta_{\sigma'\sigma_4}\delta_{s'\mu'}\delta_{\sigma\sigma_3}$$

$$= \sum_{\substack{p'qrs' \\ \sigma\sigma'}} \{...\} < \alpha_{\sigma_1}\beta'_{\sigma_2} \mid p'_{\sigma}q_{\sigma'} > \delta_{r\nu}\delta_{\sigma'\sigma_4}\delta_{s'\mu'}\delta_{\sigma\sigma_3}$$

$$= \sum_{\substack{p'qrs' \\ \sigma\sigma'}} \{...\}\delta_{p'\beta'}\delta_{\sigma\sigma_2}\delta_{q\alpha}\delta_{\sigma_2\sigma_1}\delta_{r\nu}\delta_{\sigma'\sigma_4}\delta_{s'\mu'}\delta_{\sigma\sigma_3}$$

$$= \{< \nu\beta' \mid V \mid \mu'\alpha > - < \nu\beta' \mid V \mid \alpha\mu' >\} \tag{3.82}$$

and the two-body electron-hole scattering matrix elements are calculated from two-body on-site and long-range Coulomb matrix elements (see Table **??**) (Güçlü *et al.*, 2009; Potasz *et al.*, 2010; Güçlü *et al.*, 2016) from which one can continue to construct Hamiltonian matrix to be diagonalized. The programming language which has been used to diagonalize Hamiltonian matrices is MATLAB and detailed information about codes can be seen in Appendix.

CHAPTER 4

OPTICAL PROPERTIES

In this chapter, we try to understand absorption properties of GQDs by using tight-binding, mean-field Hubbard and configuration methods.
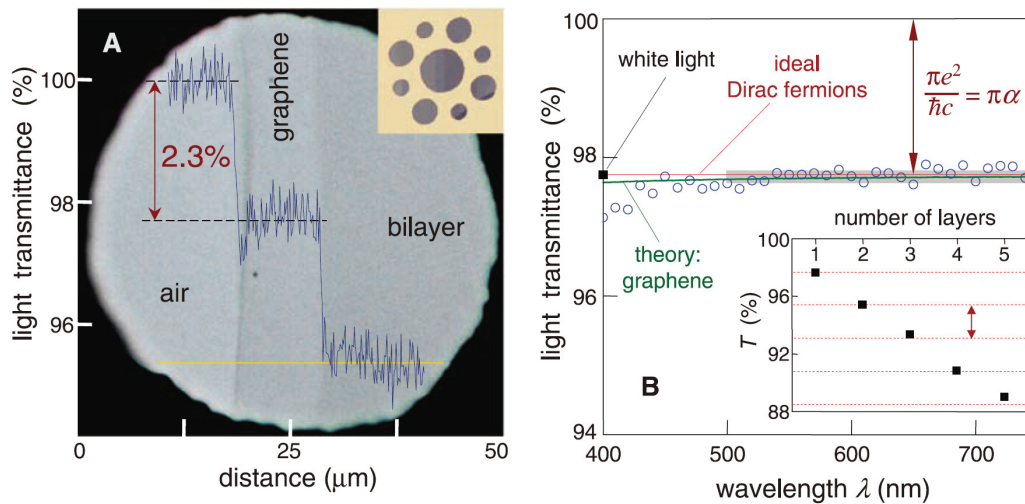
Figure 4.1. Picture of a graphene sample. The value 2.3% is an indication of universal optical conductivity observed in graphene. (Source: Nair *et al.*, 2008).

We describe absorption properties of graphene nanostructures and effects of charge impurities and electron-electron interaction on the optical properties of GQDs.

4.1. Absorption

Graphene shows explicit manifestation of light and matter interaction by having universal optical conductivity (UOC) $(\pi/2)e^2/\hbar = 0.023$ which provides graphene with striking optical characteristics as can bee seen in Figure 4.1 (Nair *et al.*, 2008; Kuzmenko *et al.*, 2008; Yuan *et al.*, 2011).

The experimental observation of UOC for a graphene sheet seems to indicate that
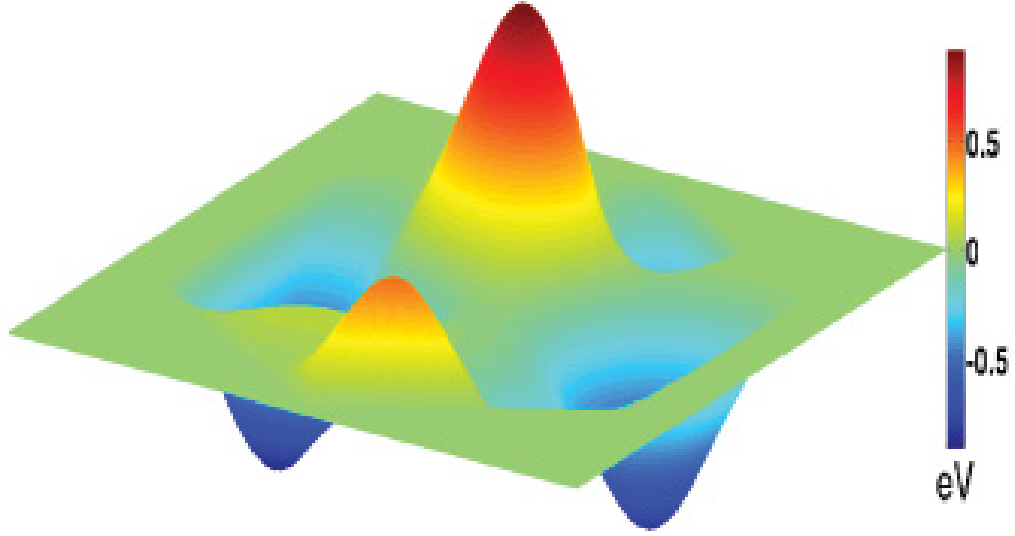
Figure 4.2. Impurity Potential Landscape. Positive potential hills shown by red color and negative potential hills by blue color.

optical properties are robust against imperfections, although significant deviations from UOC at lower energies was observed (Mak *et al.*, 2011; Lee *et al.*, 2011).

The interaction of light and matter can be quite well understood by perturbation theory of quantum mechanics (Dirac, 1927; Saqurai, 1994). Hamiltonian of a particle interacted with a radiation field can be approximated as:

$$H = \frac{p^2}{2m_e} + e\phi(\mathbf{r}) - \frac{e}{m_e c}\mathbf{A} \cdot \mathbf{p} \qquad (4.1)$$

where e, m_e, p, $\phi(\mathbf{r})$, c and $\mathbf{A}$ indicate charge, mass, momentum of the electron, electric potential, speed of light and vector potential of the field, respectively, and we have neglected higher order terms. By considering monochromatic field of plane wave, one can write:

$$\mathbf{A} = 2A_0 \mathbf{n} \cos\left(\frac{w}{c}\mathbf{l} \cdot \mathbf{r} - wt\right) \qquad (4.2)$$
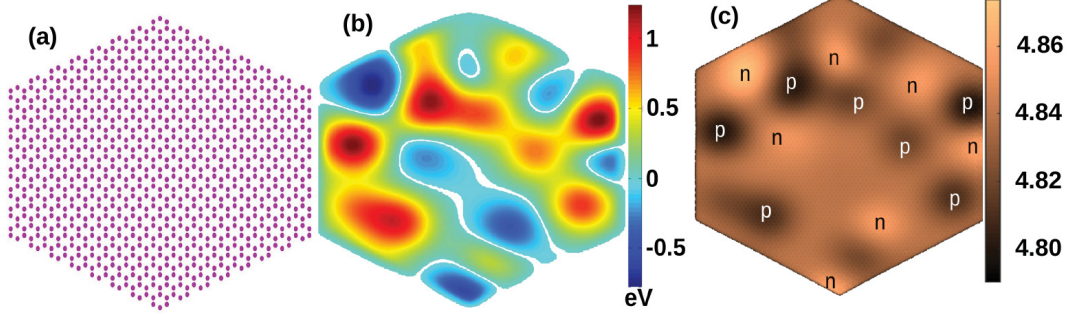
Figure 4.3. (a) Lattice structure of hexagonal armchair edged GQD. (b) Impurity potential landscape. (c) Electron-hole puddle formation achieved by MFH model where local charge accumulation is indicated as n and p puddles.

where $\mathbf{n}$, $\mathbf{l}$, $\mathbf{r}$, w and t refer to unit vector of polarization, unit vector of propagation, position vector, frequency and time, respectively. We rewrite eqn. (4.2) by using Euler relation for trigonometric functions as:

$$\mathbf{A} = A_0\mathbf{n} \left[e^{i(\frac{w}{c}\mathbf{l}\cdot\mathbf{r}-wt)} + e^{-i(\frac{w}{c}\mathbf{l}\cdot\mathbf{r}-wt)} \right]. \tag{4.3}$$

The term $e^{i(\frac{w}{c}\mathbf{l}\cdot\mathbf{r}-wt)}$ is responsible for absorption, whereas, the other term $e^{-i(\frac{w}{c}\mathbf{l}\cdot\mathbf{r}-wt)}$ brings about stimulated emission. Hence, we can define absorption energy part as:

$$T_{i\to f} = \frac{2\pi}{\hbar} \frac{e^2}{m_e^2 c^2} |\mathbf{A_0}|^2 | < f|e^{i(\frac{w}{c}\mathbf{l}\cdot\mathbf{r}-wt)}\mathbf{n}\cdot\mathbf{p}|i > |^2 \delta(E_f - E_i - \hbar w) \tag{4.4}$$

where δ has been inserted to account for continuous distribution of states. Lastly, absorption cross section is defined as:

$$\frac{\text{Energy absorbed by the atom per unit time}}{\text{Energy flux due to electromagnetic wave}}. \tag{4.5}$$

We can obtain energy flux and and energy densities by using classical electromagnetic theory (Jackson, 1975; Griffiths, 1962) and write absorption cross section as:

$$a(w) = \frac{4\pi^2 e^2}{m_e^2 c w (Area)} | < f|e^{i(\frac{w}{c}\mathbf{l}\cdot\mathbf{r}-wt)}\mathbf{n}\cdot\mathbf{p}|i > |^2 \delta(E_f - E_i - \hbar w) \tag{4.6}$$

where $Area$ is the area of the structure exposed to radiation. We will make an electric dipole approximation as:

$$e^{i(\frac{w}{c}\mathbf{l}\cdot\mathbf{r}-wt)} \approx 1 \tag{4.7}$$
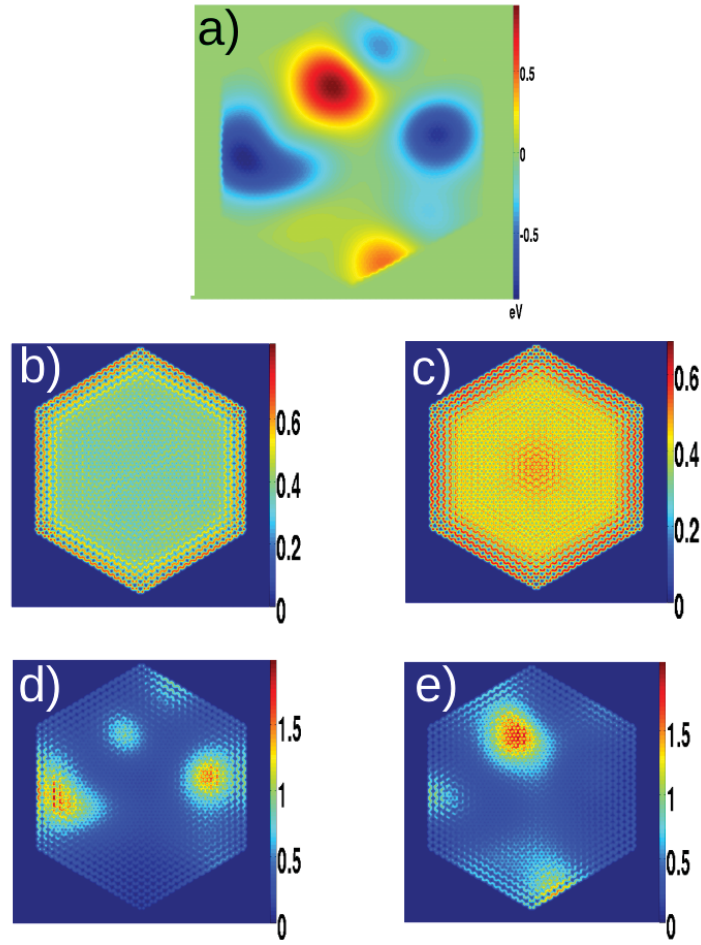
Figure 4.4. (a) Impurity potential landscape. TB results of (b) conduction and (c) valance states of clean sample made up of 5514 atoms. Corresponding puddle formation of (d) electron and (e) hole states of disordered sample.

since electromagnetic wavelength is much longer than the atomic dimensions and we are left with:

$$a(w) = \frac{4\pi^2 e^2}{m_e^2 cw(Area)} |\mathbf{n} \cdot <f|\mathbf{p}|i>|^2 \delta(E_f - E_i - \hbar w). \tag{4.8}$$

The x component of the term $|<f|\mathbf{p}|i>|$ can be written as:

$$<f|p_x|i> \tag{4.9}$$

and by using commutation relation:

$$[x, H_0] = \frac{i\hbar p_x}{m}, \tag{4.10}$$
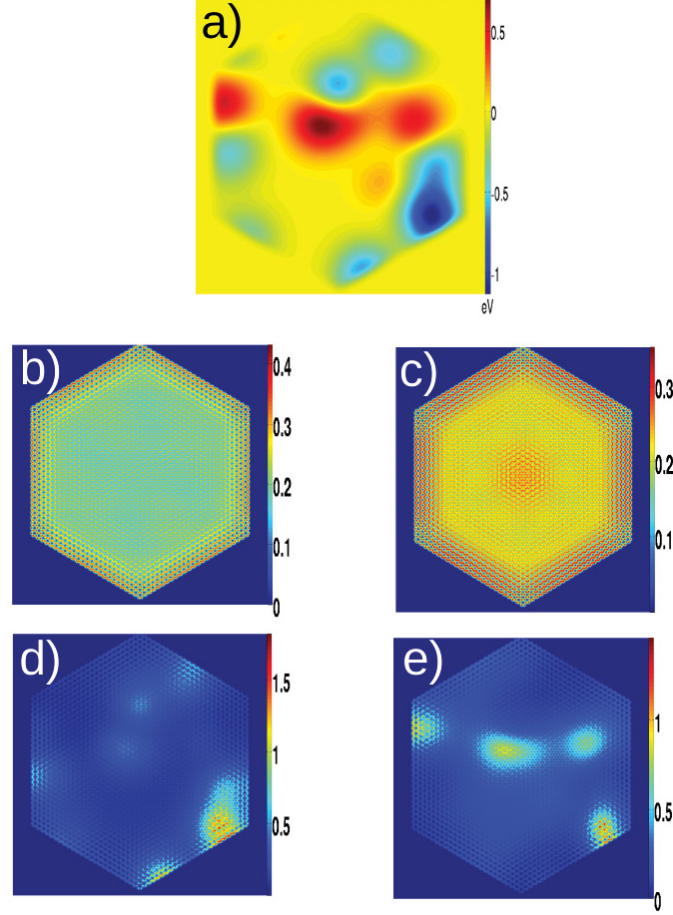
Figure 4.5. (a) Impurity potential landscape. TB results of (b) conduction and (c) valance states of clean sample made up of 10806 atoms. Corresponding puddle formation of (d) electron and (e) hole states of disordered sample.

one can write the x component of the term $|<f|\mathbf{p}|i>|$ as:

$$<f|p_x|i> = \frac{m}{i\hbar}<f|[x,H_0]|i>$$
$$= imE_{fi}<j|x|i> \tag{4.11}$$

where E_{fi} is energy difference between final and initial states obtained by TB or MFH model. As a result, we obtain total absorption for two dimensional material as:

$$A(\omega) = \sum_f \frac{4\pi^2\alpha E_{fi}|<f\mid\mathbf{r}\mid i>|^2\delta(\hbar\omega - E_{fi})}{Area} \tag{4.12}$$

where α is the fine structure which corresponds to $e^2/\hbar c \approx 1/137$. On the other hand, we
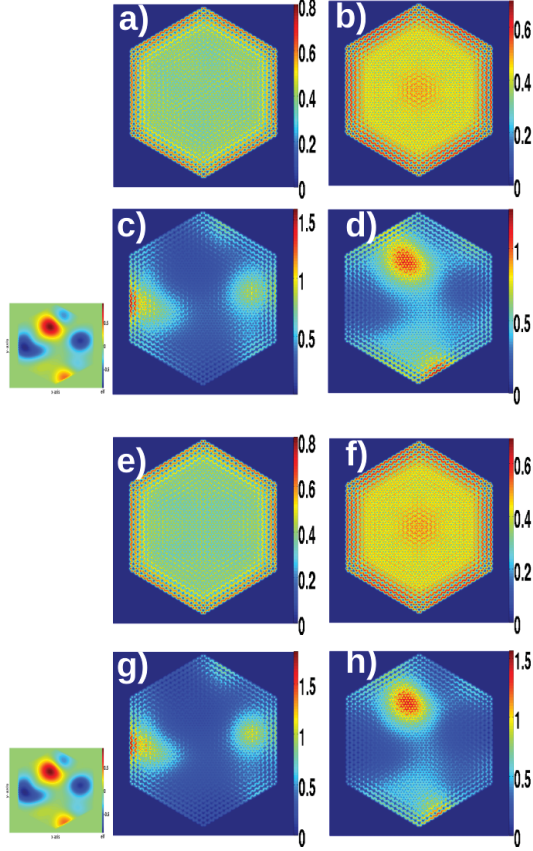
Figure 4.6. MFH results of (a, c, e and g) conduction and (b, d, f and h) valance states of (a, b and e, f) clean sample and (c, d and g, h) disordered sample made up of 5514 atoms. Corresponding puddle formation of (c,g) electron and (d,h) hole states of disordered sample. Figures a, b, c and d are for $\kappa = 3$ and e,f, g and h are for $\kappa = 6$. Potential landscape added as a smaller size picture to show corresponding potential hills and valleys.

define absorption spectrum which includes many-body correlations as:

$$A(\omega) = \sum_f \frac{4\pi^2 \alpha E_{fi} |< f \mid \mathbf{P}^\dagger \mid gs >|^2 \delta(\hbar\omega - E_{fi})}{Area} \tag{4.13}$$

where E_{fi} is the energy difference between initial (ground state) and final energies of exciton, $\mathbf{P}^\dagger$ annihilates a photon and adds an exciton to the ground state of the GQD. The final excitonic state $\mid f >$ is obtained from CI calculations, and $\mid gs >$ represents the ground state.
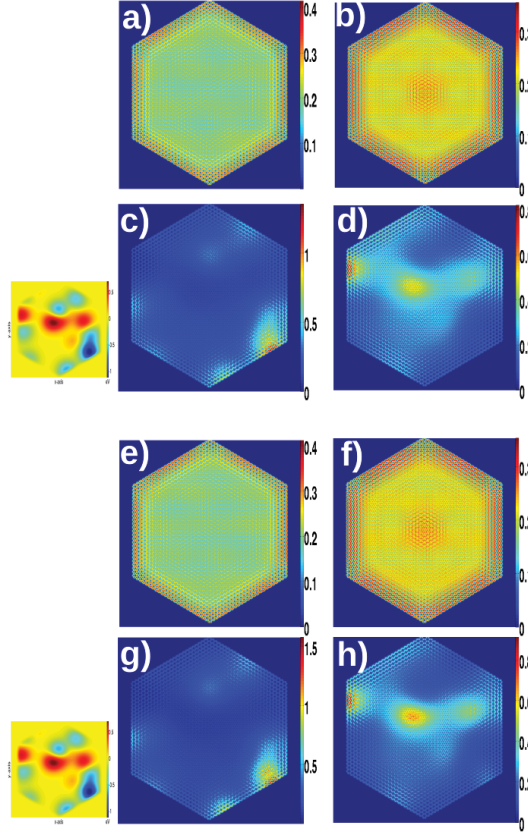
Figure 4.7. MFH results of (a, c, e and g) conduction and (b, d, f and h) valance states of (a, b and e, f) clean sample and (c, d and g, h) disordered sample made up of 10806 atoms. Corresponding puddle formation of (c,g) electron and (d,h) hole states of disordered sample. Figures a, b, c and d are for $\kappa = 3$ and e,f, g and h are for $\kappa = 6$. Potential landscape added as a smaller size picture to show corresponding potential hills and valleys.

4.2. Environment Related Charge Impurities

Properties of graphene nanostructures fabricated and observed upon substrates (Morpurgo and Guinea, 2006; Tan *et al.*, 2007; Morozov *et al.*, 2008; Jang *et al.*, 2008; Liao *et al.*, 2010; Lin *et al.*, 2010) may become affected by imperfections due to the environment and become disordered. In particular, if the disorder has a long-range character, it can lead to charge localizations as electron-hole puddles (Tan *et al.*, 2007; Zhang *et al.*, 2009; Lin *et al.*, 2010; Zhang *et al.*, 2009; Martin *et al.*, 2008; Gibertini *et al.*, 2012). For instance, magnetic properties of graphene nanoribbons are found to be strongly dependent
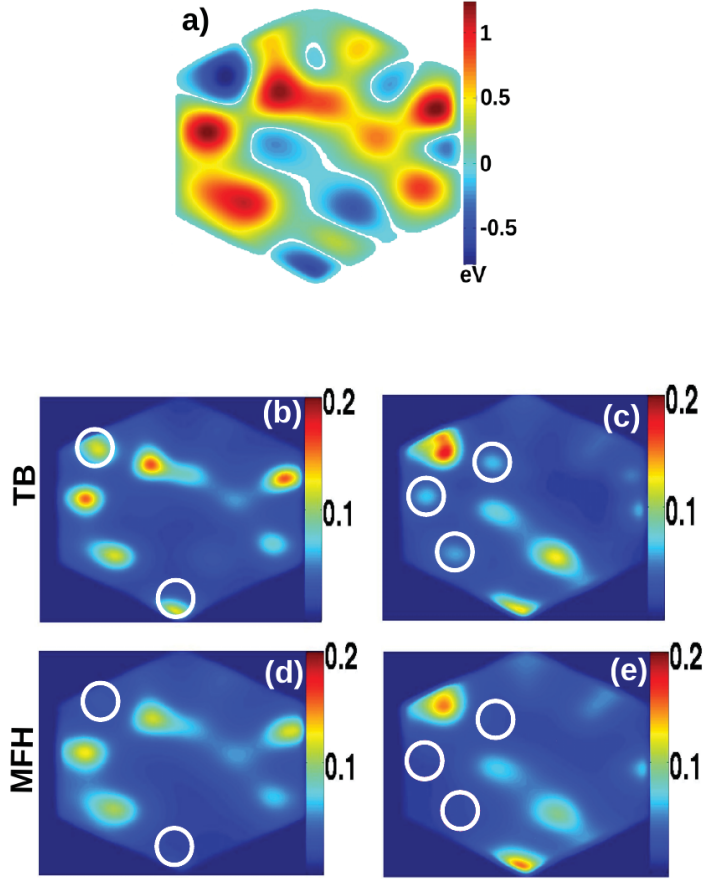
Figure 4.8. Electronic density corresponding to the 20 highest valence states (left panels), and the 20 lowest conduction states (right panels), obtained from TB (upper panels) and MFH (lower panels) model of the structure 18 nm width size. Electron-electron interactions wash out abnormal localized states near Fermi level as indicated by white circles.

of long-range impurities (Özdemir *et al.*, 2016). Additionally, the role of electron-hole puddles on the formation of Landau levels in a graphene double quantum dot was investigated experimentally by K. L. Chiu et al.(Chiu *et al.*, 2015). We use long-range disorders, in order to have reliable theoretical models for charge impurity effects on GQDs.

4.2.1. Long-Range Disorders

In order to model the long-range disorder due to charge impurities caused by substrate effects, we use a superposition of Gaussian electrostatic potentials V_{imp} which are
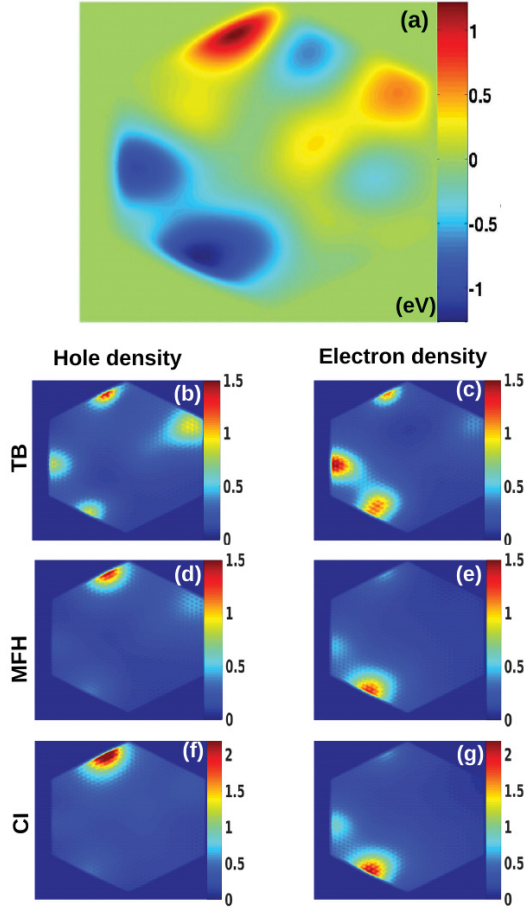
Figure 4.9. (a) Impurity potential for the structure containing 5514 atoms. (b-g) show corresponding electron and hole densities weighted with absorption probabilities in the energy range between 0 eV and 0.3 eV obtained by TB, MFH and CI models, respectively.

determined randomly to have a smooth potential landscape (see Figure 4.2) on the GQD. Impurity potential is written as:

$$V_{imp}(r_i) = \sum_k V_k \, exp\left[-\frac{(\vec{r_i} - \vec{R_k})^2}{2\sigma^2}\right] \tag{4.14}$$

where V_k is chosen to be the potential peak value which is randomly generated between $-V_{max} < V_k < V_{max}$ values for an impurity at R_k, characterizing the strength of the disorder. For most of the calculations, we take $V_{max} = t_{nn}/3$ giving a medium disorder strength. However, the effect of strong ($V_{max} = t_{nn}$) and weak ($V_{max} = t_{nn}/5$) disorder is also investigated (see Figure 4.14). The width of the potential, σ, is determined to be 10 times the lattice constant in order to simulate long-range lattice scatterers

36
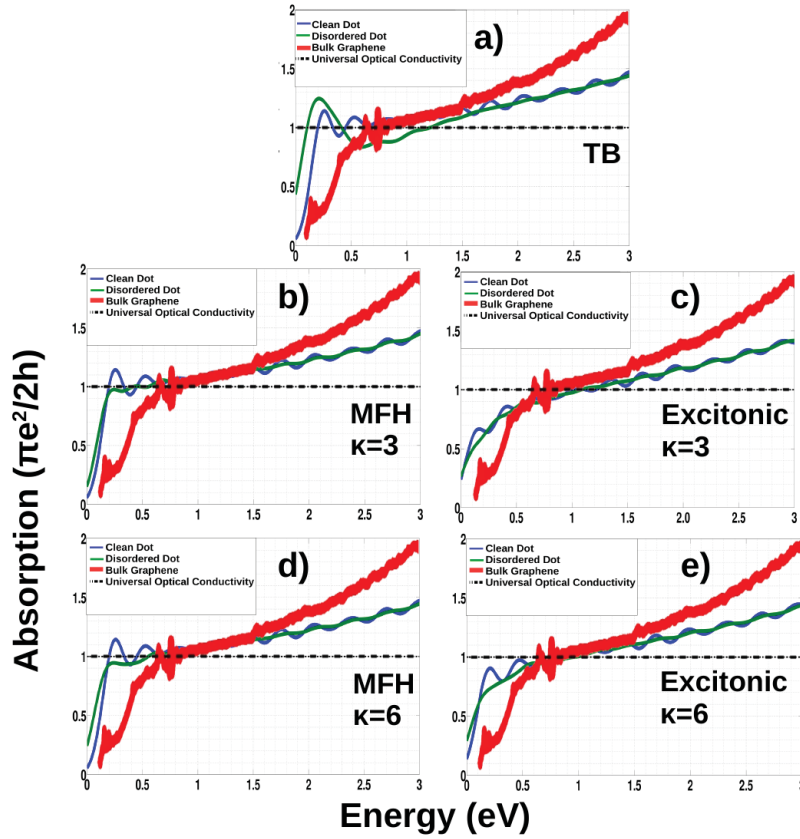
Figure 4.10. Absorption of GQD containing 5514 atoms. a) Clean dot (blue line) and disordered dot (green line) are obtained by obtained TB model and bulk graphene (red line) and UOC (dashed line) are shown, respectively. b) MFH model with $\kappa = 3$, d) with $\kappa = 6$. c) excitonic effect without correlation with $\kappa = 3$, d) with $\kappa = 6$.

(Zhang *et al.*, 2009; Altıntaş *et al.*, 2017). For 5 nm (1014 atoms), 13 nm (5514 atoms) and 18 (10806 atoms) nm wide GQDs, respectively 4, 20 and 40 source point of impurities are randomly created to have approximately similar source point densities (but different form of distribution of source points) for each GQD. The main effect of long-range disorder on the electronic densities is the formation of electron-hole puddles (Zhang *et al.*, 2009; Özdemir *et al.*, 2016; Altıntaş *et al.*, 2017), as seen from Figure **??**, obtained by subtraction of the positive background charge from MFH electronic density. The effect of the electron-hole puddles on the optical properties will be investigated in Section 4.3 using TB, MFH and CI approaches.
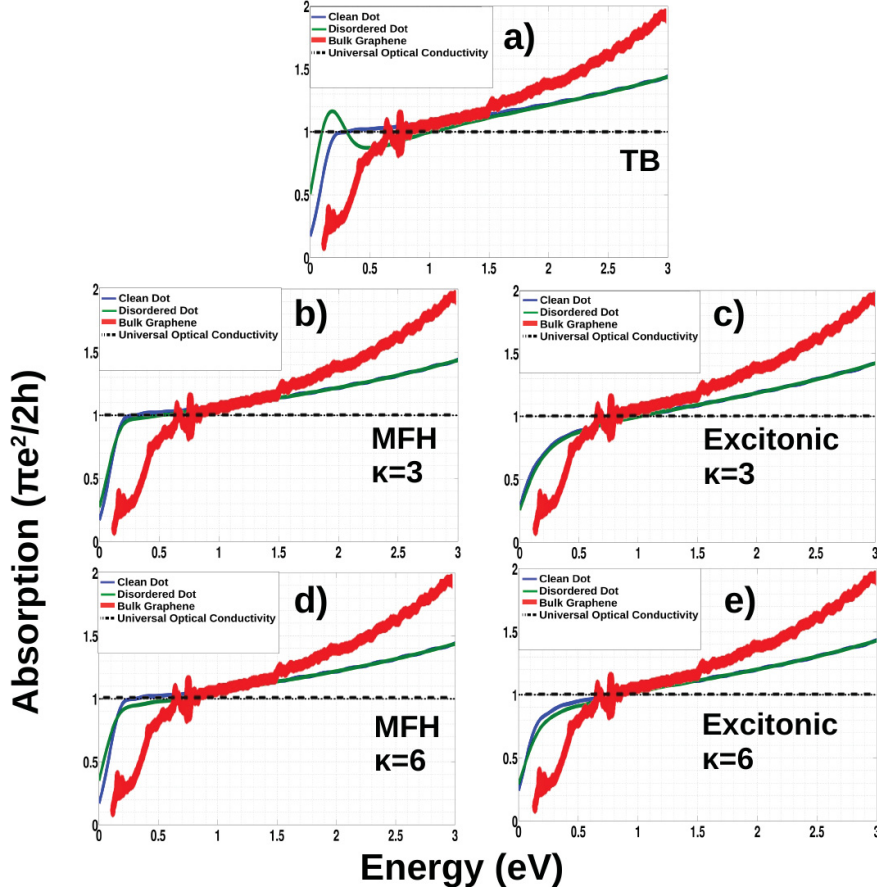
Figure 4.11. Absorption of GQD containing 10806 atoms. a) Clean dot (blue line) and disordered dot (green line) are obtained by obtained TB model and bulk graphene (red line) and UOC (dashed line) are shown, respectively. b) MFH model with $\kappa = 3$, d) with $\kappa = 6$. c) excitonic effect without correlation with $\kappa = 3$, d) with $\kappa = 6$.

4.3. Results and Discussion

In Figure 4.4 and 4.5, we investigate electronic densities corresponding to 20 lowest conduction and 20 highest valence states obtained from TB for the GQDs structure that we studied, which has 5514 and 10806 atoms giving a width of 13 nm and 18 nm with corresponding potential landscape. We note that we repeated all the calculations for 5 different random potential landscape (for each QD size) and observed similar behaviors. In the TB results, in addition to valance states accumulated around peaks and conduction states around troughs as expected, we also observe abnormal valance states
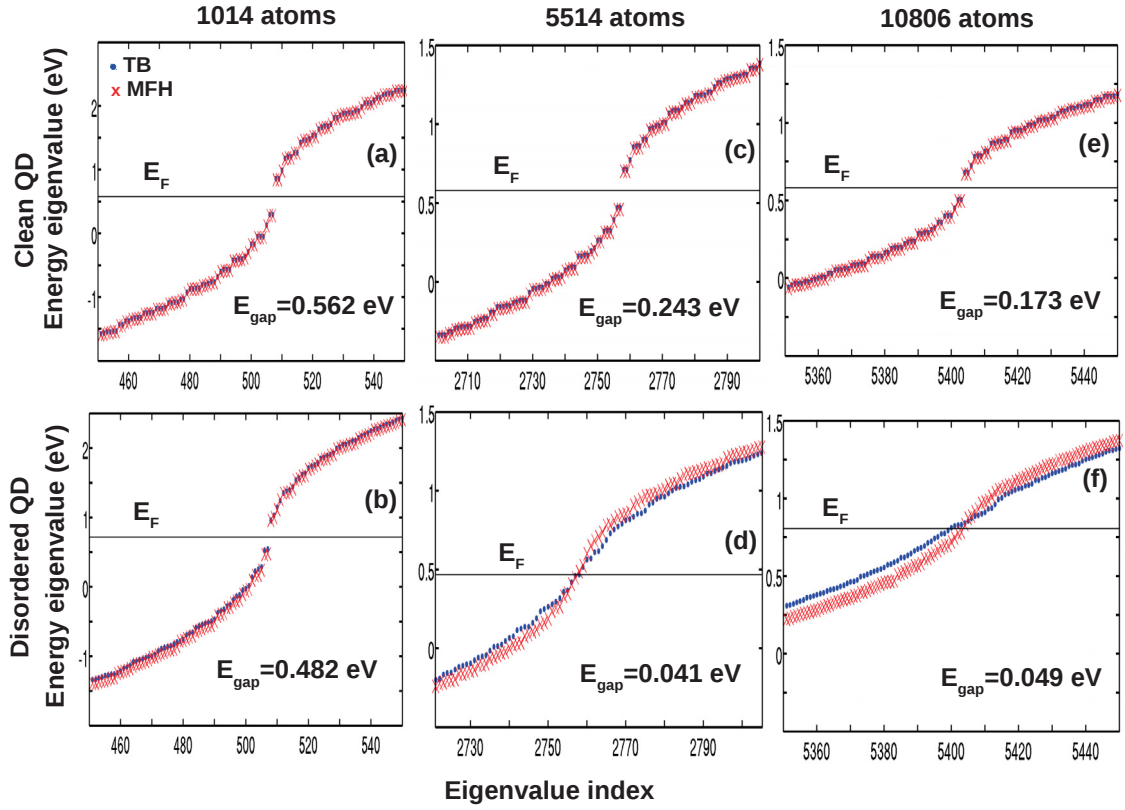
Figure 4.12. Energy spectra for clean (upper panels) and disordered (lower panels) GQDs obtained by TB and MFH. Fermi energy level E_F is determined to be in the mid-point between valance and conduction band.

around troughs and conduction states around peaks. In fact, those abnormal states are an artifact of the TB method which is better suited for systems with homogeneous and neutral charge distributions. In our system, the charge density fluctuates strongly due to random disorder and the energy gap between valence and conduction states is not large enough to protect hole states from mixing with electron states. Thus, a mean-field correction to the TB method must be included

In Figure 4.6 and 4.7, we investigate electronic densities corresponding to 20 lowest conduction and 20 highest valence states obtained from MFH for the GQDs having similar disorder structures that we studied for TB model. When electron-electron interactions are included through MFH calculations, electronic density fluctuations are reduced in almost all area of the QD and the abnormal localized states are washed out (Altıntaş *et al.*, 2017) (see Figure 4.8). Similar behavior was also observed in graphene
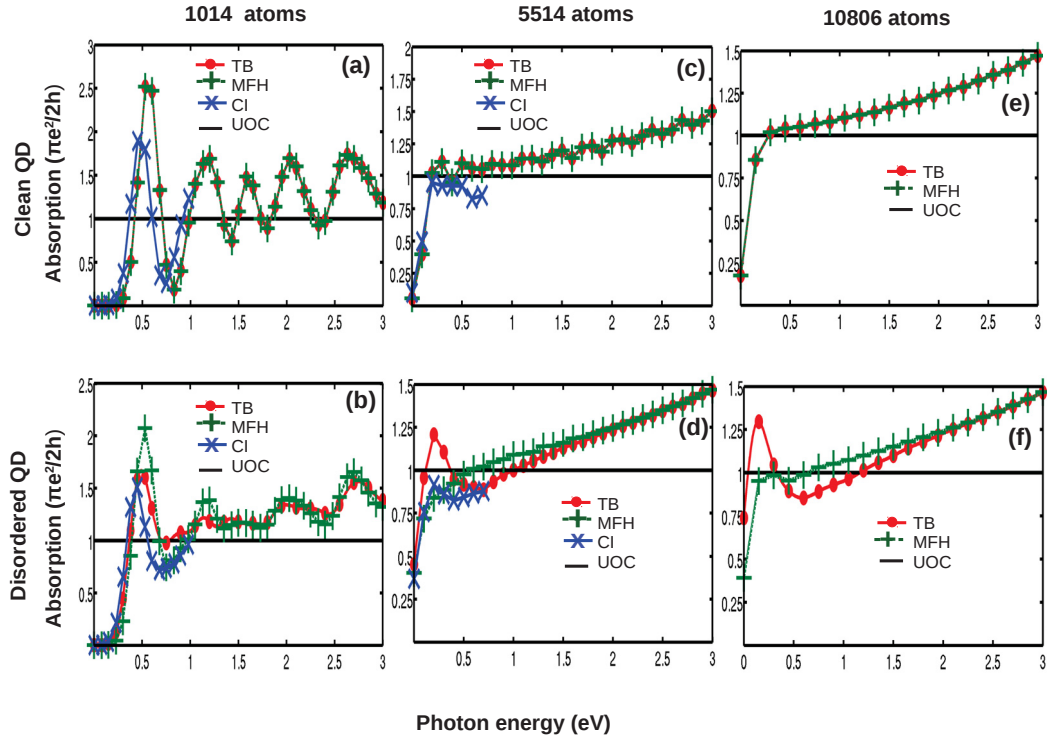
Figure 4.13. Absorption Spectrum for clean (upper panels) and disordered (lower panels) GQDs obtained by TB, MFH and excitonic effect with CI model. UOC is indicated by black line. In clean GQDs, as the size of GQDs increase, a plateau develops near the UOC at low energies, before a sudden drop occurs due to finite size effects.

nanoribbons (Özdemir *et al.*, 2016). The rearrangement of electron-hole puddles through electronic interactions has an important effect on optical properties. Additionally, we don't see dramatic change in effects of interaction strength on distribution of electronic states in QDs for $\kappa = 3$ and $\kappa = 6$ as can be seen in Figure 4.6 and 4.7.

In order to investigate the effect of configuration interactions, in Figure 4.9 we plot the electron and hole densities weighted with absorption probabilities in the energy range between 0 eV and 0.3 eV for the 5514 atom GQD, obtained from TB , MFH and CI calculations. As discussed earlier, mean-field interactions smooth the puddles so that excitonic hole states are now localized only on peaks, and the electron states are localized on troughs as seen in Figure 4.9. On the other hand, the correlations have a less dramatic effect on the density distribution, but the electron states are now slightly more localized

40
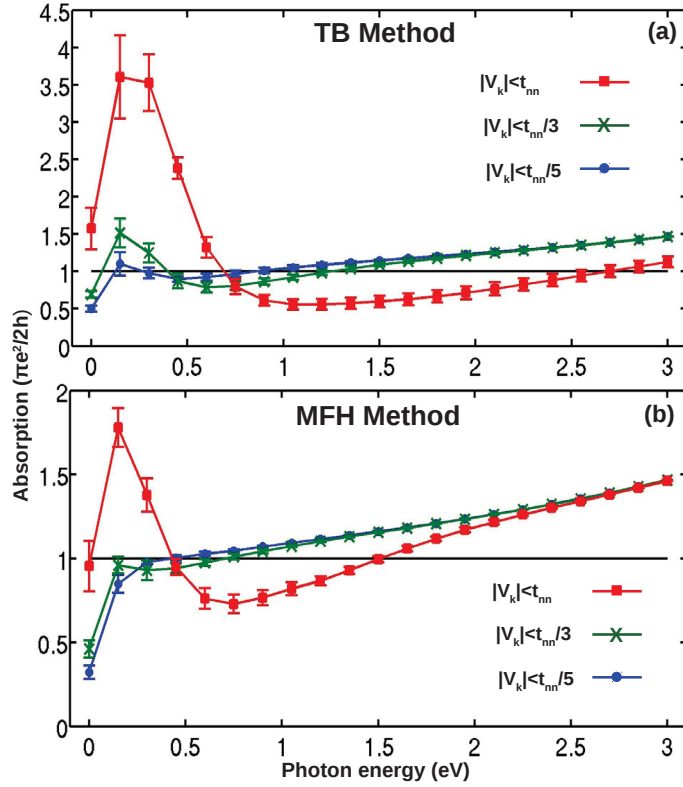
Figure 4.14. Average absorption spectrum curves (each curve corresponds to average of 5 different configurations) for three different impurity potential peaks obtained by TB (upper panel) and MFH (lower panel) method with estimated error bars for the structure containing 10806 atoms. UOC is indicated by black line.

on a potential trough that is closer to the hole puddle (Figures 4.9 f and g). Indeed, the electron-hole attraction is favoured in the CI calculations minimizing the average distance between the electron and the hole, thus increasing the electric dipole strength and the absorption at lower energies (see Figure 4.13).

Energy spectra of clean (upper panels) and disordered (lower panels) GQDs having width size of 5 nm (1014 atoms), 13 nm (5514 atoms) and 18 nm (10806 atoms) obtained by TB and MFH model are shown in Figure 4.12. For each case, the energy gap E_{gap} between between lowest unoccupied conduction state and highest occupied valence state obtained from the MFH calculations is indicated as well. As expected, E_{gap} decreases more rapidly as a function of size when impurities are present. More interestingly however, for larger size disordered GQDs the difference between TB and MFH spectra

become pronounced indicating that when charge inhomogeneities (due to electron-puddle formation) are present it is important to include the effects of electronic interactions. Similar behavior was also observed for other random potential configurations that we have tested.

Figure 4.13 shows absorption spectra curves corresponding to the GQDs considered in Figure 4.12 for energies up to 3 eV. The absorption spectra are calculated using equations (4) and (5) with a Gaussian broadening (0.1 eV) of delta functions in order to obtain continuous curves, within TB (line doted curve, red color online), MFH (line plus signed curve, green color online) and CI (line cross signed curve, blue color online) approaches. The UOC is indicated by black line as a reference. For clean GQDs, there is no noticeable difference between the TB and MFH results, consistent with the results in Figure 4.12. We note that, as the system size increases, absorption curves approach the UOC value at low energies, until a sudden drop occurs due to finite size effects. For the CI calculations, 100 highest valence and 100 lowest conduction states were included to form a many-body basis set of 10000 excitonic states, to ensure convergence for energies up to 0.75 eV. As seen from Fig.4a and Fig.4b, the main effect of excitonic correlations is to red shift the absorption spectrum (Ozfidan *et al.*, 2016) followed by a slight decrease in the peak value. For GQDs larger than 13 nm (5514 atoms), it was not possible to calculate the CI absorption spectrum due to computational limits.

When disorder is present, we observe a dramatic difference between the TB and MFH results, shown in Figure 4.13 b,d,f. This is mainly due to the redistribution of electron-hole puddles discussed in Figure 4.8. For the medium and large size GQDs without electronic interactions, in TB calculations, both electrons and hole puddles may be present at the same locations, giving rise to stronger electric dipole coupling, thus higher absorption values in average at lower energies. Note that the situation is different for the GQD with 1014 atoms, since the puddle formation is much less well defined as the size of the QD is reduced, and the specific form of the disorder landscape has a bigger role. For medium size GQD, however, a disorder peak reappears at low energies when excitonic correlations are taken into account. This is due to the fact that excitonic interactions rearranges the electron and hole distributions within the disorder troughs and peaks, as we discuss in Figure 4.9. We note that the CI results obtained for the disordered GQD with 5514 atoms is consistent with the experimental results for graphene sheet (Mak *et al.*, 2008, 2011; Lee *et al.*, 2011).

To see effects of various impurity potential strength on absorption spectrum obtained by TB and MFH methods (see Figure 4.14 a-b), we compare spectrum curves

(each spectrum curve corresponds to average of five different samples shown with error-bars having width of twice the standard error) containing three different impurity potential strength peak values of t_{nn} (line squared curve, red color online), $t_{nn}/3$ (line cross signed curve, green color online) and $t_{nn}/5$ (line doted curve, blue color online), for the largest QD structure. For the strong impurity potential strength ($|V_k| < t_{nn}$), both TB and MFH results deviate significantly from UOC line indicating that the system is in a strongly non-perturbative regime, and meanfield electron interactions are not sufficiently strong to wash out the impurity peak. However, for medium potential strength ($|V_k| < t_{nn}/3$) and small potential strength $|V_k| < t_{nn}/5$, the low energy absorption obtained from MFH remains always below the UOC line within our error bars.

4.4. Conclusion

In conclusion, we have investigated electronic and optical properties of three different sizes of clean and disordered hexagonal armchair-edged GQDs by applying tight-binding, mean-field Hubbard and configuration interaction models. Long-ranged disorder give rise to formation of electron-hole puddles, which are, however poorly described by the tight-binding model alone. Electronic interactions in the mean-field picture reorganize the electron-hole puddles, strongly affecting the dipole moments between the low-energy states in the electronic spectrum. Hence, inclusion of electronic interactions are found to be important in order to correctly describe the optical properties. As the system size is increased to 18 nm, absorption spectra obtained from configuration interaction method approach the experimental results leading to observation of universal optical conductivity (Mak *et al.*, 2008, 2011; Lee *et al.*, 2011).

CHAPTER 5

MAGNETIC PROPERTIES

In this chapter, we focus on magnetic properties of GQDs which has short-range disorders such as hydrogenation or vacancies. We explain magnetization caused by defects and try to understand antiferromagnetic and ferromagnetic behavior of GQDs.

5.1. Magnetization

Graphene nanostructures can acquire ferromagnetic or anti-ferromagnetic behavior if they have populated unbalanced or balanced sublattice sites at the edges (Güçlü *et al.*, 2011; Voznyy *et al.*, 2011; Carvalho *et al.*, 2014; Özdemir *et al.*, 2016; Güçlü *et al.*, 2016; Friedman *et al.*, 2017) in the structure as can be seen in Figure 5.1 (Magda *et al.*, 2014). On the other hand, introducing adatoms(Balog, 2009; Šljivančanin *et al.*, 2009; Elias *et al.*, 2009; Balakrishnan *et al.*, 2013; González-Herrero *et al.*, 2016; McCreary *et al.*, 2012) or vacancies(Mao *et al.*, 2016; Ugeda *et al.*, 2010; Nair *et al.*, 2012; Zhang *et al.*, 2016; Nair *et al.*, 2013) can also significantly affect magnetic behavior of graphene nanostructures. For example, local or global magnetic moment induction which led to spin split state at the Fermi energy were observed in several experimental works by introducing hydrogen adatoms on graphene (Elias *et al.*, 2009; González-Herrero *et al.*, 2016). Additionally, local magnetism due to vacancies created by irradiation of graphene samples were also detected(Ugeda *et al.*, 2010; Nair *et al.*, 2013).

5.2. Short-Range Disorders

There have been many theoretical attempts to explain induction of magnetism brought about by adatom or vacancy related disorders in graphene structures (Sevinçli *et al.*, 2008; Yazyev and Helm, 2007; Palacios *et al.*, 2008; Uchoa *et al.*, 2008; Peres *et al.*, 2006; Boukhvalov *et al.*, 2008; Soriano *et al.*, 2010; Liang *et al.*, 2011; Soriano *et al.*, 2011; Leconte *et al.*, 2011; Güçlü and Bulut, 2015; Safari *et al.*, 2017). For instance, ferromagnetic or antiferromagnetic behavior of quasilocalized states can be induced by
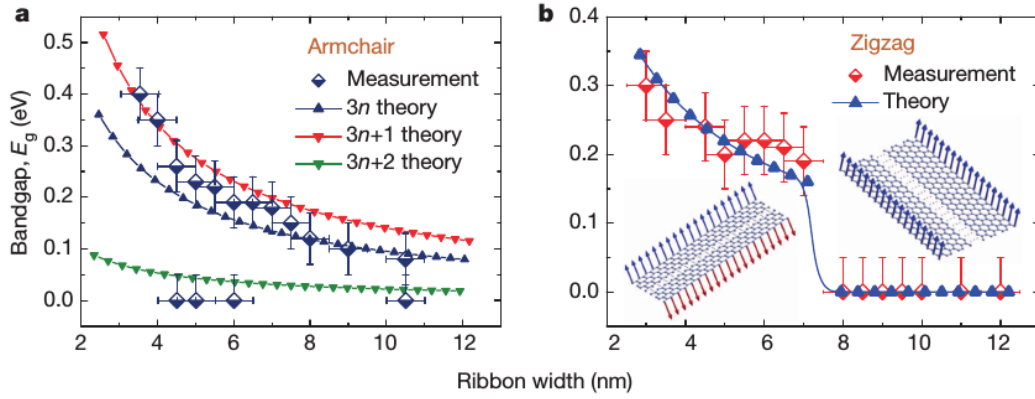
Figure 5.1. Room temperature magnetization in graphene ribbons. a) shows band gap of armchair graphene ribbon and b) shows band gap and spin orientation of zigzag ribbon. (Source: Magda *et al.*, 2014).

introducing two atomic defects on the same or opposite sublattices of the honeycomb lattice. Furthermore, it was found that vacancy related sublattice imbalance which leads to total spin $S \neq 0$ can induce global magnetism predicted by Lieb and sublattice balance which leads to total spin $S = 0$ can induce local magnetism by using mean-field Hubbard model for graphene ribbons (Lieb, 2002; Palacios *et al.*, 2008)

In order to account for short-range disorder effects (which may be due to vacancies or hydrogen adatoms, see Fig. 5.2), we simply remove corresponding p_z orbital sites. This model assumes that sp2 hybridization of atoms neighboring the defect is not distorted.

5.3. Results and Discussion

A critical step in the numerical calculations is the initial guess state used for the self-consistent diagonalization of the MFH Hamiltonian, as there is a high risk of getting stuck in a local energy minimum for systems with several thousands of atoms. Local version of Lieb's theorem provides a convenient way to generate the initial state. According to Lieb's theorem (Lieb, 2002), if there is an overall imbalance between the number of A and B sublattice atoms, a finite magnetic moment $(N_A - N_B)/2$ arises at zero temperature. Locally, such imbalance occurs in the vicinity of atomic defects. Therefore, in our initial density matrices, we assume a surplus of spin up (down) density around type-A (B)
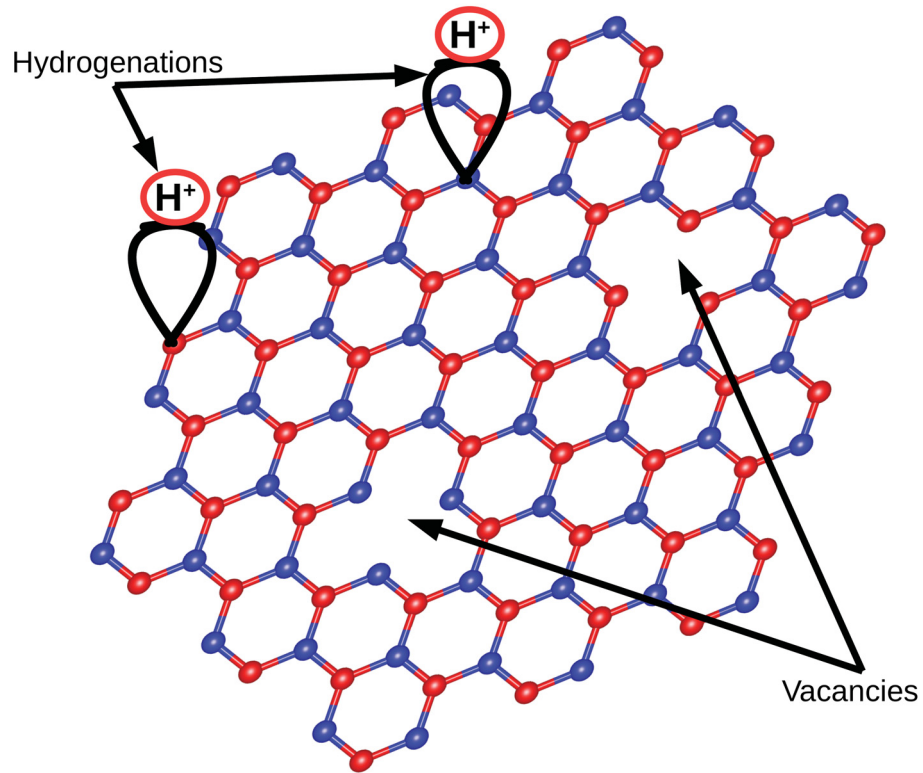
Figure 5.2. Hydrogenation or vacancies as a short-range disorder model on a hexagonal armchair edged GQD

vacancies, leading to our lowest energy solution.

Figure 5.3 shows the spin resolved DOS for defects concentrations of 1% (upper panels), 2% (middle panels) and 5% (lower panels). On the left panels, we consider equal number of randomly distributed defects on A and B sublattices (50-50 %). Even though the total spin of such a system is zero as predicted by Lieb's theorem (Lieb, 2002), a slight asymmetry can be observed between spin up and down impurity peaks in the vicinity of Fermi level, due to broken sublattice symmetry. On the other extreme, if all defects are placed on sublattice A (right panel), total spin is equal to half of the total number of defects, and a clear spin splitting is observed in DOS, a signature of ferromagnetic coupling. As expected, as the concentration of defects is increased from 1% to 5%, impurity peaks become more pronounced.

In Fig. 5.4, we plot the spin densities $n_{i\uparrow} - n_{i\downarrow}$ (upper panels) and defect positions (lower panel) for different concentration and sublattice distributions. When the system is antiferromagnetic (for even number of sublattice A and B defects), statistical distribution
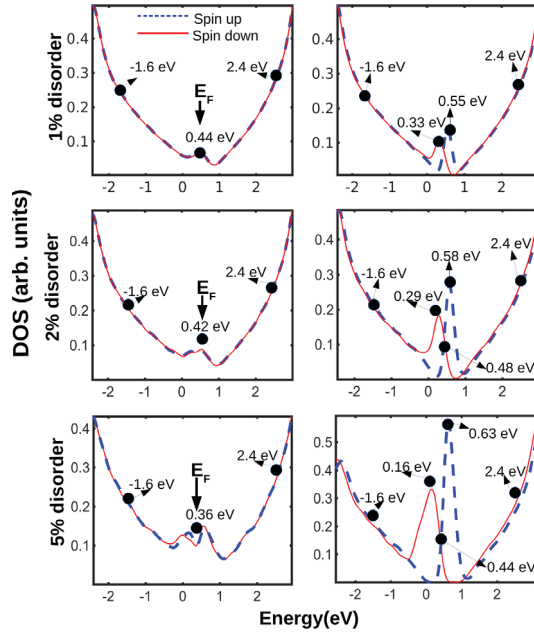
Figure 5.3. (Color online) Density of states for spin down (red solid line) and spin up (dashed blue line). 1% (upper panels), 2% (middle panels) and 5% (lower panels) disorders are randomly distributed among each sublattice as 50% (50%) (left panels) and 100% (0%) (right panels) for sub lattice A (B). Big black dots show incoming electrons with specific energy and Fermi energy indicated by arrow. As the amount of impurity increases, a peak in DOS near the Fermi level (left panels) is observed and DOS splitting of spin up and down states occurred (right panels). One configuration is shown for each disorder amount since other 19 configurations show similar behaviors.

of defects gives rise to formation of magnetic puddles with opposite signs (shown in red and blue colors online). On the other hand, a formation of electron-hole puddles due to atomic defects was previously observed in a TB study of LDOS in large graphene ribbon structures (Schubert and Fehske, 2012). It was found that as the defect concentration increases from 0.1% to 1%, the spatial extent of electronic puddles is reduced below 1 nm from 5-10 nm. Although the scale of our magnetic puddle size is consistent with the findings of Ref. (Schubert and Fehske, 2012) for 1% impurity concentration, we do not observe clear change in puddle size as we increase the defect concentrations. The formation of magnetic puddles observed in our calculations is presumably mainly due to the statistical distribution of defect-induced spins rather than more subtle quantum interference or interaction effects. We observed similar magnetic puddle-like structures
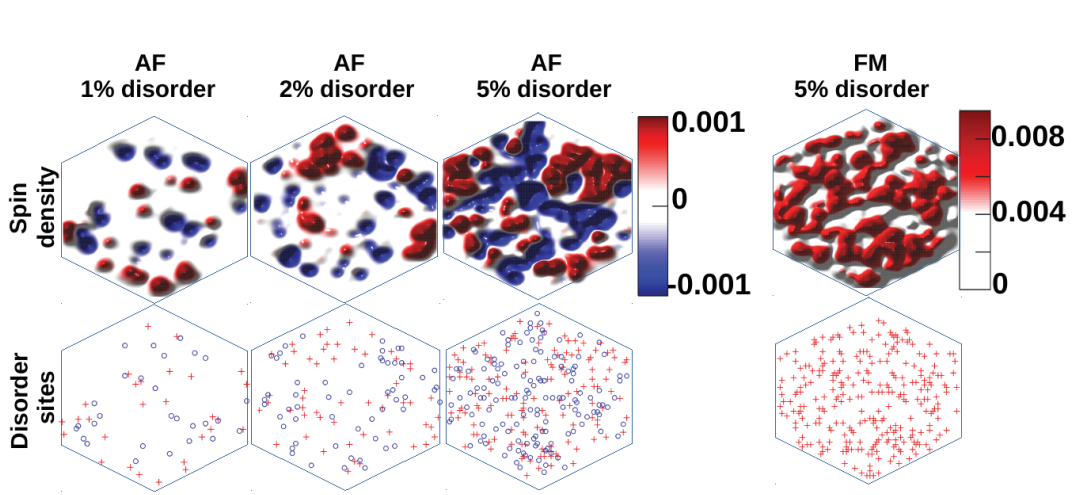
Figure 5.4. Magnetic puddle formation in anti-ferromagnetic (AF) and ferromagnetic (FM) GQDs. Disorders are randomly distributed among each sublattice as 50% (50%) (first three panels) and 100% (0%) (last panel) for sub lattice A (B) . Upper panels show spin density profile and red (blue) regions represent either spin up or down electrons. The corresponding disorder sites are pictured by lower panels and blue circles (red crosses) represent corresponding disorder sites.

for other 19 different disorder configurations.

Finally, we try to observe staggered magnetization per impurity (see Fig. 5.5) and we will discuss interplay between magnetization and localization in the chapter 6. A useful quantity that describes the magnetic properties is staggered magnetization defined as :

$$M^{stag} = \sum_i (-1)^x (n_{i\uparrow} - n_{i\downarrow})/2 \qquad (5.1)$$

where x is even for A and odd for B sublattice sites. In Fig. 8, we plot the staggered magnetization per impurity, M^{stag}/N_{imp} as a function of defects concentration of 0.3 - 5 % for the AFM and FM configurations, averaged over 20 disorder samples. For each case, the localization length λ is also shown. Several interesting observations can be made from Figure 5.5. First, magnetization of AFM configurations (same-sublattice defect distribution) is considerably lower than the FM configurations (even distribution). This reflects the suppression of antiferromagnetic coupling whenever two impurities are close to each other (Leconte *et al.*, 2011), as discussed above (see Figure5.4). Also, the AFM error bars are much larger than the FM error bars, showing that the AFM magnetization is more sen-
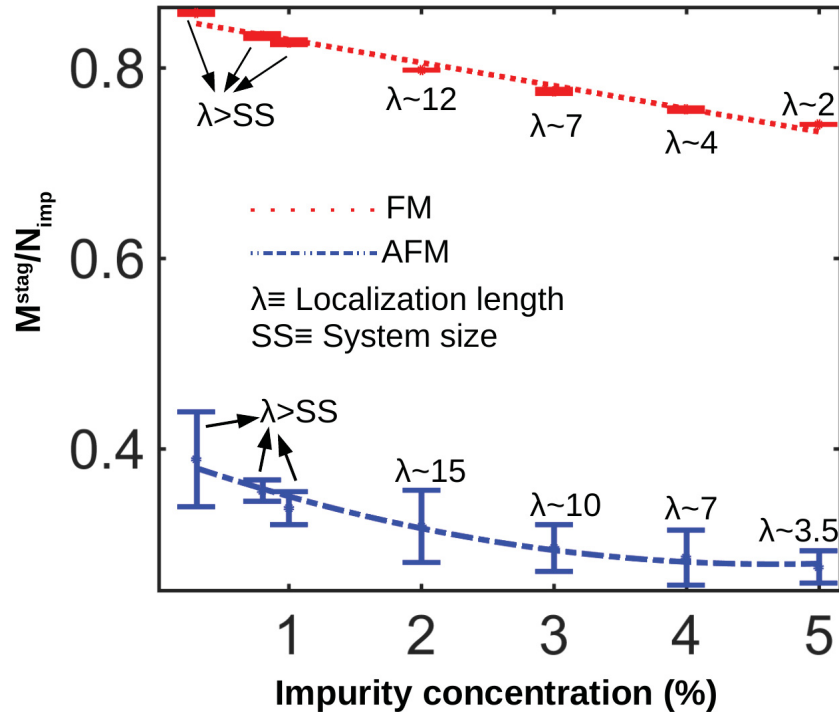
Figure 5.5. Staggered magnetization per impurity vs total impurity percent. Staggered magnetization slightly increases with localization length both for evenly (50-50%, dashed blue curve) and unevenly (100-0%, dotted red curve) and randomly distributed defects among each sublattice. Each data of impurity represents average of 20 different configurations containing 5514 atoms with corresponding error bars.

sitive to the specific distribution of the defect sites. Indeed, for some of the samples, large regions dominated by same-sublattice type defects may be present, causing weaker AFM suppression. However the net AFM magnetization is never completely suppressed.

5.4. Conclusions

We observed magnetic puddle-like formations induced by random distribution of defects with concentrations between 1% and 5%.We showed that, if the disorder sites are distributed on a same sublattice of the honey-comb lattice, significantly enhanced magnetism occurs compared to the evenly distributed antiferromagnetic case.

CHAPTER 6

ANDERSON LOCALIZATION

In this chapter, we try to figure out the effects of randomly created disorders on the localization of electronic waves. We show that randomly created short-range disorders leads to Anderson-type localization of electronic waves in GQDs.

6.1. Propagation of electronic waves
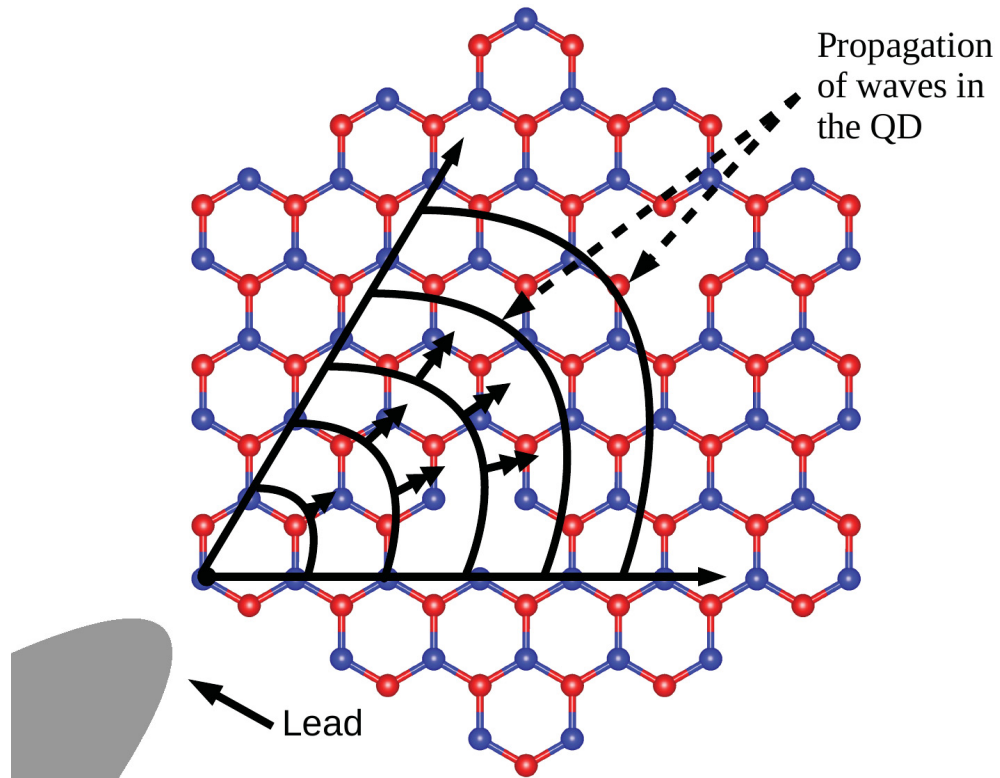
Figure 6.1. Cartoon of propagation of waves corresponding to an electron injected from one corner of the QD.

Impurity may halt transport and waves become localized when disorders are distributed randomly with enough concentrations as claimed by Anderson in 1958 (Ander-
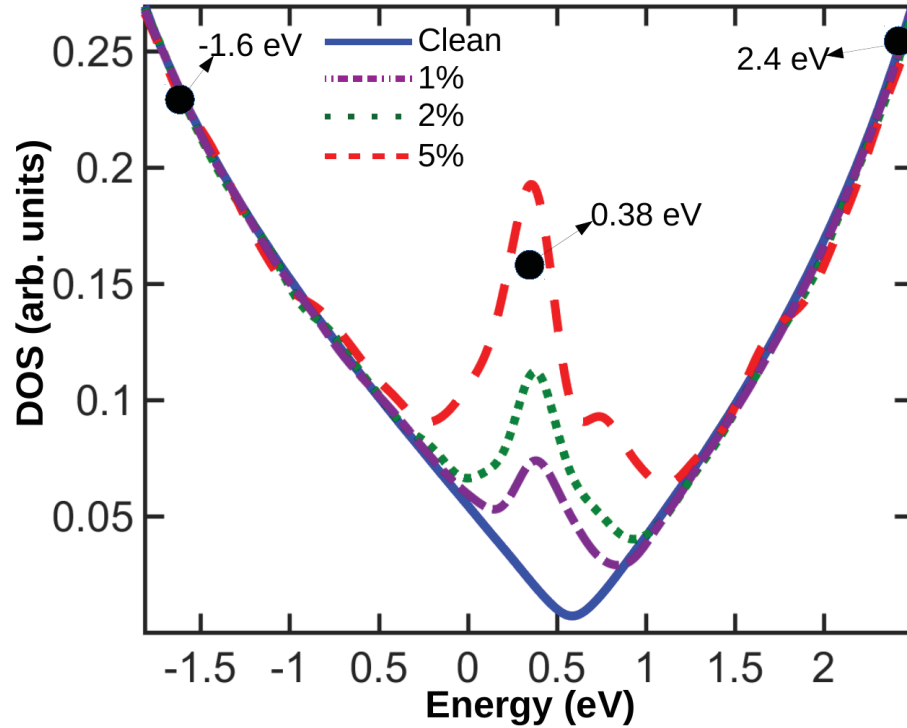
Figure 6.2. Density of states obtained by TB model for clean (solid blue line),%1 (dotted and dashed purple line), %2 (dotted green line) and %5 (dashed red line) disordered dot. Big black dots show incoming electrons with specific energy. One configuration is shown for each percent of disorder since other 19 configurations show similar behavior. As the amount of impurity increases, a peak in DOS near the Fermi level ($E \sim 0.38$ eV) is observed, as expected.

son, 1958). This type of localization of waves are so called Anderson localization since the time it has been predicted. A conductive material may become insulator when it has randomly distributed disorders on it. For example, a dramatic increase in resistivity of graphene, metal-to-insulator (localization) behavior were observed in several experimental works by randomly introducing hydrogen adatoms on graphene nanostructures (Ponomarenko *et al.*, 2011; Elias *et al.*, 2009; Bostwick *et al.*, 2009). In several studies, it has been attempted to explain induction of metal-to-insulator transition (localization) theoretically (Soriano *et al.*, 2010; Liang *et al.*, 2011; Khajetoorians *et al.*, 2013; Schubert *et al.*, 2009; González-Santander *et al.*, 2013; Schubert and Fehske, 2012; Leconte *et al.*, 2011; Cresti *et al.*, 2013). For instance, Schubert *et al.* used a tight-binding (TB) model ignoring magnetic effects to show that low concentrations of randomly distributed
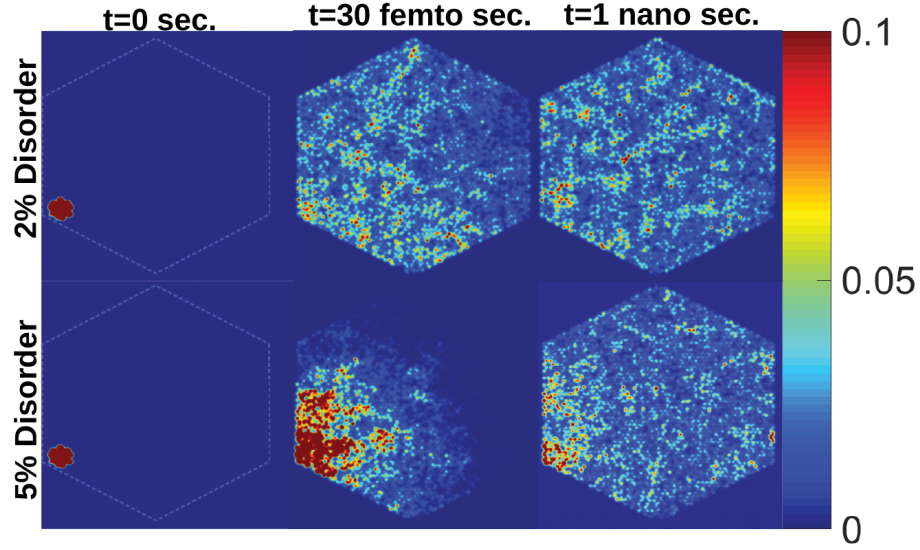
Figure 6.3. Time evolution of local particle density obtained by TB model for disordered GQD. Each column panels show the snapshot of propagation of waves at the specific time. From left to right, time is taken to be t=0 sec., t=30 femto sec. and t=1 nano sec. and from top to bottom, disorders are distributed as 2% and 5%, respectively. Color bar shows relative density of waves. Relative density increases from blue to red color.

hydrogen adatoms lead to metal-to-insulator transition in graphene, although alongside formation of electron-hole puddles that tend to suppress Anderson localization (Schubert *et al.*, 2009).

Our approach is to obtain time-dependent wave functions by assuming an initial wave packet of the electron injected through one corner of the hexagonal QD (See Figure 6.1) as $\psi(t=0)$ with average energy $\langle E_i \rangle$ of width $\delta E_i \sim t_{nn}/2$, the evolution is given by $\Psi(t) = \sum_n \langle \psi_{n\sigma} | \psi(t=0) \rangle e^{-iE_n t/\hbar} \psi_{n\sigma}(x_i)$. When the time scale is sufficiently large, $t \gg t_0 = t_{nn}/\hbar$, (where $t_0 \sim$ femto second) the system reaches a quasi-stationary state from which it is possible to deduce the localization propertiesSchubert *et al.* (2009).

6.2. Results and Discussions

In this part, we focus on defect concentrations of 1%, 2% and 5%, randomly distributed on clean hexagonal armchair GQD's containing 5514, 10806 and 21426 ($\sim$13, 18 and 25 nm QD size, respectively) atoms. Figure 6.2 shows the density of states (DOS)
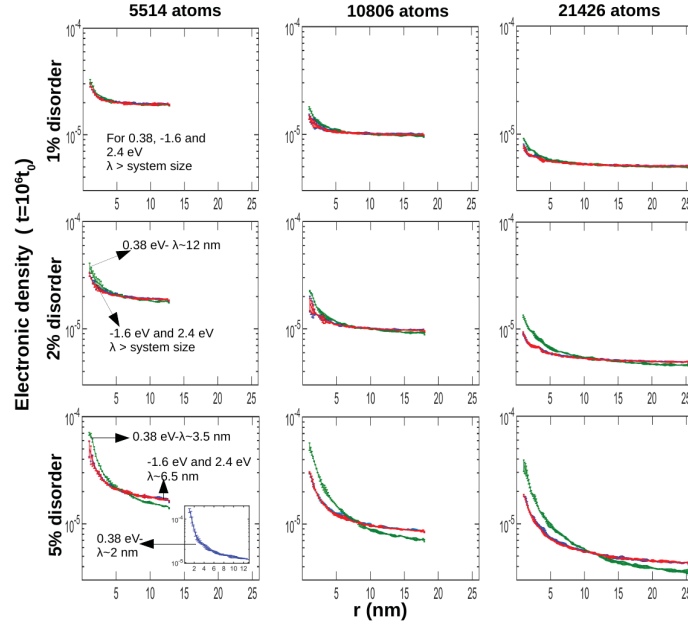
Figure 6.4. Localization of electronic states for 5514, 10806 and 21426 atoms obtained by TB method. Each column corresponds to different sizes of GQDs and row corresponds to 1%, 2% and 5% percent of randomly created disorder (evenly distributed between sublattice A and B) in GQDs. Axis-y represents electronic wave density of electrons having specific energies and x-axis represents propagation of wave along the length which starts from the contacted edge of the QD to the opposite edge (see Figure 6.1). Each curve represents average of 20 different configurations with corresponding error bars. Localization lengths of GQD containing 5514 atoms are only shown since localization lengths of bigger QDs have similar value for the same rows.

of a 5514 atoms QD for defect-free and disordered cases obtained from TB calculations. Black dots represent energies of interest at which an electron will be injected from the lead. In particular, as the defect concentration increases, a peak in DOS near the Fermi level ($E \sim 0.38 eV$) is observed, as expected. Corresponding time evolution density plots for a $E = 0.38 eV$ wave packet are shown in Figure 6.3, at $t = 0$, $t/t_0 = 30$ and $t/t_0 = 10^6$ (from left to right), for defects concentrations of 2% (upper panels) and 5% (lower panels). Initially, at $t = 0$, we assume that the injected wave packet occupies a small, defect-free region of the QD. As t is increased, the density propagates slower for higher defect concentrations, before reaching a quasi-stationary state above $t/t_0 = 10^4$. At higher time scales, $t/t_0 = 10^6$ (1 ns), the wave packet is still localized around the
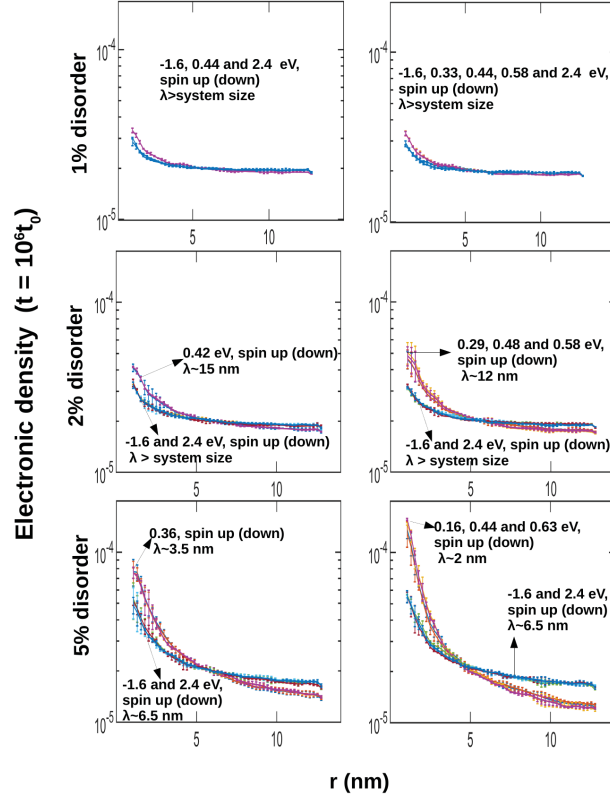
Figure 6.5. Localized particle density for spin up and down electrons. 1% (upper panels), 2% (middle panels) and 5% (lower panels) disorders are randomly distributed among each sublattice as 50% (50%) (left panels) and 100% (0%) (right panels) for sub lattice A (B). Spin up and down electrons show similar localization behavior. Each curve represents average of 20 different configurations with corresponding error bars.

corner of the QD, especially visible at the higher defect concentration.

In order to investigate the localization more systematically including size dependence, in Figure 6.4 we plot the injected electron's probability density as a function of distance to the lead corner, integrated over an angle of $\pi/3$ (see Figure 6.1), and averaged over 20 randomly generated defect configurations (evenly distributed between sublattice A (50%) and B (50%) for the main frames but unevenly as A (100%) and B (0%) for the inset figure), obtained from TB calculations. Moreover, time averages over 36 samples between $t/t_0 = 5 \times 10^5$ and 4×10^6 were performed. Here, each column corresponds to a different size GQD while each row corresponds to a different defect concentration. Localization lengths denoted by λ were estimated for different injected electron's energies (one near the Fermi level, other two in deep conduction and valence bands), by logarithmic

curve fitting. At 1% defect concentration, size effects dominate the densities. Estimated localization length is larger than the system size even for the largest QD (25 nm in width size) and the energy dependence is weak. As the defect concentration is increased to 2%, we find $\lambda \sim 12$ nm for 0.38 eV (Fermi level energy) for all QD sizes. At -1.6 and 2.4 eV, λ exceeds the system size. Finally, increasing defect concentration to 5% decreases localization length to $\lambda \sim 3.5$ nm for at 0.38 eV for all QD sizes. Additionally, we start to observe localization ($\lambda \sim 6.5$ nm) for the energies -1.6 and 2.4 eV. The calculated localization lengths here are consistent with the TB results by Schubert *et al.* (Schubert *et al.*, 2009) obtained for ribbon geometries. Furthermore, localization is more enhanced when disorders are distributed unevenly between sublattice A (100%) and B (0%) consistent with Cresti Cresti *et al.* (2013).

In the following, we focus on meanfield Hubbard results for the 13 nm wide QD to investigate the interplay between localization and magnetic properties. Figure 5.3 shows the spin resolved DOS for defects concentrations of 1% (upper panels), 2% (middle panels) and 5% (lower panels). On the left panels, we consider equal number of randomly distributed defects on A and B sublattices (50-50 %). A slight asymmetry can be observed between spin up and down impurity peaks in the vicinity of Fermi level, due to broken sublattice symmetry. On the other extreme, if all defects are placed on sublattice A (right panel), total spin is equal to half of the total number of defects, and a clear spin splitting is observed in DOS, a signature of ferromagnetic coupling. As expected, as the concentration of defects is increased from 1% to 5%, impurity peaks become more pronounced.

In order to study the interplay between localization and magnetic properties, in Figure 6.5 we plot the angle integrated electronic densities, similar to Figure 6.4, but obtained using spin-resolved MFH quasiparticle states. As before, the densities are averaged over 20 configurations and the plots include corresponding error bars. Upper, middle and lower panels correspond to 1%, 2% and 5% defect concentrations, respectively, while left and right panels correspond to evenly (50-50%) and unevenly (100-0%) distributed defects among the two sublattices. Although both spin up and down densities are plotted in each subfigure, to our surprise no noticeable difference was found between them, within the statistical error based on 20 randomly distributed configurations. For evenly distributed defects, the estimated localization lengths from MFH calculations are similar to those obtained from TB calculations of Figure 6.4. As can be seen in Figure 6.5, localization is not observed for 1% concentration and evenly (50-50%) and unevenly (100-0%) distributed defects do not change localization behavior. However, if the defect concentration increases and defects are distributed unevenly among the sublattices, localization

lengths in the vicinity of Fermi level decreases considerably from $\lambda \sim 15$ nm to $\lambda \sim 12$ nm for 2% concentration and from $\lambda \sim 3.5$ nm to $\lambda \sim 2$ nm for 5% concentration of defects. This is due to the fact that an even distribution of defects causes more impurity-level hybridization around the Fermi level compared to uneven distribution that gives rise to sharper and stronger peak in DOS as seen in Figure 6.5. Away from Fermi level, no significant sublattice effect is observed, as expected.

To observe interplay between localization and magnetization we we try to observe staggered magnetization per impurity (see Figure 5.5). One of the important observation is that the localization is consistently stronger for the FM configuration than for the AFM configurations. This results is consistent with the conductivity calculations based on tight-binding results of Cresti *et al.* (2013), where compensated distribution of defects in a graphene sheet leads to more localization than the same sublattice distribution. Finally, we see that as the defect concentration increases, the localization length decreases as expected, and the staggered magnetization per impurity slightly decreases. Net staggered magnetization of course increases with increasing number of defects.

6.3. Conclusions

To conclude, we studied localization induced by atomic defects, using tight-binding and meanfield Hubbard approaches, for medium sized hexagonal armchair graphene quantum dots. For QD sizes above 12 nm, defect concentrations of 2% is needed in order to observe localization effects. We show that localization length is not affected by magnetization if there is an even distribution of defects between the two sublattices of the honeycomb lattice. For an uneven distribution that heavily breaks the symmetry between the two sublattices, although no noticeable difference was found between the spin up and down states, their localization is found to be significantly enhanced as compared to evenly distributed defects.

CHAPTER 7

CONCLUSION

Detailed theoretical investigation of combined effects of long-range disorder and electron-electron interactions on the optical properties of graphene quantum dots has been carried out. We studied both electronic and optical properties of medium and large sized hexagonal armchair GQDs to understand the role of long-ranged disorder on the optical properties. Our main contribution involved inclusion of electron-electron interactions within meanfield and many-body configuration interaction approaches. We show that the electron-electron interactions play a significant role in redistributing electron-hole puddles, thus strongly affecting the optical properties. We also investigated the large size limit of the GQDs as compared to optical properties of bulk graphene and show that UOC can be observed in GQDs with a diameter of 18 nm.

On the other hand, we also tried to find out the role of atomic defects in both the localization of electronic states and the magnetic behavior at the nanoscale, we performed meanfield Hubbard (MFH) calculations for medium sized graphene quantum dots (GQD). More specifically, we focused on hexagonal shaped GQDs with armchair edges which are, unlike zigzag edges, free of magnetized edge effects. We showed that localization of electronic states can occur due to randomly created atomic defects, together with formation of magnetic puddles.

REFERENCES

Altıntaş, A., K. E. Çakmak, and A. D. Güçlü (2017). Effects of long-range disorder and electronic interactions on the optical properties of graphene quantum dots. *Physical Review B 95*(4), 045431.

Anderson, P. W. (1958). Absence of diffusion in certain random lattices. *Physical review 109*(5), 1492.

Balakrishnan, J., G. K. W. Koon, M. Jaiswal, A. C. Neto, and B. Özyilmaz (2013). Colossal enhancement of spin–orbit coupling in weakly hydrogenated graphene. *Nature Physics 9*(5), 284.

Balog, R. (2009). R. balog, b. jørgensen, j. wells, e. lægsgaard, p. hofmann, f. besenbacher, and l. hornekær, j. am. chem. soc. 131, 8744 (2009). *J. Am. Chem. Soc. 131*, 8744.

Basak, T., H. Chakraborty, and A. Shukla (2015). Theory of linear optical absorption in diamond-shaped graphene quantum dots. *Physical Review B 92*(20), 205404.

Berazin, F. (2012). *The method of second quantization*, Volume 24. Elsevier.

Berger, C., Z. Song, T. Li, X. Li, A. Y. Ogbazghi, R. Feng, Z. Dai, A. N. Marchenkov, E. H. Conrad, P. N. First, *et al.* (2004). Ultrathin epitaxial graphite: 2d electron gas properties and a route toward graphene-based nanoelectronics. *The Journal of Physical Chemistry B 108*(52), 19912–19916.

Berger, C., Z. Song, X. Li, X. Wu, N. Brown, C. Naud, D. Mayou, T. Li, J. Hass, A. N. Marchenkov, *et al.* (2006). Electronic confinement and coherence in patterned epitaxial graphene. *Science 312*(5777), 1191–1196.

Boehm, H., R. Setton, and E. Stumpp (1986). Nomenclature and terminology of graphite intercalation compounds.

Boehm, H.-P., A. Clauss, G. Fischer, and U. Hofmann (1962). Das adsorptionsverhalten sehr dünner kohlenstoff-folien. *Zeitschrift für anorganische und allgemeine*

Chemie 316(3-4), 119–127.

Bostwick, A., J. L. McChesney, K. V. Emtsev, T. Seyller, K. Horn, S. D. Kevan, and E. Rotenberg (2009). Quasiparticle transformation during a metal-insulator transition in graphene. *Physical review letters 103*(5), 056404.

Boukhvalov, D., M. Katsnelson, and A. Lichtenstein (2008). Hydrogen on graphene: Electronic structure, total energy, structural distortions and magnetism from first-principles calculations. *Physical Review B 77*(3), 035427.

Cai, J., C. A. Pignedoli, L. Talirz, P. Ruffieux, H. Sode, L. Liang, V. Meunier, R. Berger, R. Li, X. Feng, *et al.* (2014). Graphene nanoribbon heterojunctions. *Nature nanotechnology 9*(11), 896.

Cai, J., P. Ruffieux, R. Jaafar, M. Bieri, T. Braun, S. Blankenburg, M. Muoth, A. P. Seitsonen, M. Saleh, and X. Feng (2010). Atomically precise bottom-up fabrication of graphene nanoribbons. *Nature 466*(7305), 470.

Carvalho, A., J. Warnes, and C. Lewenkopf (2014). Edge magnetization and local density of states in chiral graphene nanoribbons. *Physical Review B 89*(24), 245444.

Chiu, K., M. R. Connolly, A. Cresti, J. Griffiths, G. Jones, and C. G. Smith (2015). Magnetic-field-induced charge redistribution in disordered graphene double quantum dots. *Physical Review B 92*(15), 155408.

Cresti, A., F. Ortmann, T. Louvet, D. Van Tuan, and S. Roche (2013). Broken symmetries, zero-energy modes, and quantum transport in disordered graphene: from supermetallic to insulating regimes. *Physical review letters 110*(19), 196601.

Dikin, D. A., S. Stankovich, E. J. Zimney, R. D. Piner, G. H. B. Dommett, G. Evmenenko, S. T. Nguyen, and R. S. Ruoff (2007). Preparation and characterization of graphene oxide paper. *Nature 448*(7152), 457.

Dirac, P. A. (1927). The quantum theory of the emission and absorption of radiation. *Proc. R. Soc. Lond. A 114*(767), 243–265.

Doi, M. (1976). Second quantization representation for classical many-particle system.

Journal of Physics A: Mathematical and General 9(9), 1465.

Dong, Y., J. Shao, C. Chen, H. Li, R. Wang, Y. Chi, X. Lin, and G. Chen (2012). Blue luminescent graphene quantum dots and graphene oxide prepared by tuning the carbonization degree of citric acid. *Carbon 50*(12), 4738–4743.

Dresselhaus, M. S. and G. Dresselhaus (2002). Intercalation compounds of graphite. *Advances in physics 51*(1), 1–186.

Elias, D. C., R. R. Nair, T. Mohiuddin, S. Morozov, P. Blake, M. Halsall, A. Ferrari, D. Boukhvalov, M. Katsnelson, A. Geim, *et al.* (2009). Control of graphene's properties by reversible hydrogenation: evidence for graphane. *Science 323*(5914), 610–613.

Emtsev, K. V., A. Bostwick, K. Horn, J. Jobst, G. L. Kellogg, L. Ley, J. L. McChesney, T. Ohta, S. A. Reshanov, J. Röhrl, *et al.* (2009). Towards wafer-size graphene layers by atmospheric pressure graphitization of silicon carbide. *Nature materials 8*(3), 203.

Fock, V. (1930). Näherungsmethode zur lösung des quantenmechanischen mehrkörper-problems. *Zeitschrift für Physik 61*(1-2), 126–148.

Friedman, J. S., A. Girdhar, R. M. Gelfand, G. Memik, H. Mohseni, A. Taflove, B. W. Wessels, J.-P. Leburton, and A. V. Sahakian (2017). Cascaded spintronic logic with low-dimensional carbon. *Nature communications 8*, 15635.

Gandhi, M. V. and B. D. Thompson (1992). *Smart Materials and Structures*. Springer.

Geim, A. K. and K. S. Novoselov (2007). The rise of graphene. *Nature materials 6*(3), 183.

Gerardot, B. D., D. Brunner, P. A. Dalgarno, P. Öhberg, S. Seidl, M. Kroner, K. Karrai, N. G. Stoltz, P. M. Petroff, and R. J. Warburton (2008). Optical pumping of a single hole spin in a quantum dot. *Nature 451*(7177), 441.

Gibertini, M., A. Tomadin, F. Guinea, M. I. Katsnelson, and M. Polini (2012). Electron-hole puddles in the absence of charged impurities. *Physical Review B 85*(20), 201405.

Gilkes, K. W. R., S. Prawer, K. W. Nugent, J. Robertson, H. S. Sands, Y. Lifshitz, and X. S (2000). Direct quantitative detection of the sp3 bonding in diamond-like carbon films using ultraviolet and visible raman spectroscopy. *Journal of Applied Physics 87*(10), 7283–7289.

Gilkes, K. W. R., H. S. Sands, D. N. Batchelder, J. Robertson, and W. I. Milne (1997). Direct observation of sp3 bonding in tetrahedral amorphous carbon using ultraviolet raman spectroscopy. *Applied physics letters 70*(15), 1980–1982.

Gomez De Arco, L., Y. Zhang, C. W. Schlenker, K. Ryu, M. E. Thompson, and C. Zhou (2010). Continuous, highly flexible, and transparent graphene films by chemical vapor deposition for organic photovoltaics. *ACS nano 4*(5), 2865–2873.

González-Herrero, H., J. M. Gómez-Rodríguez, P. Mallet, M. Moaied, J. J. Palacios, C. Salgado, M. M. Ugeda, J.-Y. Veuillen, F. Yndurain, and I. Brihuega (2016). Atomic-scale control of graphene magnetism by using hydrogen atoms. *Science 352*(6284), 437–441.

González-Santander, C., F. Domínguez-Adame, M. Hilke, and R. Römer (2013). Localisation and finite-size effects in graphene flakes. *EPL (Europhysics Letters) 104*(1), 17012.

Griffiths, D. J. (1962). *Introduction to electrodynamics*. Prentice Hall.

Güçlü, A., P. Potasz, and P. Hawrylak (2010). Excitonic absorption in gate-controlled graphene quantum dots. *Physical Review B 82*(15), 155445.

Güçlü, A., P. Potasz, and P. Hawrylak (2011). Electric-field controlled spin in bilayer triangular graphene quantum dots. *Physical Review B 84*(3), 035425.

Güçlü, A. D. and N. Bulut (2015). Spin-spin correlations of magnetic adatoms on graphene. *Physical Review B 91*(12), 125403.

Güçlü, A. D., P. Potasz, M. Korkusinski, and P. Hawrylak (2016). *Graphene quantum dots*. Springer.

Güçlü, A. D., P. Potasz, O. Voznyy, M. Korkusinski, and P. Hawrylak (2009). Magnetism

and correlations in fractionally filled degenerate shells of graphene quantum dots. *Physical review letters 103*(24), 246805.

Hartree, D. R. (1928). The wave mechanics of an atom with a non-coulomb central field. part i. theory and methods. In *Mathematical Proceedings of the Cambridge Philosophical Society*, Volume 24, pp. 89–110. Cambridge University Press.

Hass, J., W. De Heer, and E. Conrad (2008). The growth and morphology of epitaxial multilayer graphene. *Journal of Physics: Condensed Matter 20*(32), 323202.

Jackson, J. D. (1975). *Electrodynamics*. Wiley Online Library.

Jang, C., S. Adam, J.-H. Chen, E. Williams, S. D. Sarma, and M. Fuhrer (2008). Tuning the effective fine structure constant in graphene: Opposing effects of dielectric screening on short-and long-range potential scattering. *Physical review letters 101*(14), 146805.

Jin, C., H. Lan, L. Peng, K. Suenaga, and S. Iijima (2009). Deriving carbon atomic chains from graphene. *Physical review letters 102*(20), 205501.

Johansson, A.-S., J. Lu, and J.-O. Carlsson (1994). Tem investigation of cvd graphite on nickel. *Thin Solid Films 252*(1), 19–25.

Khajetoorians, A. A., B. Baxevanis, C. Hübner, T. Schlenk, S. Krause, T. O. Wehling, S. Lounis, A. Lichtenstein, D. Pfannkuche, J. Wiebe, *et al.* (2013). Current-driven spin dynamics of artificially constructed quantum magnets. *Science 339*(6115), 55–59.

Kusdemir, E., D. Özkendir, V. Fırat, C. Çelebi, *et al.* (2015). Epitaxial graphene contact electrode for silicon carbide based ultraviolet photodetector. *Journal of Physics D: Applied Physics 48*(9), 095104.

Kuzmenko, A., E. Van Heumen, F. Carbone, and D. Van Der Marel (2008). Universal optical conductance of graphite. *Physical review letters 100*(11), 117401.

Leconte, N., D. Soriano, S. Roche, P. Ordejon, J.-C. Charlier, and J. J. Palacios (2011). Magnetism-dependent transport phenomena in hydrogenated graphene: From spin-

splitting to localization effects. *ACS nano 5*(5), 3987–3992.

Lee, C., J. Y. Kim, S. Bae, K. S. Kim, B. H. Hong, and E. Choi (2011). Optical response of large scale single layer graphene. *Applied Physics Letters 98*(7), 071905.

Lee, C., X. Wei, J. W. Kysar, and J. Hone (2008). Measurement of the elastic properties and intrinsic strength of monolayer graphene. *science 321*(5887), 385–388.

Li, X., C. W. Magnuson, A. Venugopal, R. M. Tromp, J. B. Hannon, E. M. Vogel, L. Colombo, and R. S. Ruoff (2011). Large-area graphene single crystals grown by low-pressure chemical vapor deposition of methane on copper. *Journal of the American Chemical Society 133*(9), 2816–2819.

Li, X., X. Wang, L. Zhang, S. Lee, and H. Dai (2008). Chemically derived, ultrasmooth graphene nanoribbon semiconductors. *science 319*(5867), 1229–1232.

Li, Y., H. Shu, S. Wang, and J. Wang (2015). Electronic and optical properties of graphene quantum dots: The role of many-body effects. *The Journal of Physical Chemistry C 119*(9), 4983–4989.

Liang, Q., Y. Song, A. Yang, and J. Dong (2011). Wave packet dynamics in hydrogenated graphene at low hydrogen coverages. *Journal of Physics: Condensed Matter 23*(34), 345502.

Liao, L., Y.-C. Lin, M. Bao, R. Cheng, J. Bai, Y. Liu, Y. Qu, K. L. Wang, Y. Huang, and X. Duan (2010). High-speed graphene transistors with a self-aligned nanowire gate. *Nature 467*(7313), 305.

Lieb, E. H. (2002). Two theorems on the hubbard model. In *Inequalities*, pp. 91–94. Springer.

Lin, Y.-M., C. Dimitrakopoulos, K. A. Jenkins, D. B. Farmer, H.-Y. Chiu, A. Grill, and P. Avouris (2010). 100-ghz transistors from wafer-scale epitaxial graphene. *Science 327*(5966), 662–662.

Liu, R., D. Wu, X. Feng, and K. Mullen (2011). Bottom-up fabrication of photolumi-nescent graphene quantum dots with uniform morphology. *Journal of the American*

Chemical Society 133(39), 15221–15223.

Lu, X., M. Yu, H. Huang, and R. S. Ruoff (1999). Tailoring graphite with the goal of achieving single sheets. *Nanotechnology 10*(3), 269.

Magda, G. Z., X. Jin, I. Hagymási, P. Vancsó, Z. Osváth, P. Nemes-Incze, C. Hwang, L. P. Biro, and L. Tapaszto (2014). Room-temperature magnetic order on zigzag edges of narrow graphene nanoribbons. *Nature 514*(7524), 608.

Mak, K. F., M. Y. Sfeir, Y. Wu, C. H. Lui, J. A. Misewich, and T. F. Heinz (2008). Measurement of the optical conductivity of graphene. *Physical review letters 101*(19), 196405.

Mak, K. F., J. Shan, and T. F. Heinz (2011). Seeing many-body effects in single-and few-layer graphene: observation of two-dimensional saddle-point excitons. *Physical review letters 106*(4), 046401.

Mao, J., Y. Jiang, D. Moldovan, G. Li, K. Watanabe, T. Taniguchi, M. R. Masir, F. M. Peeters, and E. Y. Andrei (2016). Realization of a tunable artificial atom at a super-critically charged vacancy in graphene. *Nature Physics 12*(6), 545.

Martin, J., N. Akerman, G. Ulbricht, T. Lohmann, J. v. Smet, K. Von Klitzing, and A. Yacoby (2008). Observation of electron–hole puddles in graphene using a scanning single-electron transistor. *Nature Physics 4*(2), 144.

McCreary, K. M., A. G. Swartz, W. Han, J. Fabian, and R. K. Kawakami (2012). Magnetic moment formation in graphene detected by scattering of pure spin currents. *Physical review letters 109*(18), 186604.

McFeely, F., S. Kowalczyk, L. Ley, R. Cavell, R. Pollak, and D. Shirley (1974). X-ray photoemission studies of diamond, graphite, and glassy carbon valence bands. *Physical Review B 9*(12), 5268.

Morita, Y., S. Suzuki, K. Sato, and T. Takui (2011). Synthetic organic spin chemistry for structurally well-defined open-shell graphene fragments. *Nature chemistry 3*(3), 197.

Morozov, S., K. Novoselov, M. Katsnelson, F. Schedin, D. Elias, J. A. Jaszczak, and

A. Geim (2008). Giant intrinsic carrier mobilities in graphene and its bilayer. *Physical review letters 100*(1), 016602.

Morpurgo, A. and F. Guinea (2006). Intervalley scattering, long-range disorder, and effective time-reversal symmetry breaking in graphene. *Physical Review Letters 97*(19), 196804.

Mueller, M. L., X. Yan, J. A. McGuire, and L. S. Li (2010). Triplet states and electronic relaxation in photoexcited graphene quantum dots. *Nano letters 10*(7), 2679–2682.

Muller, D. A., Y. Tzou, R. Raj, and J. Silcox (1993). Mapping sp2 and sp3 states of carbon at sub-nanometre spatial resolution. *Nature 366*(6457), 725.

Nair, R., M. Sepioni, I.-L. Tsai, O. Lehtinen, J. Keinonen, A. Krasheninnikov, T. Thomson, A. Geim, and I. Grigorieva (2012). Spin-half paramagnetism in graphene induced by point defects. *Nature Physics 8*(3), 199.

Nair, R., I.-L. Tsai, M. Sepioni, O. Lehtinen, J. Keinonen, A. Krasheninnikov, A. C. Neto, M. Katsnelson, A. Geim, and I. Grigorieva (2013). Dual origin of defect magnetism in graphene and its reversible switching by molecular doping. *Nature communications 4*, 2010.

Nair, R. R., P. Blake, A. N. Grigorenko, K. S. Novoselov, T. J. Booth, T. Stauber, N. M. Peres, and A. K. Geim (2008). Fine structure constant defines visual transparency of graphene. *Science 320*(5881), 1308–1308.

Neto, A. C., F. Guinea, and N. M. Peres (2006). Drawing conclusions from graphene. *Physics World 19*(11), 33.

Novoselov, K. S., V. I. Fal, L. Colombo, P. R. Gellert, M. G. Schwab, and K. Kim (2012). A roadmap for graphene. *Nature 490*(7419), 192.

Novoselov, K. S., A. K. Geim, S. V. Morozov, D. Jiang, M. I. Katsnelson, I. V. Grigorieva, S. V. Dubonos, and A. A. Firsov (2005). Two-dimensional gas of massless dirac fermions in graphene. *nature 438*(7065), 197.

Novoselov, K. S., A. K. Geim, S. V. Morozov, D. Jiang, Y. Zhang, S. V. Dubonos, I. V.

Grigorieva, and A. A. Firsov (2004). Electric field effect in atomically thin carbon films. *science 306*(5696), 666–669.

Özdemir, H. U., A. Altıntaş, and A. D. Güçlü (2016). Magnetic phases of graphene nanoribbons under potential fluctuations. *Physical Review B 93*(1), 014415.

Ozfidan, I., A. D. Güçlü, M. Korkusinski, and P. Hawrylak (2016). Theory of optical properties of graphene quantum dots. *physica status solidi (RRL)-Rapid Research Letters 10*(1), 102–110.

Palacios, J., J. Fernández-Rossier, and L. Brey (2008). Vacancy-induced magnetism in graphene and graphene ribbons. *Physical Review B 77*(19), 195428.

Pauling, L. (1941). *The Nature of the Chemical Bond and the Structure of Molecules and Crystals: An Introduction to Modern Structural Chemistry*. Wiley Online Library.

Peng, J., W. Gao, B. K. Gupta, Z. Liu, R. Romero-Aburto, L. Ge, L. Song, L. B. Alemany, X. Zhan, G. Gao, *et al.* (2012). Graphene quantum dots derived from carbon fibers. *Nano letters 12*(2), 844–849.

Peres, N., F. Guinea, and A. C. Neto (2006). Electronic properties of disordered two-dimensional carbon. *Physical Review B 73*(12), 125411.

Ponomarenko, L., A. Geim, A. Zhukov, R. Jalil, S. Morozov, K. Novoselov, I. Grigorieva, E. Hill, V. Cheianov, V. Falko, K. Watanabe, and T. Taniguchi (2011). Tunable metal-insulator transition in double-layer graphene heterostructures. *Nature Physics 7*(12), 958.

Potasz, P., A. Güçlü, and P. Hawrylak (2010). Spin and electronic correlations in gated graphene quantum rings. *Physical Review B 82*(7), 075425.

Potasz, P., A. Güçlü, A. Wójs, and P. Hawrylak (2012). Electronic properties of gated triangular graphene quantum dots: Magnetism, correlations, and geometrical effects. *Physical Review B 85*(7), 075431.

Reina, A., X. Jia, J. Ho, D. Nezich, H. Son, V. Bulovic, M. S. Dresselhaus, and J. Kong (2008). Large area, few-layer graphene films on arbitrary substrates by chemical va-

por deposition. *Nano letters 9*(1), 30–35.

Ritter, K. A. and J. W. Lyding (2009). The influence of edge structure on the electronic properties of graphene quantum dots and nanoribbons. *Nature materials 8*(3), 235.

Runge, E., E. Gross, and O. Heinonen (1991). *Many-particle theory*. Adam Hilger, Bristol.

Rycerz, A., J. Tworzydło, and C. W. J. Beenakker (2007). Valley filter and valley valve in graphene. *Nature Physics 3*(3), 172.

Safari, E. K., A. Shokri, and M. BabaeiPour (2017). Effects of vacancies on spin-dependent behavior of monolayer and bilayer graphene nanoribbons. *Journal of Magnetism and Magnetic Materials 441*, 230–237.

Saqurai, J. J. (1994). Modern quantum mechanics, revised edition.

Schubert, G. and H. Fehske (2012). Metal-to-insulator transition and electron-hole puddle formation in disordered graphene nanoribbons. *Physical review letters 108*(6), 066402.

Schubert, G., J. Schleede, and H. Fehske (2009). Anderson disorder in graphene nanoribbons: A local distribution approach. *Physical Review B 79*(23), 235116.

Sevinçli, H., M. Topsakal, E. Durgun, and S. Ciraci (2008). Electronic and magnetic properties of 3 d transition-metal atom adsorbed graphene and graphene nanoribbons. *Physical Review B 77*(19), 195434.

Shen, J., Y. Zhu, X. Yang, and C. Li (2012). Graphene quantum dots: emergent nano-lights for bioimaging, sensors, catalysis and photovoltaic devices. *Chemical communications 48*(31), 3686–3699.

Shenderova, O., V. Zhirnov, and D. Brenner (2002). Carbon nanostructures. *Critical reviews in solid state and material sciences 27*(3-4), 227–356.

Slater, J. C. (1929). The theory of complex spectra. *Physical Review 34*(10), 1293.

Šljivančanin, Ž., E. Rauls, L. Hornekær, W. Xu, F. Besenbacher, and B. Hammer (2009). Extended atomic hydrogen dimer configurations on the graphite (0001) surface. *The Journal of chemical physics 131*(8), 084706.

Soriano, D., N. Leconte, P. Ordejón, J.-C. Charlier, J.-J. Palacios, and S. Roche (2011). Magnetoresistance and magnetic ordering fingerprints in hydrogenated graphene. *Physical review letters 107*(1), 016602.

Soriano, D., F. Munoz-Rojas, J. Fernández-Rossier, and J. Palacios (2010). Hydrogenated graphene nanoribbons for spintronics. *Physical Review B 81*(16), 165409.

Subramaniam, D., F. Libisch, Y. Li, C. Pauly, V. Geringer, R. Reiter, T. Mashoff, M. Liebmann, J. Burgdörfer, C. Busse, *et al.* (2012). Wave-function mapping of graphene quantum dots with soft confinement. *Physical review letters 108*(4), 046801.

Sun, C., F. Figge, I. Ozfidan, M. Korkusinski, X. Yan, L.-s. Li, P. Hawrylak, and J. A. McGuire (2015). Biexciton binding of dirac fermions confined in colloidal graphene quantum dots. *Nano letters 15*(8), 5472–5476.

Szabo, A. and N. S. Ostlund (2012). *Modern quantum chemistry: introduction to advanced electronic structure theory*. Courier Corporation.

Talirz, L., H. Sode, J. Cai, P. Ruffieux, S. Blankenburg, R. Jafaar, R. Berger, X. Feng, K. Mullen, D. Passerone, *et al.* (2013). Termini of bottom-up fabricated graphene nanoribbons. *Journal of the American Chemical Society 135*(6), 2060–2063.

Tan, Y.-W., Y. Zhang, K. Bolotin, Y. Zhao, S. Adam, E. Hwang, S. D. Sarma, H. Stormer, and P. Kim (2007). Measurement of scattering rate and minimum conductivity in graphene. *Physical review letters 99*(24), 246803.

Trauzettel, B., D. V. Bulaev, D. Loss, and G. Burkard (2007). Spin qubits in graphene quantum dots. *Nature Physics 3*(3), 192.

Treier, M., C. A. Pignedoli, T. Laino, R. Rieger, K. Müllen, D. Passerone, and R. Fasel (2011). Surface-assisted cyclodehydrogenation provides a synthetic route towards easily processable and chemically tailored nanographenes. *Nature chemistry 3*(1), 61.

Uchoa, B., V. N. Kotov, N. Peres, and A. C. Neto (2008). Localized magnetic states in graphene. *Physical review letters 101*(2), 026805.

Ugeda, M. M., I. Brihuega, F. Guinea, and J. M. Gómez-Rodríguez (2010). Missing atom as a source of carbon magnetism. *Physical Review Letters 104*(9), 096804.

Van Bommel, A., J. Crombeen, and A. Van Tooren (1975). Leed and auger electron observations of the sic (0001) surface. *Surface Science 48*(2), 463–472.

Voznyy, O., A. D. Güçlü, P. Potasz, and P. Hawrylak (2011). Effect of edge reconstruction and passivation on zero-energy states and magnetism in triangular graphene quantum dots with zigzag edges. *Physical Review B 83*(16), 165417.

Wallace, P. R. (1947, May). The band theory of graphite. *Phys. Rev. 71*, 622–634.

Wassmann, T., A. P. Seitsonen, A. M. Saitta, M. Lazzeri, and F. Mauri (2008). Structure, stability, edge states, and aromaticity of graphene ribbons. *Physical Review Letters 101*(9), 096402.

Wei, D., Y. Liu, Y. Wang, H. Zhang, L. Huang, and G. Yu (2009). Synthesis of n-doped graphene by chemical vapor deposition and its electrical properties. *Nano letters 9*(5), 1752–1758.

Wu, Z.-S., W. Ren, L. Gao, B. Liu, C. Jiang, and H.-M. Cheng (2009). Synthesis of high-quality graphene with a pre-determined number of layers. *Carbon 47*(2), 493–499.

Xin, G., T. Yao, H. Sun, S. M. Scott, D. Shao, G. Wang, and J. Lian (2015). Highly thermally conductive and mechanically strong graphene fibers. *Science 349*(6252), 1083–1087.

Yazyev, O. V. and L. Helm (2007). Defect-induced magnetism in graphene. *Physical Review B 75*(12), 125408.

Yi, M. and Z. Shen (2015). A review on mechanical exfoliation for the scalable production of graphene. *Journal of Materials Chemistry A 3*(22), 11700–11715.

Yuan, S., R. Roldán, H. De Raedt, and M. I. Katsnelson (2011). Optical conductivity of

disordered graphene beyond the dirac cone approximation. *Physical Review B 84*(19), 195418.

Zarenia, M., A. Chaves, G. Farias, and F. Peeters (2011). Energy levels of triangular and hexagonal graphene quantum dots: a comparative study between the tight-binding and dirac equation approach. *Physical Review B 84*(24), 245403.

Zaretski, A. V. and D. J. Lipomi (2015). Processes for non-destructive transfer of graphene: widening the bottleneck for industrial scale production. *Nanoscale 7*(22), 9963–9969.

Zhang, Y., V. W. Brar, C. Girit, A. Zettl, and M. F. Crommie (2009). Origin of spatial charge inhomogeneity in graphene. *Nature Physics 5*(10), 722.

Zhang, Y., S.-Y. Li, H. Huang, W.-T. Li, J.-B. Qiao, W.-X. Wang, L.-J. Yin, K.-K. Bai, W. Duan, and L. He (2016). Scanning tunneling microscopy of the π magnetism of a single carbon vacancy in graphene. *Physical review letters 117*(16), 166801.

Zhang, Y., Y. W. Tan, H. L. Stormer, and P. Kim (2005). Experimental observation of the quantum hall effect and berry's phase in graphene. *nature 438*(7065), 201.

Zhang, Y., T. T. Tang, C. Girit, Z. Hao, M. C. Martin, A. Zettl, M. F. Crommie, Y. R. Shen, and F. Wang (2009). Direct observation of a widely tunable bandgap in bilayer graphene. *Nature 459*(7248), 820.

Zurutuza, A. and C. Marinelli (2014). Challenges and opportunities in graphene commercialization. *Nature nanotechnology 9*(10), 730.

APPENDIX A

MATLAB CODES

```
%The program computes effects of long range disorder
%and electron−electron interactions
%on the optical properties of
%hexagonal armchair graphene quantum dots.

%Short−range disorder can be built similarly
%Short−range disorder has been not included here!

%The model Hamilltonians are Tight−Binding,
%Mean−Field Hubbard and
%Many−body configuration interactions


% Author: Abdulmenaf ALTINTAS


%%%——————————LONG−RANGE DISORDER————%%
%%%—————ELECTRON−ELECTRON INTERACTIONS——%%

 clear all;
 close all;
 tic;% shows elapsed time
 SizeofDot=2;% a parameter to determine size of quantum dot
 %fprintf('\n\n Size of the dot parameter=%d is determined!
 ...!!\n\n',SizeofDot); %Displays size of quantum dot
 epsilon=0.0001;% epsilon is needed for accuracy that
 %program needs
 a=2.683410904; % a which is the distance between two
 %carbon atoms is in atomic unit
 tnn=2.8; % t=tnn which is the nearest neighbour
 %hopping integral is in eV
 tnnn=0.2; % t=tnnn which is the next nearest
 %neighbour hopping integral is in eV
```

```matlab
nlimit=1000; % a upper limit of for loop
count=0;  % used as an index number
sqrt3=1.732050807568877;% defining square roots
%improves program performance
slope=1/sqrt3;  % decrease computation time
a1_x=a*0.5*sqrt3; a2_x=-a*0.5*sqrt3; b_x=0;
a1_y=a*1.5; a2_y=a*1.5; b_y=a; % unit cell vectors


%% Determining coordinates coordinates of quantum dot%%%

for n=-nlimit:nlimit
for m=-nlimit:nlimit
xtemp=n*a1_x+m*a2_x+b_x;
ytemp=n*a1_y+m*a2_y+b_y;


if ytemp<=-slope*xtemp+(3+3*SizeofDot)*a+epsilon
if ytemp<=slope*xtemp+(3+3*SizeofDot)*a+epsilon
if xtemp>=-(2+(SizeofDot-1)*1.5)*sqrt3*a-epsilon
if ytemp>=-slope*xtemp-(3*SizeofDot-1)*a-epsilon
    if ytemp>=slope*xtemp-(3*SizeofDot-1)*a-epsilon
      if xtemp<=(2+(SizeofDot-1)*1.5)*sqrt3*a+epsilon
          count=count+1;
          xcoor(count)=xtemp;
          ycoor(count)=ytemp;
      end
    end
end
end
end
end


xtemp=n*a1_x+m*a2_x;
ytemp=n*a1_y+m*a2_y;
if ytemp<=-slope*xtemp+(3+3*SizeofDot)*a+epsilon
if ytemp<=slope*xtemp+(3+3*SizeofDot)*a+epsilon
if xtemp>=-(2+(SizeofDot-1)*1.5)*sqrt3*a-epsilon
if ytemp>=-slope*xtemp-(3*SizeofDot-1)*a-epsilon
    if ytemp>=slope*xtemp-(3*SizeofDot-1)*a-epsilon
```

```matlab
        if xtemp<=(2+(SizeofDot-1)*1.5)*sqrt3*a+epsilon
            count=count+1;
            xcoor(count)=xtemp;
            ycoor(count)=ytemp;
        end
    end
end
end
end
end
end
end

%% Determining off-diagonal and diagonal matrix elements
%of any matrix
Natom=size(xcoor,2)% Number of atoms
Nmatrix=zeros(Natom);
for i=1:Natom
for j=1:Natom
d=sqrt((xcoor(i)-xcoor(j))^2+(ycoor(i)-ycoor(j))^2);
if d>a-epsilon && d<a+epsilon% nearest neighbours
    Nmatrix(i,j)=2;
elseif d>a*sqrt3-epsilon && d<a*sqrt3+epsilon% next-nearest
    %neighburs
        Nmatrix(i,j)=3;
elseif i==j
    Nmatrix(i,j)=1;%on-site
end
end
end

%% Creating long-range ramdomly distributed impurity

Vimp=zeros(Natom,1);
sigmaimp=10*a;% determines range of impurity
nimpurity=20; % determines number of impurity
fprintf('\n\n Number of impurity =%d !!!\n\n',nimpurity);
%Displays impurity
randimpxcoor=(max(xcoor)-min(xcoor)).*...
```

```matlab
    rand(nimpurity,1)+min(xcoor);
% x- coordinates of impurities
randimpycoor=(max(ycoor)-min(ycoor)).*...
    rand(nimpurity,1)+min(ycoor);
% y- coordinates of impurities
puddletop=tnn/3; % High level  of impurity potential in eV
puddlebott=-tnn/3; % Low level of impurity potential in eV
Vimpheight =((puddletop-puddlebott)).*...
    rand(nimpurity,1) + puddlebott;
% Impurity potential
for i=1:Natom;
for j=1:nimpurity;

Vimp(i)=Vimp(i)+(Vimpheight(j))*gaussmf(xcoor(i),...
    [sigmaimp randimpxcoor(j)])'*...
    gaussmf(ycoor(i),[sigmaimp randimpycoor(j)]);

end
end
%fprintf('\n\n Impurity  potential created for number
%of impurity=%d !!!\n\n',nimpurity); %Displays impurity

%% Compute and Diagonalize TB and MFH Hamiltonians
Nup=Natom/2; % number of up electrons
Ndown=Natom/2; %number of down electrons
Ntotal=Nup+Ndown; %total number of electrons
mix=0.4; % assign weight of first determined density matrix
%contribution


Kapa=6;% Kapa is material propertiy and unitless
fprintf('\n\nKapa=%d !!!\n\n',Kapa);%Displays Kapa value

Htb=zeros(Natom); %tight-binding hamiltonian construction
for i=1:Natom
for j=1:Natom
if Nmatrix(i,j)==2;
    Htb(i,j)=-tnn;
elseif Nmatrix(i,j)==3;
```

```matlab
        Htb(i,j)=-tnnn;
 elseif Nmatrix(i,j)==1;
      Htb(i,j)=Vimp(i);
end
end
end
[Eigenvector_tb,Eigenvalue_tb] = eig(Htb);
%diagonalization of tight-binding hamiltonian


H_down=Htb;%initial down electron hamiltonian
H_up=Htb;%intial up electron


Ucoulomb=16.522/Kapa; %in eV-onsite coulomb
%repulsion taken from graphenebook


%Determining off-site longrange coulomb interaction
Vcoulomb=zeros(Natom);
for i=1:Natom
for j=1:Natom
  if Nmatrix(i,j)==2;
      Vcoulomb(i,j)=8.640/Kapa; % in eV-nn
     %off-site coulomb repulsion
    elseif Nmatrix(i,j)==3;
          Vcoulomb(i,j)=5.33/Kapa;  % in eV-nnn
         %off-site coulomb repulsion
    elseif i~=j
          Vcoulomb(i,j)=27.21138/(Kapa*sqrt((xcoor(i)-...
              xcoor(j))^2+(ycoor(i)-ycoor(j))^2));
              % 1 au = 27.21138 eV   distance is in au.
  end
end
end


%fprintf('\n\n Interaction matrix is created for
%Kapa=%d !!!\n\n\n\n',Kapa);%Displays Kapa value


Hrandom=rand(Natom);% Intial Random matrix
[Eigenvector_selfcons,Eigenvalue_selfcons] = ...
    eig(Htb+Hrandom+Hrandom');
```

```matlab
%imitial diagonalization for self-consisten loop
clear Hrandom;

densitymatrix_up=conj(Eigenvector_selfcons(:,1:Nup))*...
    Eigenvector_selfcons(:,1:Nup)';
%inital density matrix for up electrons
densitymatrix_down=conj(Eigenvector_selfcons(:,1:Ndown))*...
    Eigenvector_selfcons(:,1:Ndown)'
;%inital density matrix for down electrons
densitymatrix_all=densitymatrix_up+densitymatrix_down;

Delta_Energy=100;% initial condition for while loop
selfconscount=1;% count parameter
TBEnergy=sum(diag(Htb'*densitymatrix_all));
% Tight-binding energy
GroundstateEnergy=TBEnergy;% Initial ground state energy
GroundstateEng(selfconscount)=GroundstateEnergy;

%%%%Self-consisten loop
% each variable name indicates its function explicitly
while Delta_Energy >= 10^(-8) %eV;

selfconscount=selfconscount+1;

[Eigenvector_up,Eigenvalue_up] = eig(H_up);
Diageigenvalue_up=diag(Eigenvalue_up);

densitymatrix_up=conj(Eigenvector_up(:,1:Nup))*...
    Eigenvector_up(:,1:Nup)'*(1-mix)+mix*densitymatrix_up;

[Eigenvector_down,Eigenvalue_down] = eig(H_down);
Diageigenvalue_down=diag(Eigenvalue_down);

densitymatrix_down=conj(Eigenvector_down(:,1:Ndown))*...
  Eigenvector_down(:,1:Ndown)'*(1-mix)+mix*densitymatrix_down;

densitymatrix_all=densitymatrix_up+densitymatrix_down;

n_up=diag(densitymatrix_up);
```

```matlab
n_down=diag(densitymatrix_down);
n_all=n_up+n_down;

H_int_up=zeros(Natom);
H_int_down=zeros(Natom);
V_int_coulomb=Vcoulomb*(n_all-1);

for i=1:Natom;
H_int_up(i,i)=Ucoulomb*(n_down(i)-0.5)+V_int_coulomb(i);
H_int_down(i,i)=Ucoulomb*(n_up(i)-0.5)+V_int_coulomb(i);
end

H_up=Htb+H_int_up;
H_down=Htb+H_int_down;

TBEnergy=sum(diag(Htb'*densitymatrix_all));
onsiteEnergy=Ucoulomb*...
diag(densitymatrix_up-0.5)'*diag(densitymatrix_down-0.5);
longrangeEnergy=(0.5)*diag(densitymatrix_all-1)'*...
 Vcoulomb*diag(densitymatrix_all-1);
GroundstateEnergy=TBEnergy+onsiteEnergy+longrangeEnergy;
format long g;
GroundstateEng(selfconscount)=GroundstateEnergy;
Delta_Energy=abs(GroundstateEng(selfconscount)-...
    GroundstateEng(selfconscount-1))/Ntotal;
GroundstateEnergyPerelec=GroundstateEnergy/Ntotal;
%Parameters1=[selfconscount  GroundstateEnergy
%GroundstateEnergyPerelec  Delta_Energy  ];
%disp(Parameters1)
end


% Parameters2='
% selfconscount     TotGroundstateEnergy
% GroundstateEnergyPerelec    Delta_Energyperelec    ';
% disp(Parameters2)
% Parameters3=[selfconscount       G
%
% roundstateEnergy      GroundstateEnergyPerelec
```

```matlab
% Delta_Energy ];
% disp(Parameters3)


%% Compute diagonal terms of many-body interaction matrix
%each variable name indicates its function explicitly
%please refer to chapter 3.4 of thesis to understand
%the meaning of matrix
%elements
Vcoulomb_matrix=Vcoulomb;
for i=1:Natom;
Vcoulomb_matrix(i,i)=Ucoulomb;
end
count=0;
countr=0;
for r=Natom/2:-1:1


countr=countr+1;


fprintf('\n Number of Iteration=%d !!!\n',countr);
%Displays Iteration value
if countr<2
%fprintf('\n Interaction diagonal
%matrix elements calculation started !!!\n');
end
countp_prime=0;
for p_prime=Natom/2+1:Natom
countp_prime=countp_prime+1;


r_reindexed=countr;
p_prime_reindexed=countp_prime;
V_diagonal_direct_excitonic_matrix ...
(r_reindexed,p_prime_reindexed)=...
[conj(Eigenvector_up(:,r)).*Eigenvector_up(:,r)]' ...
*Vcoulomb_matrix* ...
[conj(Eigenvector_up(:,p_prime)).*Eigenvector_up(:,p_prime)];


V_diagonal_exchange_excitonic_matrix ...
(r_reindexed,p_prime_reindexed)= ...
```

```matlab
[conj(Eigenvector_up(:,r)).*Eigenvector_up(:,p_prime)]' ...
*Vcoulomb_matrix* ...
[conj(Eigenvector_up(:,p_prime)).*Eigenvector_up(:,r)];
end


end

%fprintf('\n\n Interaction diagonal
%matrix elements calculation ended !!!\n\n');


%% Compute direct and exchange terms of many-body
%interaction matrix
%each variable name indicates its function explicitly
%please refer to chapter 3.4 of thesis to understand
%the meaning of matrix
%elements
% In order to increase computation speed we add some
%reduction algoratihm
% by using symmetric properties of interaction matrix

deep_level_index=10;%Determines number
%of deep level interaction
%fprintf('\n\ndeep_level_index=%d
%!!!\n\n',deep_level_index);
%Displays deep_level_index value

Vcoulomb_matrix=Vcoulomb;
for i=1:Natom;
Vcoulomb_matrix(i,i)=Ucoulomb;
%Here we reaarange coulomb matrix
%created before code eigenvalues and eigenvectors
end

V_direct_excitonic_matrix=-10000*...
ones(deep_level_index,deep_level_index,...
deep_level_index,deep_level_index);
V_exchange_excitonic_matrix=-...
10000*ones(deep_level_index,deep_level_index...
,deep_level_index,deep_level_index);
```

```
count =0;
countr =0;
for  r=Natom/2: −1:Natom/2−deep_level_index +1
countr=countr +1;
fprintf ('\n Number of Iteration=%d !!!\n', countr );
%Displays Iteration value
if countr <2
tic ;
%fprintf ('\n Interaction matrix
%elements calculation started !!!\n');
end


countq =0;
for  q=Natom/2: −1:Natom/2−deep_level_index +1
countq=countq +1;
countp_prime =0;
for  p_prime=Natom/2+1:Natom/2+deep_level_index
countp_prime=countp_prime +1;
counts_prime =0;
for  s_prime=Natom/2+1:Natom/2+deep_level_index
counts_prime=counts_prime +1;



r_reindexed=countr ;
q_reindexed=countq ;
p_prime_reindexed=countp_prime ;
s_prime_reindexed=counts_prime ;
if V_direct_excitonic_matrix ...
(r_reindexed , p_prime_reindexed ,...
s_prime_reindexed , q_reindexed)==−10000

V_direct_excitonic_matrix ...
(r_reindexed , p_prime_reindexed ,...
s_prime_reindexed , q_reindexed)= ...
[conj(Eigenvector_up (: , r )). ∗ Eigenvector_up (: , q)] ' ...
∗Vcoulomb_matrix∗ ...
[conj(Eigenvector_up (: , p_prime )). ∗...
Eigenvector_up (: , s_prime )];
```

```matlab
%Reduction starts from below !!
V_direct_excitonic_matrix(r_reindexed,...
s_prime_reindexed,p_prime_reindexed,q_reindexed)= ...
V_direct_excitonic_matrix(r_reindexed,...
p_prime_reindexed,s_prime_reindexed,q_reindexed);


V_direct_excitonic_matrix(q_reindexed,...
p_prime_reindexed,s_prime_reindexed,r_reindexed)= ...
V_direct_excitonic_matrix(r_reindexed,...
p_prime_reindexed,s_prime_reindexed,q_reindexed);


V_direct_excitonic_matrix(q_reindexed,...
s_prime_reindexed,p_prime_reindexed,r_reindexed)= ...
V_direct_excitonic_matrix(r_reindexed,...
p_prime_reindexed,s_prime_reindexed,q_reindexed);
end
if V_exchange_excitonic_matrix(r_reindexed,...
p_prime_reindexed,q_reindexed,...
s_prime_reindexed)==-10000;


V_exchange_excitonic_matrix(r_reindexed,...
p_prime_reindexed,q_reindexed,s_prime_reindexed)= ...
[conj(Eigenvector_up(:,r)).*Eigenvector_up(:,s_prime)]' ...
*Vcoulomb_matrix* ...
[conj(Eigenvector_up(:,p_prime)).*...
Eigenvector_up(:,q)];



V_exchange_excitonic_matrix(q_reindexed,...
s_prime_reindexed,r_reindexed,p_prime_reindexed)= ...
V_exchange_excitonic_matrix(r_reindexed,...
p_prime_reindexed,q_reindexed,s_prime_reindexed);
end
end
end
end
if countr<2
time_for_one_loop=toc;
%fprintf('\n\n Count Time=%0.6f seconds For One
```

```matlab
%Loop in Interaction Matrix !!!\n\n',
%time_for_one_loop);%Displays Total time
end
end

%fprintf('\n\n Interaction  matrix
%elements calculation ended !!!\n\n');

%% Construct many-body Hamiltonaian

Orbital_Exc=zeros(2*deep_level_index^2,2);
count=0;
for i=1:deep_level_index
for j=1:deep_level_index
count=count+1;
Orbital_Exc(count,1)=i;
Orbital_Exc(count,2)=j;
end
end

Orbital_Exc(deep_level_index^2+1:2*...
deep_level_index^2,1)=Orbital_Exc(1:deep_level_index^2,1);
Orbital_Exc(deep_level_index^2+1:2*...
deep_level_index^2,2)=Orbital_Exc(1:deep_level_index^2,2);


%Num_of_MB_Basis=deep_level_index^2;
H_MB_CI_Exc=zeros(2*deep_level_index^2);
%fprintf('\nMany Body Hamiltonian
%construction started !!!\n');
for J2=1:2*deep_level_index^2

if J2<=deep_level_index^2
mu_prime_up=Orbital_Exc(J2,2);
% Indicates electron energy level in conduction state
nu_down=Orbital_Exc(J2,1);
% Indicates hole energy level in valance state
end
if J2>deep_level_index^2
```

```matlab
mu_prime_down=Orbital_Exc(J2,2);
% Indicates electron energy level in conduction state
nu_up=Orbital_Exc(J2,1);
% Indicates hole energy level in valance state
end
for J1=1:2*deep_level_index^2
if J1<=deep_level_index^2
beta_prime_up=Orbital_Exc(J1,2);
% Indicates electron energy level in conduction state
alpha_down=Orbital_Exc(J1,1);
% Indicates hole energy level in valance state
end
if J1>deep_level_index^2
beta_prime_down=Orbital_Exc(J2,2);
% Indicates electron energy level in conduction state
alpha_up=Orbital_Exc(J2,1);
% Indicates hole energy level in valance state
end
if J2<=deep_level_index^2 && J1<=deep_level_index^2
if    J2==J1
H_MB_CI_Exc(J1,J2)=Diageigenvalue_up(Natom/2+mu_prime_up)-...
     Diageigenvalue_up(Natom/2-alpha_down+1)-...
(V_direct_excitonic_matrix(nu_down,beta_prime_up...
,mu_prime_up,alpha_down)-  ...
V_exchange_excitonic_matrix(nu_down,beta_prime_up,...
alpha_down,mu_prime_up));
else
H_MB_CI_Exc(J1,J2)=(-1)*(V_direct_excitonic_matrix...
     (nu_down,beta_prime_up,mu_prime_up,alpha_down)-...
V_exchange_excitonic_matrix(nu_down,beta_prime_up,...
alpha_down,mu_prime_up));

end
end

if J2>deep_level_index^2 && J1<=deep_level_index^2
H_MB_CI_Exc(J1,J2)=V_exchange_excitonic_matrix...
     (nu_up,beta_prime_up,alpha_down,mu_prime_down);
end
```

```matlab
end
end

fprintf('\nMany Body Hamiltonian construction ended !!!\n');
H_MB_CI_Exc(deep_level_index^2+1:2*...
deep_level_index^2,deep_level_index^2+1:2*deep_level_index^2)=...
H_MB_CI_Exc(1:deep_level_index^2,...
1:deep_level_index^2);
H_MB_CI_Exc(deep_level_index^2+1:2*...
deep_level_index^2,1:deep_level_index^2)=...
H_MB_CI_Exc(1:deep_level_index^2,...
deep_level_index^2+1:2*deep_level_index^2);

%fprintf('\nMany Body Hamiltonian
%diagonalization started !!!\n');
[Eigenvector_MB_CI_Exc,Eigenvalue_MB_CI_Exc]...
    = eig(H_MB_CI_Exc);
%fprintf('\nMany Body Hamiltonian
%diagonalization ended !!!\n');

%fprintf('\nMany Body Hamiltonian
%sorting started !!!\n');
if ~issorted(diag(Eigenvalue_MB_CI_Exc));
% Creates sorted Eigenvalues in
%ascending order with corresponding Eigenvectors
[Eigenvalue_MB_CI_Exc,I] = sort(diag(Eigenvalue_MB_CI_Exc));
Eigenvector_MB_CI_Exc = Eigenvector_MB_CI_Exc(:, I);
end
fprintf('\nMany Body Hamiltonian sorting ended !!!\n');
%Creates diagonal matrix
Diageigenvalue_MB_CI_Exc=diag(Eigenvalue_MB_CI_Exc);

%% Join-density of states obtained by tight-binding
%for optical properties

dipole=0;
Abs_xdip=zeros(Natom);
Abs_ydip=zeros(Natom);
for i=1:Natom
```

```
for j=1:Natom
if Htb(i,j)==-tnn
    dipole=0.3433;
    Abs_xdip(i,j)=dipole*(xcoor(j)-xcoor(i))/a;
    Abs_ydip(i,j)=dipole*(ycoor(j)-ycoor(i))/a;

elseif Htb(i,j)==-tnnn
    dipole=0.0873;
    Abs_xdip(i,j)=dipole*(xcoor(j)-xcoor(i))/(a*sqrt3);
    Abs_ydip(i,j)=dipole*(ycoor(j)-ycoor(i))/(a*sqrt3);

elseif i==j

    Abs_xdip(i,j)=xcoor(i);
    Abs_ydip(i,j)=ycoor(i);
else
    dipole=0;
    Abs_xdip(i,j)=0;
    Abs_ydip(i,j)=0;
end
end
end

[Eigenvector_tb,Eigenvalue_tb] = eig(Htb);
Diageigenvalue_tb=diag(Eigenvalue_tb);

Abs_x=Eigenvector_tb'*Abs_xdip*Eigenvector_tb;
Abs_y=Eigenvector_tb'*Abs_ydip*Eigenvector_tb;
Abs=Abs_x.^2+Abs_y.^2;

Engjdos=0:0.01:20;
sigmajdos=0.1;
JDOS_tb=zeros(size(Engjdos,2),1);
% JDOS needs to be divided to total area of
%the quantum dot Area=(Natom*3*a^2*sqrt3/4)
Area=(Natom*3*a^2*sqrt3/4);
for p=1:Natom/2
for q=Natom/2+1:Natom
tempE=Diageigenvalue_tb(q)-Diageigenvalue_tb(p);
```

```
JDOS_tb=JDOS_tb+Abs(p,q)*(1/Area)*tempE*4*...
    pi^2/137*gaussmf(Engjdos,[sigmajdos tempE])'.*...
    1/(sigmajdos*sqrt(2*pi));
end
end


%% Join−density of states calculations obtained
%by mean−field Hubbard for optical properties
Abs_x_up=Eigenvector_up'*Abs_xdip*Eigenvector_up;
Abs_y_up=Eigenvector_up'*Abs_ydip*Eigenvector_up;


Abs_up=Abs_x_up.^2+Abs_y_up.^2;
JDOS_up_MFH=zeros(size(Engjdos,2),1);
Area=(Natom*3*a^2*sqrt3/4);% JDOS needs
%to be divided to total area of the quantum dot Area
for p=1:Natom/2
for q=Natom/2+1:Natom
tempE_up=Diageigenvalue_up(q)−Diageigenvalue_up(p);
JDOS_up_MFH=JDOS_up_MFH+Abs_up(p,q)*(1/Area)*...
tempE_up*4*pi^2/137*gaussmf...
(Engjdos,[sigmajdos tempE_up])'.*1/(sigmajdos*sqrt(2*pi));
end
end


%% Join−density of states calculations obtained by
%many−body interaction of diagonal−terms for
%optical properties
JDOS_up_Exciton=zeros(size(Engjdos,2),1);
Area=(Natom*3*a^2*sqrt3/4);% JDOS needs to
%be divided to total area of the quantum dot Area
countr=0;
for r=Natom/2:−1:1;
countr=countr+1;
countp_prime=0;
for p_prime=Natom/2+1:Natom;
countp_prime=countp_prime+1;
        r_reindexed=countr;
        p_prime_reindexed=countp_prime;
```

```
tempE_up=Diageigenvalue_up(p_prime)−...
Diageigenvalue_up(r)−  ...
(V_diagonal_direct_excitonic_matrix...
(r_reindexed,p_prime_reindexed)−  ...
V_diagonal_exchange_excitonic_matrix...
(r_reindexed,p_prime_reindexed));

JDOS_up_Exciton=JDOS_up_Exciton+...
  Abs_up(r,p_prime)*(1/Area)*tempE_up*4*pi^2/137*  ...
gaussmf(Engjdos,[sigmajdos tempE_up])'.*...
1/(sigmajdos*sqrt(2*pi));
end
end


%% Join−density of states calculations obtained
%by many−body interaction of direct
%and excahnge terms for optical properties


Abs_x_up_molecular=Eigenvector_up'*Abs_xdip*Eigenvector_up;
Abs_y_up_molecular=Eigenvector_up'*Abs_ydip*Eigenvector_up;


dip_J_x=zeros(2*deep_level_index^2,1)';
dip_J_y=zeros(2*deep_level_index^2,1)';


for J=1:2*deep_level_index^2
beta_prime_J=Orbital_Exc(J,1);% Indicates electron
%energy level in conduction state
alpha_J=Orbital_Exc(J,2);% Indicates
%hole energy level in valance state

dip_J_x(J)=Abs_x_up_molecular...
(Natom/2+beta_prime_J,Natom/2−alpha_J+1);
dip_J_y(J)=Abs_y_up_molecular...
(Natom/2+beta_prime_J,Natom/2−alpha_J+1);
end


Abs_dip_CI_J_x=dip_J_x*Eigenvector_MB_CI_Exc;
Abs_dip_CI_J_y=dip_J_y*Eigenvector_MB_CI_Exc;
```

```matlab
Abs_CI_Exc=Abs_dip_CI_J_x.^2+Abs_dip_CI_J_y.^2;


Engjdos_CI_Exc=0:0.01:3;
sigmajdos_CI_Add=0.02;
JDOS_CI_Add=zeros(size(Engjdos_CI_Exc,2),1);
Area=(Natom*3*a^2*sqrt3/4);% JDOS needs to be
%divided to total area of the quantum dot Area
for p=1:2*deep_level_index^2;
JDOS_CI_Add=JDOS_CI_Add+Abs_CI_Exc(p)*(1/Area)* ...
  Diageigenvalue_MB_CI_Exc(p)*4*pi^2/137* ...
    gaussmf(Engjdos_CI_Exc,...
    [sigmajdos_CI_Add Diageigenvalue_MB_CI_Exc(p)])'.*...
    1/(sigmajdos_CI_Add*sqrt(2*pi));
end


%% Computes density of states (DOS)
Engdos=-10:0.01:10;
sigmados=0.1;
DOS_tb=zeros(size(Engdos,2),1);
%DiagEigenvalue_tb=diag(Eigenvalue_tb);
for i=1:Natom
DOS_tb=DOS_tb+gaussmf(Engdos,...
      [sigmados Diageigenvalue_tb(i)])'.*...
  1/(sigmados*sqrt(2*pi))*(4/Natom);
end
% We multiplied gaussmf with (1/(Natom/2)*2.
% (Natom/2) is the number of unit cells
% *2 is the spin conribution
%figure;
hold on;
plot(Engdos,DOS_tb);


%% Probability density plots


figure;% for down electrons
numPointss=250;
x0=linspace(min(xcoor)-5,max(xcoor)+5,numPointss);
y0=linspace(min(ycoor)-5,max(ycoor)+5,numPointss);
sigmaprobdensity=a/2;
```

```
z1=zeros(size(x0,2));
for is=1:Natom
z1=z1+(sum(Eigenvector_down(is,1:Ndown)'.^2))*...
gaussmf(x0,[sigmaprobdensity xcoor(is)])'*...
gaussmf(y0,[sigmaprobdensity ycoor(is)]).*...
(1/(sigmaprobdensity*sqrt(2*pi)))^2;
end
[x,y]=meshgrid(x0,y0);
mesh(x,y,z1');
view(-90,-90);
axis off;
%colorbar off;
az =0;
el =90;
colorbar; view(az, el);
%caxis([0 10^-2])
```

VITA

EDUCATION

2012 - 2018 Doctor of Philosophy in Theoretical Condensed Matter Physics

Graduate School of Engineering and Sciences, İzmir Institute of Technology,

İzmir -Turkey

Thesis Title: Electronic, Magnetic and Optical Properties of Graphene Quantum Dots

Supervisor: Assoc. Prof. Dr. Alev Devrim GÜÇLÜ

2008 - 2010 Master of Science in Experimental Physics

Institute of Physics, Lund University, Lund-Sweden

Thesis Title: Electrical Characterization of GaAS:Mn Nanowires

Supervisors: Prof. Dr. Hongqi Xu and Dr. Henrik A. Nilsson

2003 - 2007 Bachelor of Physics

Department of Physics, Faculty of Science, Middle East Technical University

Ankara - Turkey

PROFESSIONAL EXPERIENCE

2014 - 2018 Research and Teaching Assistant

Department of Physics, İzmir Institute of Technology, İzmir -Turkey

SELECTED PUBLICATIONS

Altıntaş, A. and Güçlü, A. D., (2018).
 "Defect induced Anderson localization and magnetization in graphene quantum dots".
Solid State Communications, 281, 44.

Altıntaş, A., Çakmak, K. E. and Güçlü, A. D., (2017).
 "Effects of long-range disorder and electronic interactions on the optical
properties of graphene quantum dots".
Physical Review B, 95, 045431 .

Özdemir, Hakan Ulaş, Altıntaş, A. and Güçlü, A. D., (2016).
"Magnetic phases of graphene nanoribbons under potential fluctuations".
Physical Review B, 93, 014415 .